


1-1-2015

Frequency Domain Ultrasound Waveform Tomography Breast Imaging

Gursharan Singh Sandhu
Wayne State University,

Follow this and additional works at: http://digitalcommons.wayne.edu/oa_dissertations

 Part of the [Bioimaging and Biomedical Optics Commons](#), and the [Physics Commons](#)

Recommended Citation

Sandhu, Gursharan Singh, "Frequency Domain Ultrasound Waveform Tomography Breast Imaging" (2015). *Wayne State University Dissertations*. Paper 1295.

This Open Access Dissertation is brought to you for free and open access by DigitalCommons@WayneState. It has been accepted for inclusion in Wayne State University Dissertations by an authorized administrator of DigitalCommons@WayneState.

**FREQUENCY DOMAIN ULTRASOUND WAVEFORM TOMOGRAPHY
BREAST IMAGING**

by

GURSHARAN YASH SINGH SANDHU

DISSERTATION

Submitted to the Graduate School

of Wayne State University,

Detroit, Michigan

in partial fulfillment of the requirements

for the degree of

DOCTOR OF PHILOSOPHY

2015

MAJOR: PHYSICS

Approved by:

Advisor

Date

Co-Advisor

© COPYRIGHT BY

GURSHARAN YASH SINGH SANDHU

2015

Some Rights Reserved

DEDICATION

For my grandmother, father, and aunty ... all of them survivors of cancer.

ACKNOWLEDGMENTS

The last five years have been a very rewarding experience. I can only make such a statement due to the diligence of others who have made a profound impact in my life.

I would first like to thank four individuals who ultimately decided my current path in life. I thank Dr. Ratna Naik. Without her help, I would not have been a student in the Department of Physics and Astronomy at Wayne State University (WSU). She has served as an advisor as well a mother figure to me. I will always be in her debt. I thank Dr. Jay Burmeister. As a physics student, he allowed me to participate in the Medical Physics Department at the WSU School of Medicine (SM). As a result, I gained a great deal of knowledge that has proven to be invaluable in my work. He has always been very kind, understanding, and encouraging of my work. I thank Dr. Zhi-Feng Huang. He has served as my Ph. D. advisor and has made a great deal of effort to ensure my success as a Ph. D. student. He has been a great mentor and has always made sure I understand the importance of good scientific work. His suggestions have made me in to a better scientist. I thank Dr. Neb Duric. He has served as my co-advisor and has adopted me into the fold of his research team. He has been patient while I have gained the skills necessary to perform research in the field of medical imaging. He has always been encouraging, but has also pushed me to do my best. Although I have many people to thank for where I am today, Dr. Duric's support of my work led to my eventual success.

My time at WSU has provided me with the necessary skills to perform research in medical imaging. A part of the success is due to the didactic teaching of the faculty at WSU and WSUSM. I have learned a great deal about physics and medical physics as a result of my course work. I thank my fellow students and colleagues with whom I have had the pleasure to study and laugh. I thank all my fellow employees at Delphinus Medical Technologies Inc. (DMT). Working with all of you great. If it wasn't for television and other media portraying an obnoxious and sullen work environment, I would be completely oblivious that such things could be possible. I thank Dr. Steven Schmidt for always having an answer to any question

that I may have. This ranged from simple programming questions to technical details about our ultrasound tomography device. He has served as a great role model for me. I thank Erik West and Kuo Li for help with many programming and research related questions. I thank Zack Mumm, Michael Boone, Mark Sak, Katelyn Montgomery, and Matt Prus for help with various experiments. I thank all of the members of the DMT hardware team. Without your efforts, it would not be possible for me to conduct my research. As I can not write everyone's name, I thank everyone at DMT.

The following individuals have had some of the greatest impact in the development of my technical skills. I thank Dr. Cuiping Li. I do not know where to begin. She has fostered me from the very beginning when I did not know what "cd" meant in a Linux terminal to this day as I am writing this section of my thesis. She has given me infinite kindness and I will always cherish her as my friend, colleague, and mentor. I thank Dr. Olivier Roy. His encouragement and optimism was a fuel that I needed when I was most discouraged. Discussing mathematics with him has given me a great deal of joy. He has expounded that by rigorously following the principles of mathematics, that the truth will be revealed. As a result, I know understand how to see the true face of nature. I thank Dr. Peter Littrup. He has taught me a great deal of about radiology and the interpretation of medical images. His view of life has given me an important perspective about the choices I will make in my life.

Last, I would like to thank my family and friends for all their encouragement and support throughout my life and studies. To my mom and dad, the things I have done in my life are only possible as result of your sacrifice. You moved to an unknown country with the hopes that it will provide an opportunity for your children. I have not always been the best son or cherished this sacrifice. I want to let you know that I have learned from my mistakes that I have made in life, and that I love you from the bottom of my heart. To my sister Sonu, you are a part of me. Not only do we share the same DNA, but we share something more important: memories that have come and gone and memories that have yet to be forged. No matter what happens in life, you are my sister and, I will always love and be a friend to you. To my brother-in-law Aman, thank you for taking care of my sister. I can always

sleep in comfort knowing that she has someone like you in her life. Over the last few years, you have become a part of my family, and I love you. I look forward to all the memories that I will have with you guys and my niece and nephew. To all of my uncles, aunties, and cousins, thank you. All of you have given me the pleasure of family. To my uncle Dr. Daya Singh Sandhu, thank you for being a role model of academic excellence. To my mother and father-in-law, thank you for accepting me into your family. To all my friends, you guys keep me sane. Participating in various acts of debauchery has been the highlight of my life.

To all of my music teachers, thank you for sharing with me the gift of percussion. Your examples have shown me that one path to nirvana is through musical dedication. Without this gift, I see no point in existence. To Mr. Jim, even though our time together was brief, I will always remember you. To Greg, thank you for your excellent tutelage. To all my colleagues from high school drum line, I will always remember all of the fun we had. To Matt, Tony, Saul, Kevin, and Mike, my time with you guys have taught me a great deal about percussion and the virtue of discipline that has permeated to all other aspects of my life. To Amratpal Singh, Kishor, Vinod, Dr. Sachdeva, and John, thank you for sharing your love and knowledge of Indian music. To all the members of the NAO, playing music with your guys is a blessing.

Last, I thank my soul mate KeFei Duan. You are my moon and stars, and I love you more than the world. You have filled my life with happiness that no words can describe. I can not imagine life without you at my side. I can not imagine life without me at your side. Only together do I feel whole. I can not speak of my self without thinking of you. Through the decade that we have known each other, my love for you has only grown. You are my best friend and my closest confidant. I thank you for overlooking my shortcomings and seeing beauty in my soul. You have always supported me when I have been discouraged. You have relied on my shoulder when your eyes have been full of tears. Until my last day, I will always love you.

TABLE OF CONTENTS

Dedication	ii
Acknowledgments	iii
List of Tables	x
List of Figures	xvi
Chapter 1 Introduction	1
1.1 What is Cancer?	2
1.1.1 Classifying Cancer	2
1.1.2 Cancer Risk	3
1.2 American Breast Cancer Statistics	4
1.3 Breast Anatomy and Cancer Detection	5
1.3.1 Palpation and Mammography	6
1.3.2 Hand-Held Ultrasound	7
1.4 Ultrasound Tomography	9
1.5 Previous Contributions to Waveform Tomography	11
1.5.1 Geophysics Applications	12
1.5.2 Medical Applications	12
1.6 Problem Statement	13
1.7 Dissertation Outline	15
Chapter 2 Physics of Wave Propagation	17
2.1 Formulation of the Wave Equation	17
2.1.1 Euler's Equation	17
2.1.2 Sound Waves	18
2.2 Wave Equation	21
2.2.1 Solution of the Wave Equation	21
2.2.2 Incorporating Attenuation: Complex Sound Speed	23
2.2.3 High Frequency Ray Approximation	25

Chapter 3 Numerical Forward Modeling	27
3.1 Discretization	28
3.2 Matrix Solution	30
3.3 Discussion	31
3.3.1 Attenuation: Relationship Between Q and Power Loss	31
3.3.2 Reflections From Boundary	32
3.3.3 Comparison of Analytical Solution and Numerical Approximation	33
Chapter 4 Inverse Problem	36
4.1 Cost Function	36
4.2 Linearization of the Cost Function	37
4.3 Gradient Descent Method	38
4.3.1 Starting Model and Phase Mismatch	40
4.3.2 Calculating the Gradient	40
4.4 Numerical Reconstructions: Accuracy and Resolution Analysis	42
4.4.1 Methods: Experiment 1	43
4.4.2 Results and Discussion: Experiment 1	45
4.4.3 Methods: Experiment 2	49
4.4.4 Results And Discussion: Experiment 2	51
Chapter 5 Acquisition Hardware, Signal Processing, and Other Practical Considerations	54
5.1 Acquisition Hardware	54
5.2 Signal Processing	55
5.2.1 Acquired Ultrasound Data	55
5.2.2 Time Windowing	57
5.2.3 Exponential Damping	57
5.2.4 Waveform Selection	58
5.2.5 Fourier Transformation	59
5.2.6 Transducer Response	60
5.2.7 Source Signal Estimation	60

5.3	Other Practical Considerations	61
5.3.1	Slice Thickness and Vertical Beam Profile	61
5.3.2	Number of Transducer Elements	62
5.3.3	Convergence Based on the Accuracy of the Starting Model	64
5.3.4	Computation Time	66
Chapter 6	In Vivo Sound Speed Imaging	69
6.1	Comparison of Waveform and Travel Time Tomography	69
6.1.1	Physical Phantom Results	69
6.1.2	Artifacts	72
6.1.3	In Vivo Results	73
6.2	Comparison to MRI	78
Chapter 7	Clinical Use	84
7.1	Methods	84
7.1.1	Patient Selection	84
7.1.2	Quantitative Sound Speed Analysis	85
7.1.3	Qualitative and Area Comparison to Other Imaging Modalities	86
7.1.4	Clinical Application	88
7.2	Results and Discussion	88
7.2.1	Quantitative Sound Speed Analysis	88
7.2.2	Case 1 - Small Cancer in Younger Female with Scattered Density (SV029)	89
7.2.3	Case 2 - Multiple Fibroadenomas in Younger Female with Heterogeneous Density (SV162)	92
7.2.4	Case 3 - Benign Cyst in Older Female with Scattered Density (SV113)	94
7.2.5	Case 4 - Benign Cysts in Older Female with Extremely Dense Breasts (SV077)	96
7.2.6	Case 5 - Large Cancer in Older Female with Extremely Dense Breasts (SV161)	98
Chapter 8	Conclusions	101

Appendices	105
Chapter A Finite Difference Stencil	105
A.1 Real and Imaginary Parts of Slowness and its Derivatives	105
A.2 S Matrix: Interior Points	105
A.3 S Matrix: Boundary Points	106
A.4 S Matrix: Corner Points	107
A.5 Derivative of S Matrix: Interior Points	108
A.6 Derivative of S Matrix: Boundary Points	109
A.7 Derivative of S Matrix: Corner Points	109
A.8 Example of Matrix Representing Finite Difference Stencil	110
Chapter B Inverse Problem	111
B.1 Line Search Estimation	111
B.2 Cost Function Gradient	112
B.3 Gradient Example	113
Chapter C Common Shot Gathers and Frequency Spectrums	116
References	121
Abstract	131
Autobiographical Statement	132

LIST OF TABLES

- 6.1 Comparison of Reference Values (m/s) to Travel Time and Waveform Tomography Reconstructions of Breast Phantom. Values are reported using the mean sound speed μ in the ROI and the corresponding standard deviation σ . 71
- 7.1 Sound Speed Analysis of Various Tissue Types. The average background enhancement is with respect to the surrounding fibroglandular tissues. . . . 88

LIST OF FIGURES

1.1 Breast Anatomy. (1) Chest wall. (2) Pectoralis muscles. (3) Lobules. (4) Nipple. (5) Areola. (6) Milk duct. (7) Fatty tissue. (8) Skin.	5
1.2 Mammography. (a) Data acquisition. (b) Example of x-ray attenuation image.	6
1.3 Hand-Held Ultrasound (a) Example of reflection or B-mode image. (b) Example of reflection or B-mode image from another scan at a later time corresponding to the approximate location in (a). (c) Data acquisition.	8
1.4 Ultrasound Tomography Breast Placement and Patient Scan. (a) Breast in ring. (b) Data acquisition.	10
1.5 Ultrasound Tomography Scan of Small Benign Cysts in a Dense Breast. (a) Reflection. (b) Sound speed (m/s). (c) Attenuation (dB/mm).	11
1.6 Ultrasound Tomography Transducer Ring Configuration.	13
2.1 Acquisition Geometry. The domain Ω with boundary $\partial\Omega$ has a transducer ring Γ with γ evenly spaced transducers that act as sources and sinks of ultrasound radiation. A breast Ω' is placed in Γ . The coordinate vector is \mathbf{r} and the vector denoting the location of a transducer is \mathbf{r}' . At a particular transducer location γ , $\mathbf{r}' = \mathbf{r}_\gamma$	22
2.2 Eikonals Travel Times. Shown is the result of a finite difference modeling of the Eikonal equation of a constant background medium with an embedded high sound speed triangle. (a) Eikonals travel times. (b) Contour plots of constant Eikonals.	25
3.1 Discretized Acquisition Geometry. The domain Ω is split into an evenly spaced grid with spacing Δ . The boundary of Ω is $\partial\Omega$. A transducer ring Γ surrounds the object Ω' that will be imaged. Cartesian coordinates are sampled on the corner points $u_{m,n}$. Direction of positive and negative x and y coordinates are given in lower right hand corner of stencil.	28
3.2 Average Power Lost as a Function of Q and Frequency. (a) Power lost per unit distance. (b) Power lost per unit distance. Use the frequency f and not ω when using this figure.	32
3.3 Numerical Wave Fields. (a) Real part of numerical wave field $\text{Re}\{\mathbf{u}\}$. (b) Imaginary part of numerical wave field $\text{Im}\{\mathbf{u}\}$. (c) Log of the modulus of the numerical wave field $\log_{10} [\mathbf{u}]$. (d) Phase of the numerical wave field $\tan^{-1} [\text{Im}\{\mathbf{u}\} / \text{Re}\{\mathbf{u}\}]$	34

3.4	Comparison of Numerical and Analytical Solutions. (a) Line profile of real part of numerical wave field $\text{Re}\{\mathbf{u}\}$ and real part of Green's function. (b) Line profile of imaginary part of numerical wave field $\text{Re}\{\mathbf{u}\}$ and imaginary part of Green's function. Graphs are plotted as a function of $kr = k \mathbf{r} - \mathbf{r}' $	35
3.5	Comparison of Numerical and Analytical Solutions With Attenuation. (a) Line profile of real part of numerical wave field $\text{Re}\{\mathbf{u}\}$ and real part of Green's function. (b) Line profile of imaginary part of numerical wave field $\text{Re}\{\mathbf{u}\}$ and imaginary part of Green's function. Graphs are plotted as a function of $kr = k \mathbf{r} - \mathbf{r}' $	35
4.1	The Gradient of the Cost Function. (a) Gradient for one emitter and one receiver. (b) Accumulated gradient for one emitter and all receivers. (c) Accumulated gradient for all emitters and all receivers.	42
4.2	Numerical Phantoms True Models. (a) Heterogeneous sound speed phantom. (b) Homogeneous sound speed phantom. (c) Homogeneous attenuation phantom.	44
4.3	Reconstruction of Heterogeneous Sound Speed Phantom. (a) Waveform reconstruction. (b) Travel time reconstruction.	45
4.4	Reconstruction of Homogeneous Sound Speed Phantom. (a) Waveform reconstruction. (b) Travel time reconstruction.	46
4.5	Line Profile of Homogeneous Sound Speed Model Reconstructions. (a) Waveform reconstruction profile. (b) Travel time reconstruction profile.	46
4.6	Reconstruction of Homogeneous Attenuation Phantom. (a) Waveform reconstruction. (b) Waveform reconstruction with regularization.	48
4.7	Reconstruction of Homogeneous Attenuation Phantom. (a) Waveform attenuation reconstruction. (b) Waveform attenuation reconstruction with regularization.	48
4.8	Reconstruction of Homogeneous Attenuation Phantom. (a) Waveform reconstruction. (b) Waveform reconstruction with regularization.	49
4.9	Numerical Phantom True Models. (a) 50 mm radius 1540 m/s cylinder embedded in a 1470 m/s background. (b) Two 1 cm width 1540 m/s squares separated by 2 mm embedded in a 1470 m/s background.	50
4.10	Time Domain Waveform Tomography Data. (a) Common source gather for waves propagated through a cylindrical model. (b) Windowed waveform for a particular source receiver pair. (c) Magnitude of Fourier transform of windowed waveform.	51

4.11	Reconstruction of Cylindrical Model. 50 mm radius 1540 m/s cylinder embedded in a 1470 m/s background. Sound speed images of 5th iteration of frequency: (a) 223 kHz, (b) 358 kHz, and (c) 615 kHz.	52
4.12	Profiles of Reconstruction of Cylindrical Model. 50 mm radius 1540 m/s cylinder embedded in a 1470 m/s background. Midline profiles of 5th iteration of frequency: (a) 223 kHz, (b) 358 kHz, and (c) 615 kHz.	52
4.13	Reconstruction of Squares Model. Two 1 cm width 1540 m/s squares separated by 2 mm embedded in a 1470 m/s background. Sound speed images of 5th iteration of frequency: (a) 223 kHz, (b) 358 kHz, and (c) 615 kHz.	53
4.14	Profiles of Reconstruction of Squares Model. Two 1 cm width 1540 m/s squares separated by 2 mm embedded in a 1470 m/s background. Midline profiles of 5th iteration of frequency: (a) 223 kHz, (b) 358 kHz, and (c) 615 kHz.	53
5.1	Ultrasound Tomography Devices. (a) CURE. (b) SoftVue.	54
5.2	Ultrasound Tomography Device Transducer Rings. (a) CURE. (b) SoftVue.	55
5.3	Common Shot Gather of Scattered Density Breast. Overlaid are red crosses that are the first arrival times determined by the automatic TOF picking algorithm.	56
5.4	Processing of Raw Ultrasound Signal. Data generated by newer prototype. (a) Original waveform. (b) Processed waveform. (c) Magnitude spectrum of processed waveform.	58
5.5	Schematic of a Vertical Profile of an Ultrasound Scan.	61
5.6	Registration Problems in a Sloping Breast. Images consist alternating row of reflection envelope images and waveform sound speed images. Each vertical pair of reflection and sound speed images correspond to the same slice.	63
5.7	Varying Emitters. Reducing the number of emitters used in the reconstruction process affects the quality of the reconstructed image.	65
5.8	Convergence to a Homogeneous Sound Speed Model as a Function of the Starting Sound Speed Model and Operating Frequency.	66
5.9	Computation Time: GPU vs. CPU. The total accumulated time is displayed on the y-axis.	67

6.1	Reconstructions of Physical Breast Phantom. Data acquired by older ultrasound tomography unit. Gray scale values in the sound speed images correspond to a range of 1475–1550 m/s. Brighter areas correspond to higher sound speed. (a) Travel time tomography method. (b) Waveform tomography method. (c) Computed tomography reference with arrow overlays labeling structures: (1) Small tumor, (2) Large fat deposit, (3) Large tumor, (4) Small Fat deposit, (5) Glandular tissue, (6) Subcutaneous fat layer.	70
6.2	Comparison of Travel Time (top row) and Waveform (bottom row) Reconstruction Methods. Data acquired using older ultrasound tomography unit. Gray scale values in the sound speed images correspond to a range of 1400–1575 m/s. Brighter areas correspond to higher sound speed. (a) Complex parenchyma shape. (b) 1.5 cm tumor. (c) 4 cm tumor (1 o'clock) and parenchyma (9 o'clock).	74
6.3	Comparison of Travel Time (top row) and Waveform (bottom row) Reconstruction Methods. Data acquired using newer ultrasound tomography unit. Gray scale values in the sound speed images correspond to a range of 1400–1575 m/s. Brighter areas correspond to higher sound speed. (a) Very fine parenchyma patterns. (b) 1 cm tumor (10 o'clock). (c) 4 cm tumor (3 o'clock).	76
6.4	Vertical Line Profile Through the Tumor in Figure 6.3(c)	77
6.5	Saline Breast Implant Reconstructions. Gray scale values in the sound speed images correspond to a range of 1450–1550 m/s. Brighter areas correspond to higher sound speed. (a) Waveform tomography method. (b) Travel time tomography method.	77
6.6	Comparison of Waveform Tomography Reconstruction to MRI. Combinations of numbers and arrows indicate the corresponding tissues for comparison. Data was acquired by the old prototype. (a) Waveform sound speed; (b) MR slice with corresponding parenchyma; (c) MR slice with corresponding tumor.	79
6.7	Comparison of Waveform Tomography Reconstruction to MRI. Combinations of numbers and arrows indicate the corresponding tissues for comparison. Data was acquired by the old prototype. (a) Waveform sound speed; (b) and (c) Corresponding MRI slices.	79
6.8	Comparison of Waveform Tomography Reconstruction to MRI. Combinations of numbers and arrows indicate the corresponding tissues for comparison. Data was acquired by the new prototype. Gray scale values of the waveform tomography image have been inverted to better match the MR image. (a) Waveform sound speed; (b) Waveform sound speed; (c) MR slice with corresponding tumor and parenchyma.	80

6.9	Comparison of Waveform Tomography Reconstruction to MRI. Combinations of numbers and arrows indicate the corresponding tissues for comparison. Data was acquired by the new prototype. Gray scale values of the waveform tomography image have been inverted to better match the MR image. (a) Waveform sound speed; (b) Corresponding MRI slice; (c) Waveform sound speed; (d) Corresponding MRI slice.	81
6.10	Series of MR and Waveform Tomography Sound Speed Images. Images consist of alternating rows of MR images and waveform sound speed images. Each vertical pair of MR and sound speed images correspond to approximately the same location in the patient.	83
7.1	Directional References. Schematic of body planes and commonly used terminology to describe anatomic location.	85
7.2	Images Corresponding to Case 1. (a) Cranial-Caudal mammogram. (b) Hand-Held ultrasound. (c) Waveform sound speed re-sampled in sagittal plane. (d) MRI. (e) Waveform sound speed with inverted gray scale.	90
7.3	Images Corresponding to Case 2. (a) Hand-Held ultrasound. (b) Reflection envelope. (c) Waveform sound speed. (d) Waveform sound speed with preferential window and leveling.	93
7.4	Images Corresponding to Case 3. (a) Mediolateral Oblique Mammogram. (b) Hand-Held ultrasound. (c) Waveform sound speed. (b) Reflection envelope.	95
7.5	Images Corresponding to Case 4. (a) Cranial-Caudal mammogram. (b) Hand-Held ultrasound. (c) Waveform sound speed. (b) Reflection envelope.	97
7.6	Images Corresponding to Case 5. (a) Mammogram. (b) Hand-Held ultrasound. (c) Waveform sound speed.	99
A.1	Finite Difference Stencil. Field values $u_{m,n}$ are sampled on the corner points.	106
B.1	Surface and Contour Lines Representing the Cost Function $f(\mathbf{x})$. Lines representing the system of equations intersect at the minimum point of $f(\mathbf{x})$	114
C.1	Common Shot Gather of Water Shot. Overlaid are red crosses that are the first arrival times determined by the automatic TOF picking algorithm.	117
C.2	Common Shot Gather of Scattered Density Breast. Overlaid are red crosses that are the first arrival times determined by the automatic TOF picking algorithm.	117

C.3	Common Shot Gather of Dense Breast. Overlaid are red crosses that are the first arrival times determined by the automatic TOF picking algorithm. . . .	118
C.4	Preprocessed Common Shot Gather of Scattered Density Breast. Overlaid are red crosses that are the first arrival times determined by the automatic TOF picking algorithm.	118
C.5	Preprocessed Common Shot Gather of Dense Breast. Overlaid are red crosses that are the first arrival times determined by the automatic TOF picking algorithm.	119
C.6	Magnitude Spectrum of Preprocessed Common Shot Gather of Water Shot. .	119
C.7	Magnitude Spectrum of Preprocessed Common Shot Gather of Scattered Density Breast.	120
C.8	Magnitude Spectrum of Preprocessed Common Shot Gather of Dense Breast.	120

CHAPTER 1: Introduction

The purpose of this work is to produce high resolution quantitative *in vivo* sound speed images of the human breast for aiding in the detection and diagnosis of breast cancer. Breast cancer is the second-leading cause of cancer death of American women.[1] Early detection is the best known means for reducing cancer mortality. Mammography, as a screening tool, generates many abnormal findings not related to cancer which generate additional imaging procedures. More effective screening and diagnosis tools are urgently needed for the early detection of breast cancer. Tomographic imaging techniques in ultrasound show tremendous potential to detect and diagnose early stage breast cancer.

In this work, we focus on the reconstruction of the sound speed of breast tissue using waveform tomography techniques. Waveform tomography reconstruction algorithms model the propagating wavefields using the full wave equation, hence taking into account higher order effects such as diffraction and multiple scattering [2]. This is in contrast to more common travel time (or ray) tomography techniques which only consider the arrival times of transmitted wavefronts [3]. A limitation of our approach is that we model 2D wave propagation which neglects the out of plane scattering present in real data acquisition. However, this approach has significant advantages in terms of computational speed, complexity of hardware, and chest wall access. It is also mitigated by the fact that the considered transducer ring focuses most of the acoustic energy in the coronal plane. By careful data-fitting of the numerical wavefields to real acoustic data, we solve the inverse problem to iteratively produce sound speed models of the breast. We start from an initial estimate of the sound speed model and update it using conventional gradient descent methods. The iterations stop when a convergence criterion is satisfied. The computation of the simulated wave field for a given sound speed model is achieved through forward modeling. The update of the sound speed model based on the computed measurement mismatch is obtained by solving the cor-

responding inverse problem. The improved image quality enabled by waveform tomography has the potential to significantly increase the clinical value of these images for the detection and diagnosis of breast cancer. We will show that the radical improvements in contrast and resolution over previous travel time methods improve the shape and margins of structures. For example, by using the waveform tomography technique, there are great improvements in the differentiation of benign masses, malignant masses, and cysts from the bulk breast parenchyma. The results obtained by ultrasound waveform tomographic techniques mirror the capabilities of modalities such as MRI. By using the waveform tomography technique, there is potential to improve the clinical assessment of breast disease.

1.1 What is Cancer?

Medical imaging techniques can reveal information not visible to the naked eye. This can range from the size of bone fractures to the gender of a fetus. Medical imaging can also be used to detect the presence and the extent of malignancy of diseases such as cancer. Cancer is a term used to describe a wide group of diseases that cause cells to divide and multiply uncontrollably [4, 5]. The resulting growth is called a neoplasm or the more colloquial term tumor. The uncontrolled growth is due to problems with genes that both encourage and discourage cell division. Cell division is encouraged by proto-oncogenes, but when they are damaged, they may become oncogenes which encourage cells to divide uncontrollably. As cells undergo their usual processes of growth and division, mutations may result. Tumor suppression genes would typically cause these cells to die in a process called apoptosis. When damaged, the genes fail to regulate cell division.

1.1.1 Classifying Cancer

There two types of tumors: malignant and benign. Benign tumors are typically identical to normal tissues. They are simply capsular overgrowths of normal tissues and are most likely not fatal. Some examples of benign tumors include fluid-filled cysts and mass-like fibroadenomas. Malignant tumors may result in fatalities. Malignant tumors are destructive

because they consume oxygen that would otherwise go to healthy tissues. Healthy tissues would starve and die undergoing necrosis. Malignant tumors are morphologically different from benign tumors in that they are invasive and branch out to adjacent normal tissues. They do not recognize tissue boundaries and can move or metastasize throughout the body. Malignant tumors cease to resemble their parent cells. They are said to be poorly differentiated.

The degree to which a tumor has developed is quantified by grading [6]. The TNM (tumor-node-metastasis) grading scale is used to describe the degree of malignancy of a tumor. Scores of 0-4, 0-3, and 0-1 are given to each subcategory, respectively. Higher numbers indicate a worsening prognosis. A score of "X" is given if the minimum requirements for classification have not been met. The tumor, node, and metastasis scores describes the size of the primary tumor and the extent to which it has spread to adjacent structures, the spread of malignancies to regional lymph nodes close to the primary tumor, and the spread of malignancies to other parts of the body, respectively.

Breasts are also classified into their respective densities using, for example, the BI-RADS criteria for mammographic density [7]. This results in four distinct and qualitative classifications for breast density: (1) almost entirely fatty, (2) scattered areas of fibroglandular density, (3) heterogeneously dense, and (4) extremely dense.

1.1.2 Cancer Risk

Screening is essential to finding tumors when they are small and still *in situ* or locally constrained. Age is the most important factor in cancer incidence. Older people are at a higher risk. It has been shown that people with healthy lifestyles with good diet and exercise have lower incidences of cancers. Chemicals and substances known as carcinogens induce cancer formation. These can range from the charred lamb kabobs to industrial insulators such as asbestos. Smoking and the consumption of drugs such as alcohol and tobacco also increase the likelihood of cancer incidence. There are differences in genes that predispose certain individuals to form cancers. For example, breast cancer risk is higher for individuals

with family history. Differences in genes among the people of different regions of the world might also contribute to the incidence of cancers. For example, it has been shown that Asians and sub-Saharan Africans have a lower risk of forming cancers.

1.2 American Breast Cancer Statistics

Information about American breast cancer statistics has been compiled in [1]. In 2011, 230,480 new incidences of breast cancer and 39,520 deaths were expected. Women over the age of 50 accounted for 78% and 87% of these numbers, respectively. New incidence rates increased in the 1980s due to the invention of mammography screening and a decline in pregnancy rates. They further increased during the 1990s possibly due to further increases in mammography screening as well as the use of menopausal hormones. A sharp decrease of 7% was noted in 2002 when a report detailing the harms of menopausal hormones was published. Mortality rates increased steadily at a rate of 0.4% per year from 1975–1990 reaching 50,000 deaths per year. The rate has steadily declined at a rate of 2.2% per year due to increased screening and treatment options.

There is a disparity in incidence and survival rates based on state, socioeconomic class, and ethnicity. Asian American/Pacific Islanders had the lowest rate of new incidences (84.9 new cases per 100,000 women). Non-Hispanic whites had the highest rate (125.4 new cases per 100,000 women). Mortality rates were lowest among Asian American/Pacific Islanders (12.2 deaths per 100,000 women). The highest mortality rate is among African American women (32.4 deaths per 100,000 women). This disproportionately higher rate reflects differences in socioeconomic status which leads to a lack of early screening. This is particularly evident in the fact that new incidence rates are higher in non-Hispanic white women when compared to African American women (125.4 and 116.1 cases per 100,000 women, respectively), yet they have lower mortality rates when compared to African American women (23.9 and 32.4 cases per 100,000 women, respectively). The variation in cancer in different ethnicities might also arise from molecular differences in tumor biology. Within a state, there is disparity among counties according to the level of poverty. The mortality rate is

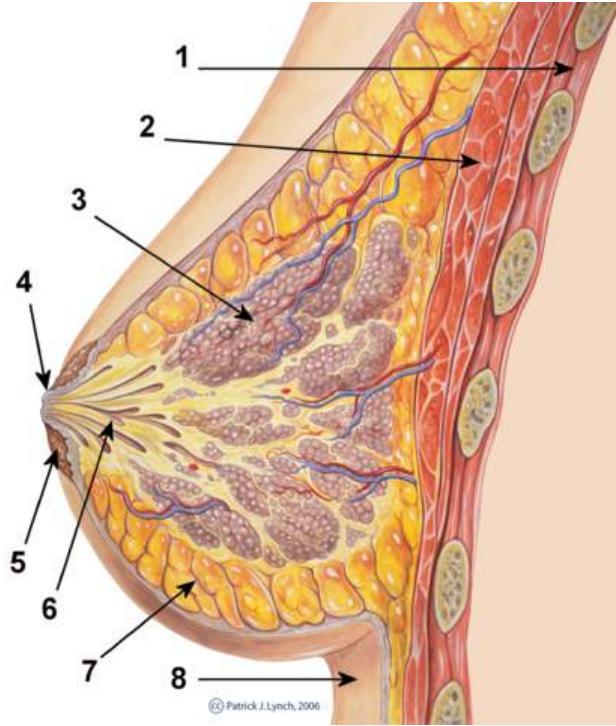


Figure 1.1: Breast Anatomy. (1) Chest wall. (2) Pectoralis muscles. (3) Lobules. (4) Nipple. (5) Areola. (6) Milk duct. (7) Fatty tissue. (8) Skin.

proportional to the level of poverty.

1.3 Breast Anatomy and Cancer Detection

A human female breast is composed of a matrix of adipose and fibrous tissues surrounding mammary lobules. The lobules are composed of secretory ducts which converge at the nipple. The fibrous tissue, or parenchyma, connects and holds the breast together. The breast connects to the rest of the body at the pectoralis muscle which is connected to the chest wall. An image displaying these and other relevant structures is seen in Figure 1.1 [8]. Since the breast is composed of soft tissues, it is an ideal candidate for ultrasound tomography. Note that the chest wall and corresponding muscles can corrupt image quality by entering in to the field of view of the ultrasound tomography scanner (for an example, see image closest to chest wall in Figure 6.10). Early detection of breast disease can lead to significant reduction in the mortality rate [9]. The detection of breast cancer is multi-modal.

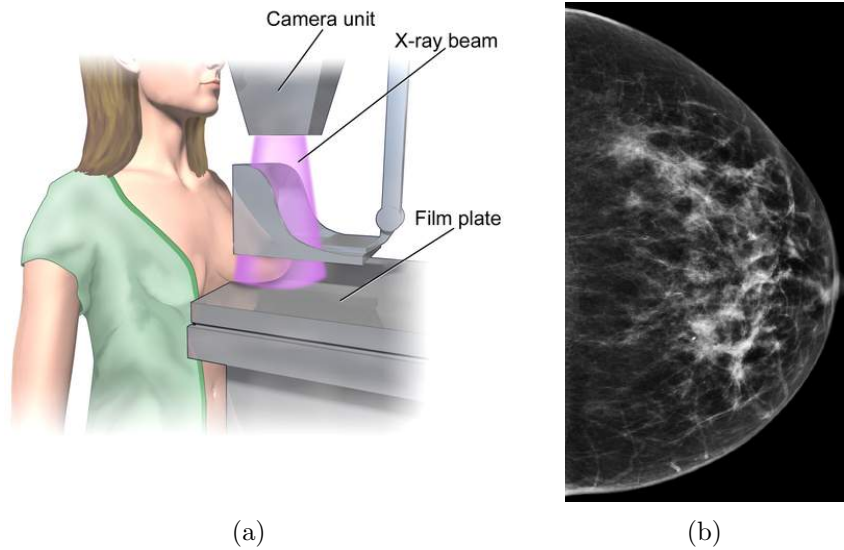


Figure 1.2: Mammography. (a) Data acquisition. (b) Example of x-ray attenuation image.

1.3.1 Palpation and Mammography

The first line of defense uses self examination and palpation of the breasts. The problem with self palpation is that it would typically only find suspicious lumps after they have grown to a sizable volume. However, a women doing regular breast self examination would on average find a tumor of approximate size 2 cm as opposed to a finding a tumor of approximate size 3.5 cm by accident [10]. The typically screening modality associated with breast cancer detection is mammography. It has shown to be an effective tool in reducing mortality associated with breast cancer [11]. An illustration of a mammogram acquisition is seen in Figure 1.2(a) [12].

In mammography, a patient places a breast in between plates that compress the breast. Diagnostic ionizing x-rays are then used to scan the breast typically resulting in two planar projections characterizing the photoelectric attenuation properties of the breast anatomy [13]. An example image is seen in Figure 1.2(b). The resulting shape of the imaged structures is then used to assess the presence of breast disease. For a good introduction to reading and interpreting mammograms, the reader is referred to [14]. The reader will find that to first order, malignant cancers are defined by indistinct or “fuzzy” margins (or borders) while benign tumors have more round or smooth shape. When using mammography, a mass of

average size 1.6 cm is found by a woman's first mammogram while a mass of average size 1.2 cm is found when previous mammograms are available for comparison. Thus, the best method to detect breast cancer early as possible would use a combination of high-quality mammograms which are the gold standard for cancer screening and a *clinical* breast exam performed by a physician [15]. Routine mammographic screening every one or two years is recommended for women age forty or older [9] although there is some debate on the most effective age of beginning participation [16, 17, 18].

Problems exist with the effectiveness of screening mammography [19]. The extent of the ability for screening mammography to improve the quality of life of a patient is debatable [20, 21]. For example, a false-positive mammographic finding usually results in an unneeded biopsy or subsequent imaging with another modality such as hand-held ultrasound. This adds a great deal of anxiety and expense for the patient as well as expense to the health care system. False-positives can also lead to overdiagnosis [22]. Cancers such as some forms of Ductal Carcinoma In Situ (DCIS) are stable diseases related to the presence of microcalcifications and will not become metastatic [23]. Finding these cancers by an imaging method will lead to their removal even though they might not be potentially hazardous. Another problem associated with mammography is the presence of mammographically occult lesions in dense breasts who often times are in young women [24]. The extensive parenchyma and fibrous tissue present in these types of breasts hinder the ability of a radiologist to make an accurate diagnosis of breast disease based on morphology. If a patient is young, she would be also less likely to be seek cancer screening or perceive a risk to the disease. Another prevalent problem with mammography is the use of painful compression that can lead to a reduction in women seeking screening. Due to many of the problems listed above, we are motivated to find an adjunct or replacement to mammography.

1.3.2 Hand-Held Ultrasound

A very effective tool at increasing the specificity of mammography is given by the use of hand-held ultrasound [25, 26, 27]. Hand-Held ultrasound is the precursor to our ultrasound

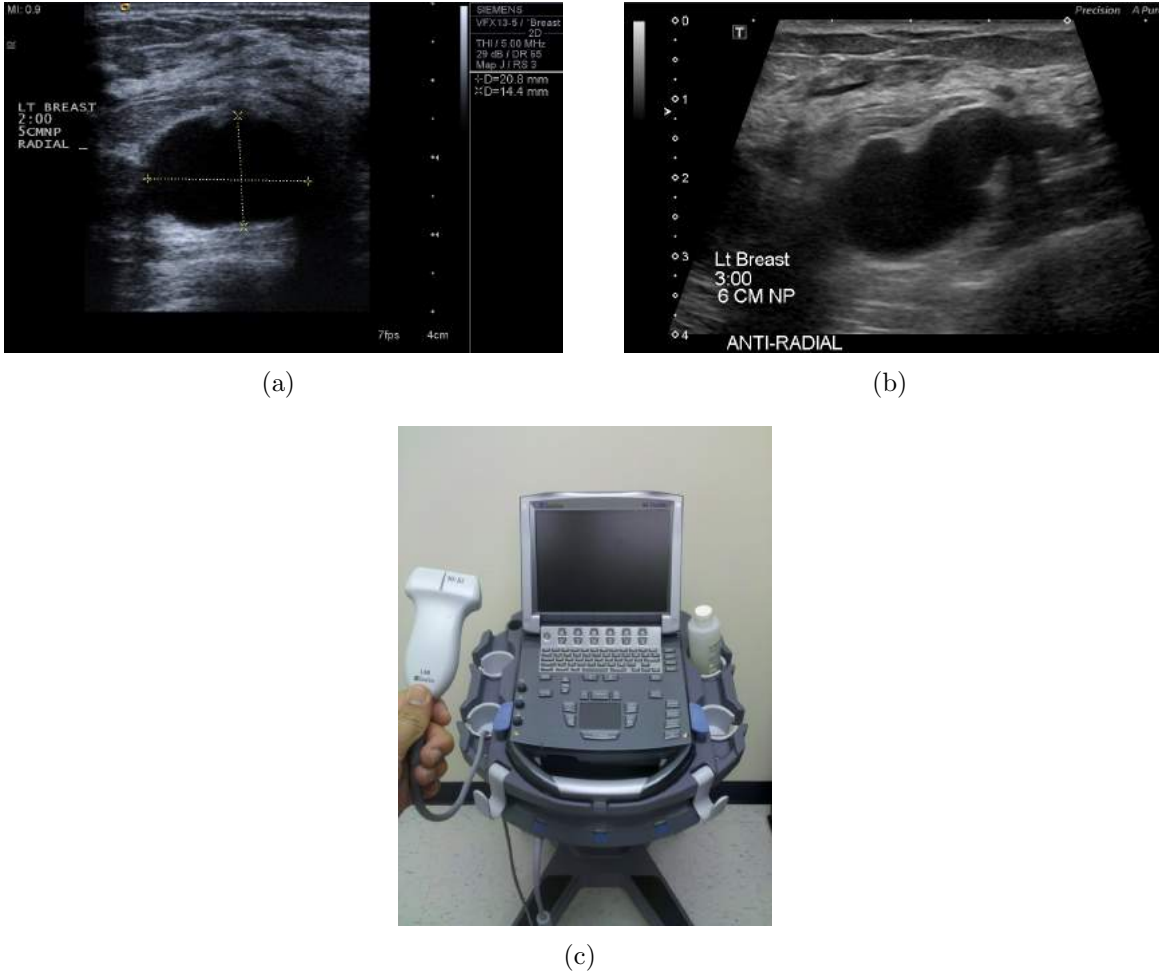


Figure 1.3: Hand-Held Ultrasound (a) Example of reflection or B-mode image. (b) Example of reflection or B-mode image from another scan at a later time corresponding to the approximate location in (a). (c) Data acquisition.

tomography method. A hand-held ultrasound probe consists of a linear or curvi-linear ultrasound transducer array that is typically attached to processing hardware and an imaging workstation. An example is seen in Figure 1.3(c). An impedance matching acoustic coupling gel is applied to a patients skin before it scanned by the probe. This type of reflection based ultrasound scanning measures the variation of the impedance $Z = \rho c$ of the breast where the density and the sound speed of the breast are ρ and c , respectively [28]. For example, a signal originating from a medium with impedance Z_1 and reflecting at a normal incidence from a medium with impedance Z_2 would have a reflection coefficient $R = (Z_2 - Z_1)^2 / (Z_2 + Z_1)^2$. An example of the reflection or B-mode image of a breast is seen in Figures 1.3(a) and 1.3(b).

The hand-held ultrasound scan is highly dependent on the expertise of the operator as they must search through tissue and visualize and calibrate the 2D image on the imaging workstation with the scanned anatomy. An example of this is seen in the B-mode ultrasound breast images in Figure 1.3. One image was acquired in the radial breast plane while the other was acquired in the anti-radial plane (see Figure 7.1(c)). The lesion location, i. e. distance from nipple and clock position, should be roughly the same for both images. The fact that the images look very different gives an example of the operator dependence of hand-held ultrasound. The reader is referred to [29] for a basic introduction to hand-held ultrasound. For the interpretation of sonographic findings, the reader is referred to [26] which does an extensive analysis of benign and malignant findings in ultrasound breast scans. As was the case for mammography, the reader will find that malignant tumors generally have more diffuse shape and indistinct margins when compared to benign cases. It is important to understand that the shape and margins of tumors carry vital diagnostic information which can directly characterize breast disease. If the classification is robust and not marred by false-positives, then unneeded biopsies can be reduced. Due to the operator dependence of hand-held ultrasound and its ability to accurately characterize benign and malignant lesions, we are motivated to image with ultrasound tomography.

1.4 Ultrasound Tomography

Ultrasound tomography is an ideal technique for obtaining 3D images of breast structures since the breast is comprised mostly of soft tissues without bones or other materials which would strongly scatter and attenuate transmitted signal energy [30]. Potential clinical benefits of ultrasound tomography include safety, comfort, and 3D imaging. This is in contrast to existing clinically accepted modalities, such as x-ray mammography, which only provides planar projections, involves ionizing radiation, and uses uncomfortable compression.

Many researchers have made important contributions to the field of ultrasound tomography. Early work focused on using tomographic techniques for reflection imaging [31]. A fundamental benefit of ultrasound tomography techniques over traditional hand-held ultra-

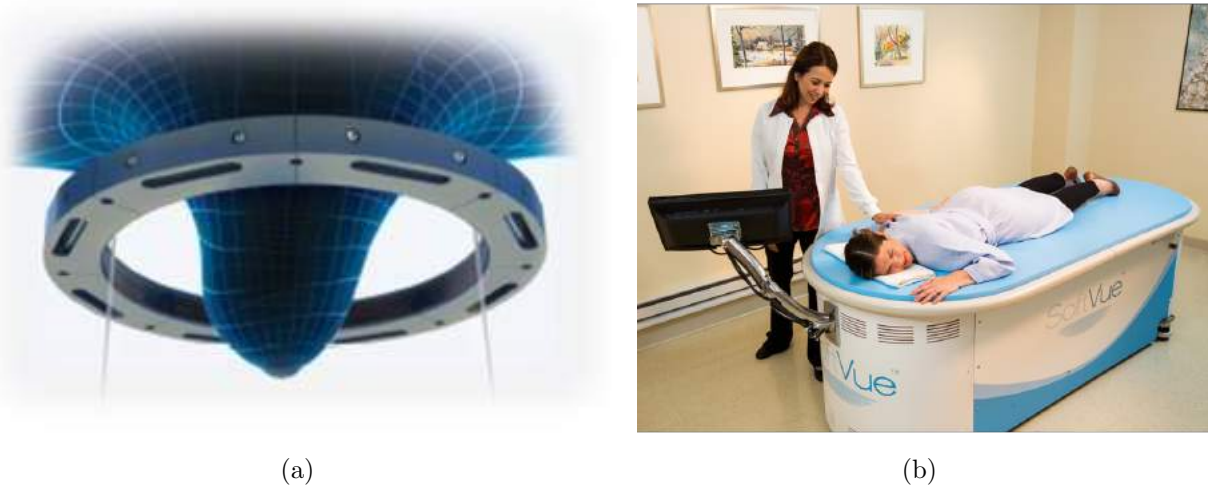


Figure 1.4: Ultrasound Tomography Breast Placement and Patient Scan. (a) Breast in ring. (b) Data acquisition.

sound is the ability to use the transmitted ultrasound wave field. This is important because the transmitted portion of an ultrasound signal contains information about the sound speed and attenuation properties of the insonified medium [32, 33, 34, 35]. These properties can aid in the differentiation of fat, fibro-glandular tissues, benign masses, and malignant cancer. A few examples of research groups that have made contributions to transmission ultrasound tomography include [36, 37, 38, 39, 40, 41].

The two ultrasound tomography devices used to generate data for this work [42, 43] operate in a similar fashion. During an exam, the patient lies prone on a table and inserts a breast into a ring transducer which is immersed in a water filled chamber. Examples of a patient exam and the placement of the breast are seen in Figure 1.4. The ring transducer then scans the entire breast acquiring coronal slices from the chest wall to the nipple region. Tomographic reflection or B-mode images are then reconstructed from the reflected signals while sound speed and attenuation images are reconstructed from the transmitted signals. The three image types can then be used to evaluate the presence of breast disease. The B-mode images are qualitative reconstructions which measure the variations in the impedance properties of the breast tissue [44]. They provide useful contrast and morphological information. The sound speed and attenuation images map the sound speed (m/s) and attenuation

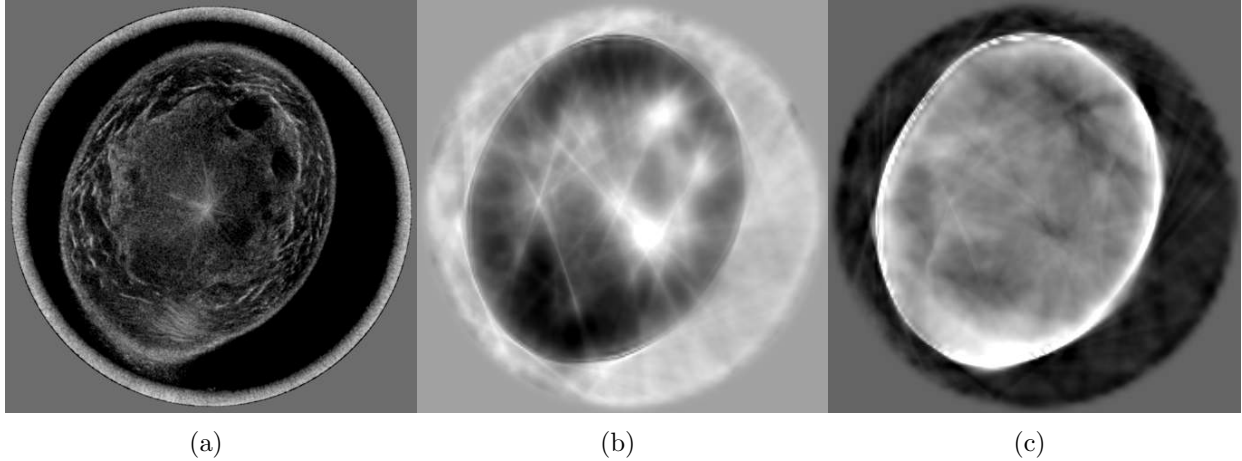


Figure 1.5: Ultrasound Tomography Scan of Small Benign Cysts in a Dense Breast. (a) Reflection. (b) Sound speed (m/s). (c) Attenuation (dB/mm).

(dB/mm) within each voxel of the reconstructed breast volume. In addition to providing contrast and morphological information, this quantitative data helps in the identification of unknown structures in an absolute and consistent way [3, 45, 46]. An example of a scan of small benign cysts in a very dense breast is seen in Figure 1.5. It can be seen that the hypoechoic cyst locations correspond to regions of higher sound speed and lower attenuation. The sound speed of breast can also be a quantitative surrogate marker for the evaluation of breast density which would be useful since women with dense breasts are at an increased risk for breast cancer due to increased incidence and reduced diagnosis [47, 48, 49, 50]. Thus, waveform tomography can be used to assess the possible cancer risk to young women as well as monitoring the progression of benign or malignant breast disease without having to subject the patient to repeated doses of ionizing radiation.

1.5 Previous Contributions to Waveform Tomography

In the preceding decades, various research teams have made significant advances in waveform tomography. These include extensive research in Geophysics as well as limited study in medical applications. Sound scales fairly linearly across the frequencies used in these applications. For example, Geophysics uses sound waves with frequencies on the order of Hz to image the Earth's subsurface where relevant length scales are on the order of km. In

contrast, medical ultrasound uses MHz signals to image structures with length scales of mm. Thus, Geophysics waveform tomography techniques can be utilized in medical applications.

1.5.1 Geophysics Applications

The most important contributions to waveform tomography arose from research in the field of Geophysics. A major subset of this field includes the study and investigation of seismic waveforms. As these waveforms travel through the earth, they are modified and perturbed according to the elastic properties of the Earth. The received waveforms can then be used to deduce the elastic properties which caused the modifications. For example, as in B-mode ultrasound imaging, one can map the reflective properties of the interior of the Earth by using the principles of migration [51]. A method to iteratively update a sound speed model by perturbations developed from a least-squares minimization of a cost function was developed in [52, 53]. The authors recast the principles of migration to show that the sound speed model was updated by using the gradient of the cost function where the perturbations were given by correlating the forward propagated wave field with the backward propagated data residual. An example of a numerical result in the time domain is given in [54] while a numerical result in the frequency domain is given in [55]. The compact matrix formalism approach and technique developed in [56] was absolutely crucial in developing our algorithm. The frequency domain approach is efficient as it allows only the inversion of a subset of the frequencies contained within the signal bandwidth [57]. Some examples of the application of waveform tomography to experimental data is given in [56, 58, 59, 60, 61, 62, 63]. An excellent review of Geophysics applications of waveform tomography is found in [2].

1.5.2 Medical Applications

While some research has investigated medical applications using numerical data sets [64, 65, 66, 67], to the best of our knowledge, very few have successfully applied these techniques to clinical *in vivo* data. The work in [39, 68] was a major pioneering contribution using an ultrasound tomography device with planar transducer arrays. Their reconstruction technique

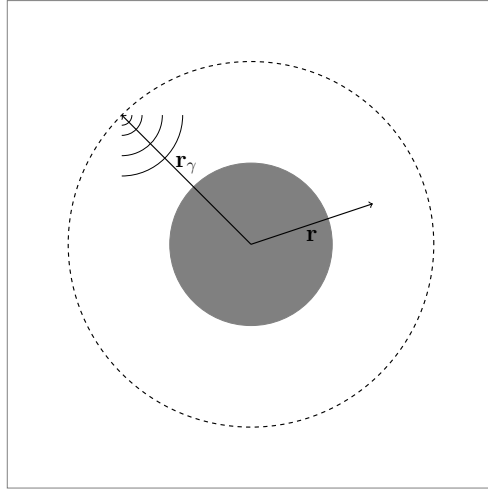


Figure 1.6: Ultrasound Tomography Transducer Ring Configuration.

contrasts sharply with ours. While [39] used an implicit integral equation technique to find the scattered wavefields, we use finite difference and matrix inversion methods using data acquired from a ring transducer. Another important contribution to waveform tomography for breast imaging is given in [69]. The authors use a very similar waveform tomography algorithm to produce sound speed and attenuation images of a physical tissue mimicking breast phantom and *in vivo* data obtained using our older ultrasound tomography unit. Their work relies on manual travel time picking to build the initial sound speed model. Manual travel time picking requires a user to look at a received waveform and decide the time-of-flight of the acoustic signal. Due to the vast amount of data collected, this approach is impossible for practical clinical applications. In contrast, our method utilizes a completely automatic time-of-flight picker which is capable of separating system noise and the arrival of the acoustic signal. We also use different preprocessing techniques in the implementation of our algorithm.

1.6 Problem Statement

Let us consider the ultrasound tomography transducer ring configuration depicted in Figure 1.6. The breast, represented by the gray circle, is immersed in water and surrounded by an ultrasound transducer ring with N_T elements (see Figure 1.4(a)). The positions of the

transducer elements are given by \mathbf{r}_γ for $\gamma = 1, 2, \dots, N_T$. Our goal is to estimate the sound speed model $c(\mathbf{r})$ as a means to quantitatively characterize breast tissue. The sound speed is assumed to be independent of the frequency (no dispersion). Reconstructing the sound speed model of the breast is an inherently 3D problem. However, since our ring transducer focuses most of the transmitted energy in the acquisition plane, we will reconstruct the breast volume as a series of 2D coronal slices. The inter-slice spacing can be adjusted as a function of the vertical transducer beam width to ensure full coverage (with possible overlap). Note that attenuation can easily be included by adding an imaginary component to the sound speed model [58, 70]. The sound speed model is sampled on an uniform $N \times N$ reconstruction grid and stacked into an N^2 dimensional vector \mathbf{c} .

The acquisition works as follows. Each transducer element sequentially emits an ultrasound pulse which propagates throughout the medium. In the frequency domain, the transmitting pulse given by the transducer operating at frequency ω is given by complex valued quantity $s(\omega)$, and the resulting complex wave field at position \mathbf{r} is denoted $d(\mathbf{r}, \omega)$. The wave field is measured at the transducer locations \mathbf{r}_γ , giving complex valued experimental measurements $d(\mathbf{r}_\gamma, \omega)$. The measurements obtained for all emitter-receiver pairs can be stacked into an N_T^2 dimensional vector $\mathbf{d}_{obs}(\omega)$. The expected numerical wave field obtained at position \mathbf{r} for a given operating frequency ω and sound speed model \mathbf{c} is denoted $u(\mathbf{r}, \omega, \mathbf{c})$. Similar to the experimental measurements, the simulated wave field is sampled at the transducer locations and the values are stacked in an N_T^2 dimensional vector $\mathbf{u}_{obs}(\omega, \mathbf{c})$.

The problem that we would like to solve is to estimate the sound speed model \mathbf{c} that generates, upon numerical simulation, simulated measurements $\mathbf{u}_{obs}(\omega, \mathbf{c})$ that best match the experimental measurements $\mathbf{d}_{obs}(\omega)$. More specifically, we would like to minimize the real valued mean squared error cost function

$$E(\omega, \mathbf{c}) = \frac{1}{2} \mathbf{e}^H(\omega, \mathbf{c}) \mathbf{e}(\omega, \mathbf{c}), \quad (1.1)$$

where H denotes the Hermitian transpose, and \mathbf{e} is the residual mismatch defined as

$$\mathbf{e}(\omega, \mathbf{c}) = \mathbf{u}_{obs}(\omega, \mathbf{c}) - \mathbf{d}_{obs}(\omega). \quad (1.2)$$

Note that the dependence on the frequency ω and the sound speed model \mathbf{c} is explicitly given in the above expressions to emphasize that the optimization is performed on one frequency at a time, and that the simulated wave field depends on the assumed sound speed model. In other words, if the sound speed model is updated, the simulated wave field needs to be reevaluated.

1.7 Dissertation Outline

Application of the frequency domain acoustic wave equation on data acquired from ultrasound tomography scans is shown to yield high resolution sound speed images on the order of the wavelength of the highest reconstructed frequency. Using a signal bandwidth of 0.4–1 MHz and an average sound speed of 1500 m/s, the resolution is approximately 1.5 mm. The quantitative sound speed values and morphology provided by these images have the potential to inform diagnosis and classification of breast disease. In this manuscript, we present the formalism, practical application, and *in vivo* results of waveform tomography applied to breast data gathered by two different ultrasound tomography scanners that utilize ring transducers. The formalism includes a review of the physics of wave propagation, frequency domain modeling of the wave equation using finite difference operators, and a review of the inverse problem as related to an iterative reconstruction scheme using the gradient descent method. We give numerical results and show that the practical application of waveform tomography requires an accurate starting model, careful data processing, and a method to gradually incorporate higher frequency information into the sound speed reconstruction. Following these steps resulted in high resolution quantitative sound speed images of the breast. These images show marked improvement relative to commonly used travel time tomography reconstruction methods. The robustness of the method is demonstrated by obtaining similar results from two different ultrasound tomography devices. We also compare our method to MRI to demonstrate concordant findings. We give examples of the possible use of waveform

tomography in a clinical setting. The clinical data used in this work was obtained from a HIPAA compliant clinical study (IRB 040912M1F). This work was partially funded by the National Institutes of Health (NIH) through National Cancer Institute grants R43CA171601 and R44CA165320.

CHAPTER 2: Physics of Wave Propagation

The topic of acoustic wave propagation in breast tissue is a subset of the field of fluid mechanics. Many resources are available to understand this topic [71, 72, 73, 74, 75, 76, 77]. We will develop some of the principal equations of fluid mechanics from fundamental physical principles and then make the appropriate considerations and approximations to yield the acoustic wave equation. We will not be nearly as rigorous in our development as in the sources cited above, but we hope that adequate justice is done to the development and presentation of the acoustic wave equation.

2.1 Formulation of the Wave Equation

2.1.1 Euler's Equation

Fluid mechanics is concerned with macroscopic phenomena and thus the breast is considered to be a continuous fluid. We then consider an *ideal* fluid particle of the breast which is large enough such that it contains many molecules, but it is smaller than other length scales considered in the problem. The fluid is *ideal* in the sense that we ignore any effects of energy dissipation that occur to internal frictional losses (viscosity) and heat exchange between different parts of the fluid. Thus, the motion of an ideal fluid is adiabatic.

We can then apply the laws of conservation of matter, momentum, and energy to a fluid particle to yield the equations of motion. From the conservation of matter, a small infinitesimal volume of fluid dV with density $\rho(\mathbf{r}, t)$ and velocity $\mathbf{v}(\mathbf{r}, t)$ obeys the continuity equation

$$\frac{\partial \rho}{\partial t} + \nabla \cdot (\rho \mathbf{v}) = 0, \quad (2.1)$$

where the spatial variable $\mathbf{r} = (x, y, z)$, the time is denoted t , and the gradient is given by ∇ . The net force acting on some arbitrary volume of fluid is related to the pressure p by

$$F_{net} = - \int_V \nabla p dV ,$$

where the integral is taken over volume elements dV within the arbitrary volume V . Thus, the equations of motion for a volume element of a fluid is given by

$$\rho \frac{d\mathbf{v}}{dt} = -\nabla p . \quad (2.2)$$

Following the steps in [72], the change in velocity $d\mathbf{v}$ can be decomposed in terms of the change in the velocity of fluid particle at a fixed point during a time interval dt as well as the difference between velocities of two points separated by a distance $d\mathbf{r}$

$$d\mathbf{v} = \frac{\partial \mathbf{v}}{\partial t} dt + (d\mathbf{r} \cdot \nabla) \mathbf{v} . \quad (2.3)$$

Inserting equation 2.3 into equation 2.2, recognizing $\mathbf{v} = d\mathbf{r}/dt$, and dividing by the density ρ yields Euler's equation

$$\frac{\partial \mathbf{v}}{\partial t} + (\mathbf{v} \cdot \nabla) \mathbf{v} = -\frac{1}{\rho} \nabla p . \quad (2.4)$$

Equation 2.4 can also be derived using the principles of conservation of momentum as shown in [74].

2.1.2 Sound Waves

Since we will be using ultrasound as a probe to image the breast, we are concerned with the propagation of sound waves. A sound wave is a small oscillatory motion in a compressible fluid that causes regions of compression and rarefaction. The fact we are dealing with small oscillations allows us to expand the pressure, density, and velocity as

$$p = p_0 + p', \quad \rho = \rho_0 + \rho', \quad \text{and} \quad \mathbf{v} = \mathbf{v}_0 + \mathbf{v}' , \quad (2.5)$$

where the constant equilibrium pressure p_0 , density ρ_0 , and velocity \mathbf{v}_0 are perturbed by a sound wave with pressure, density, and velocity variations p' , ρ' , and \mathbf{v}' ($p_0 \gg p'$, $\rho_0 \gg \rho'$, and $|\mathbf{v}_0| \gg |\mathbf{v}'|$). We can assume that in the unperturbed state, there is no net flow and

$\mathbf{v}_0 = 0$. We will obtain an expression for the acoustic wave equation by combining the continuity and Euler's equations with a first-order relation between density and pressure. The continuity equation in equation 2.1 can be written as

$$\frac{1}{\rho_0} \frac{\partial \rho}{\partial t} + \nabla \cdot \mathbf{v} + \frac{\mathbf{v} \cdot \nabla \rho}{\rho_0} = 0, \quad (2.6)$$

where we have used that since ρ' is small, $\rho^{-1} \approx \rho_0^{-1}$. Using the expansions in equation 2.5, equation 2.6 becomes

$$\frac{1}{\rho_0} \frac{\partial \rho'}{\partial t} + \nabla \cdot \mathbf{v}' + \frac{\mathbf{v}' \cdot \nabla \rho'}{\rho_0} = 0. \quad (2.7)$$

In the above expression, variations with respect to ρ_0 are zero and are omitted. Also, we can omit $\mathbf{v}' \cdot \nabla \rho'$ as this involves a small term multiplied by the derivative of a small term. Thus, equation 2.6 becomes

$$\frac{1}{\rho_0} \frac{\partial \rho'}{\partial t} + \nabla \cdot \mathbf{v}' = 0. \quad (2.8)$$

Transforming Euler's equation in equation 2.4 in a similar manner gives

$$\frac{\partial \mathbf{v}'}{\partial t} + \frac{1}{\rho_0} \nabla p' = 0, \quad (2.9)$$

where we ignore the convective acceleration $(\mathbf{v}' \cdot \nabla) \mathbf{v}'$ since soft tissue like the human breast would be lacking this phenomena, and because it is essentially a product of a small term times the derivative of a small term. In addition, the term $1/\rho$ is approximated as $1/\rho_0$. Implicit in this linearization procedure is the assumption that the velocity of a fluid particle in the wave is small compared with the velocity of sound, i. e. $|\mathbf{v}'| \ll c$. For ideal fluids (adiabatic process with constant entropy s), small changes in the pressure and density can be obtained through a Taylor expansion yielding the first order result

$$p' = \rho' \left(\frac{\partial p}{\partial \rho_0} \right)_s, \quad (2.10)$$

where $(\cdot)_s$ denotes the process is done at a constant entropy s . Thus, combining equations 2.10 and 2.8 yields

$$\frac{\partial p'}{\partial t} + \rho_0 \left(\frac{\partial p}{\partial \rho_0} \right)_s \nabla \cdot \mathbf{v}' = 0. \quad (2.11)$$

Before obtaining a wave equation, we must perform one more substitution. Introduce a scalar velocity potential $u(\mathbf{r}, t)$ by defining

$$\mathbf{v}' = \nabla u. \quad (2.12)$$

Note that in general we could consider another term $\nabla \times \Psi$ to add to equation 2.12. However, we can omit shear waves by approximated the breast to be a liquid with irrotational flow. Using equation 2.12, equation 2.9 becomes

$$p' = -\rho_0 \frac{\partial u}{\partial t}. \quad (2.13)$$

Combining equations 2.11, 2.12, and 2.13 then gives the wave equation for scalar field values $u(\mathbf{r}, t)$

$$\nabla^2 u(\mathbf{r}, t) = \frac{1}{c^2} \frac{\partial^2 u(\mathbf{r}, t)}{\partial t^2}, \quad (2.14)$$

where the sound speed c of the propagating waves is related to the pressure and density by

$$c^2 = \left(\frac{\partial p}{\partial \rho_0} \right)_s. \quad (2.15)$$

The isentropic compressibility κ_s is given by (see [78])

$$\kappa_s = -\frac{1}{V} \left(\frac{\partial V}{\partial p} \right)_s = \frac{1}{\rho} \left(\frac{\partial \rho}{\partial p} \right)_s. \quad (2.16)$$

Letting $\rho = \rho_0$, we can relate the compressibility in equation 2.16 to the sound speed in equation 2.15

$$c^2 = \frac{1}{\kappa_s \rho_0}.$$

Note that isentropic bulk modulus β_s is the inverse of the compressibility.

2.2 Wave Equation

2.2.1 Solution of the Wave Equation

For frequency domain application, we are interested in the solution of the Helmholtz equation. Transforming equation 2.14 into the frequency domain for a particular frequency ω , input sound speed distribution $c(\mathbf{r})$, and source function $s(\mathbf{r}, \omega)$ yields the Helmholtz equation

$$\left(\nabla^2 + \frac{\omega^2}{c(\mathbf{r})^2} \right) u(\mathbf{r}, \omega) = s(\mathbf{r}, \omega), \quad \mathbf{r} \in \Omega. \quad (2.17)$$

There are appropriate boundary conditions such as

$$\begin{aligned} u(\mathbf{r}) &= 0, \quad \mathbf{r} \in \partial\Omega, \quad (\text{Dirichlet}), \\ \nabla u(\mathbf{r}) \cdot \hat{\mathbf{n}}(\mathbf{r}) &= 0, \quad \mathbf{r} \in \partial\Omega, \quad (\text{Neumann}), \end{aligned}$$

where $\hat{\mathbf{n}}(\mathbf{r})$ is a unit vector normal to the boundary $\partial\Omega$. A schematic of the acquisition geometry is seen in Figure 2.1. Letting the sound speed $c(\mathbf{r})$ be a constant background sound speed c_0 , the wave number is $k = \omega/c_0$. The Green's function $g(\mathbf{r}|\mathbf{r}')$ for the Helmholtz equation then satisfies

$$(\nabla^2 + k^2) g(\mathbf{r}|\mathbf{r}') = -\delta(\mathbf{r} - \mathbf{r}'). \quad (2.18)$$

Assuming a solution with an oscillatory part $\exp[i\mathbf{k} \cdot \mathbf{r}]$, a unique solution is given by requiring a boundary condition at infinity as given by the Sommerfeld radiation condition [79]

$$\lim_{|\mathbf{r}| \rightarrow \infty} |\mathbf{r}|^{(d-1)/2} \left(\frac{\partial}{\partial |\mathbf{r}|} - ik \right) g(\mathbf{r}|\mathbf{r}') = 0,$$

where d is the dimension (i. e. 1D, 2D, 3D) and $i = \sqrt{-1}$. Many methods exist for the determination of the solution of equation 2.18. Readers are referred to [80, 81, 82, 83] for a detailed discussion of the derivation of the Green's function solution. For example, a guess to the solution can be made in terms of an eigenfunction expansion. The resulting equations can then be determined to be identical to some known function. In the case of a 2D geometry, the Green's function is given by the Hankel function of the first kind

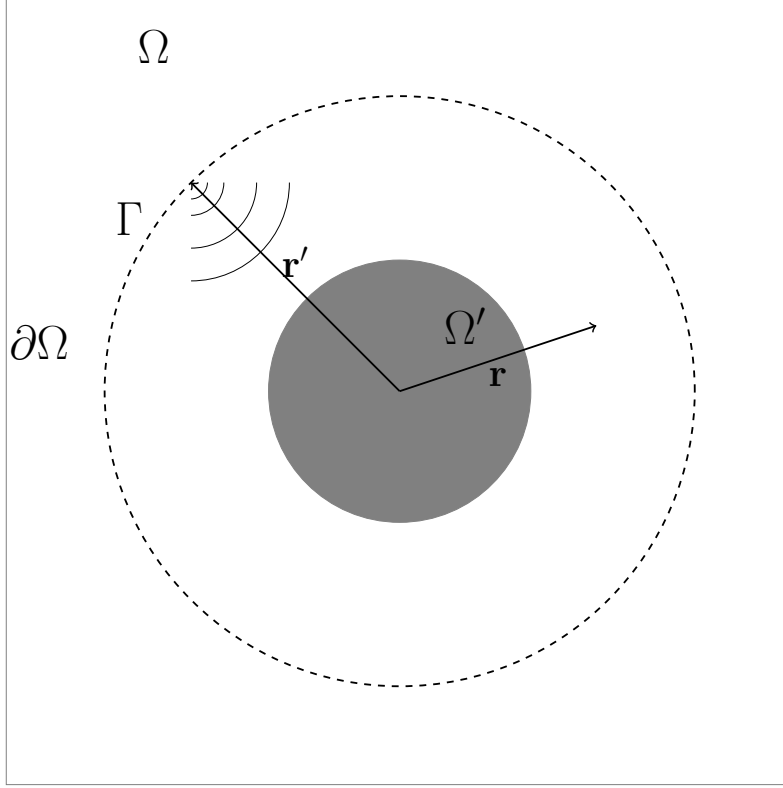


Figure 2.1: Acquisition Geometry. The domain Ω with boundary $\partial\Omega$ has a transducer ring Γ with γ evenly spaced transducers that act as sources and sinks of ultrasound radiation. A breast Ω' is placed in Γ . The coordinate vector is \mathbf{r} and the vector denoting the location of a transducer is \mathbf{r}' . At a particular transducer location γ , $\mathbf{r}' = \mathbf{r}_\gamma$.

$$g(\mathbf{r}|\mathbf{r}') = \frac{i}{4} H_0^{(1)}(k|\mathbf{r} - \mathbf{r}'|) . \quad (2.19)$$

Given a general source distribution $s(\mathbf{r}, \omega)$, the field values $u(\mathbf{r}, \omega)$ would then be obtained by using Green's second identity

$$u(\mathbf{r}) = \int_{\Omega} g(\mathbf{r}|\mathbf{r}')s(\mathbf{r}') d\mathbf{r}' + \int_{\partial\Omega} [g(\mathbf{r}|\mathbf{r}')\nabla s(\mathbf{r}') \cdot \hat{\mathbf{n}}(\mathbf{r}') - s(\mathbf{r}')\nabla g(\mathbf{r}|\mathbf{r}')] \cdot \hat{\mathbf{n}}(\mathbf{r}') dS' ,$$

where dS' is a surface element on $\partial\Omega$. We note that if we had instead used a solution with oscillatory part $\exp[-i\mathbf{k} \cdot \mathbf{r}]$ in the development of the Sommerfeld radiation condition, then a unique solution would be given by the Hankel function of the second kind: $i/4H_0^{(2)}(k|\mathbf{r} - \mathbf{r}'|)$. Further discussion of this observation and its relation to attenuation and numerical implementation can be seen in section 2.2.2 and Appendix A.3, respectively.

2.2.2 Incorporating Attenuation: Complex Sound Speed

In our development of the wave equation, we made the assumption of isentropic fluid flow. This leads to a wave equation that does not dissipate energy in the form of internal friction losses. We can then incorporate attenuation by using an ad hoc method. For example, in the time domain wave equation, attenuation can be added by adding a term $a\partial u/\partial t$ to the right hand side of equation 2.14 [64]. For the Helmholtz equation, allowing the wave number to have an imaginary component leads to evanescent waves [84]. A common practice in the field of Geophysics is to allow the sound speed to have an imaginary part [56, 58, 70]. Thus, in our problem, attenuation is introduced through the use of the use of a complex valued sound speed

$$c(\mathbf{r}) = c(\mathbf{r})_R + ic(\mathbf{r})_I ,$$

where the real part of the sound speed $c(\mathbf{r})_R$ is the phase sound speed or the typical quantity when we think of sound speed, and the imaginary part of the sound speed $c(\mathbf{r})_I$ provides viscous damping. This type of attenuation is derived from the quality factor Q , the reciprocal of which is proportional to the attenuation. The quality factor is a dimensionless measure of the intrinsic attenuation (as opposed to attenuation resulting from scattering due to velocity inhomogeneities) when a material is subject to stress at periodic intervals ω . The quality factor is defined through its relation to the loss in energy $-\Delta E$ and maximum strain energy E contained in each cycle

$$\frac{1}{Q} \equiv \frac{1}{2\pi} \frac{-\Delta E}{E} . \quad (2.20)$$

An expression for the amplitude of a signal $A(x)$ with initial amplitude A_0 moving in a medium with phase velocity c_R can be derived from equation 2.20 yielding

$$A(x) = A_0 \exp [-\alpha_Q x] , \quad (2.21)$$

with $\alpha_Q = \omega / (2c_R Q)$. We now show how the quality factor relates to c_I . Consider a plane wave $\Psi(\mathbf{r}, t)$ with a complex valued wavenumber $\mathbf{k} = \mathbf{k}_R + i\mathbf{k}_I$ as given by

$$\Psi(\mathbf{r}, t) = A_o e^{i(\mathbf{k} \cdot \mathbf{r} - \omega t)} = A_o e^{i(\mathbf{k}_R \cdot \mathbf{r} - \omega t)} e^{-\mathbf{k}_I \cdot \mathbf{r}}. \quad (2.22)$$

Note that each wavevector has a spatial decomposition in the unit bases \hat{x} and \hat{y}

$$\begin{aligned} \mathbf{k}_R &= (k_{x,R}, k_{y,R}), \\ \mathbf{k}_I &= (k_{x,I}, k_{y,I}). \end{aligned}$$

Let the wave travel from \mathbf{r} to $\mathbf{r} + \boldsymbol{\lambda}$ where we have chosen $\boldsymbol{\lambda} = \lambda \mathbf{k}_R$ and $\boldsymbol{\lambda} \cdot \mathbf{k}_R = 2\pi$. Therefore, $\lambda = 2\pi / \mathbf{k}_R \cdot \mathbf{k}_R$. Then, the change in energy of the wave, which goes like the square of the amplitude, is given by

$$\Delta E = \|\Psi(\mathbf{r} + \boldsymbol{\lambda}, t)\|^2 - \|\Psi(\mathbf{r}, t)\|^2 \quad (2.23)$$

combining equations 2.22 and 2.23

$$\frac{1}{Q} = \frac{1}{2\pi} (1 - e^{-2\mathbf{k}_I \cdot \boldsymbol{\lambda}}) \approx \frac{2\mathbf{k}_I \cdot \mathbf{k}_R}{|\mathbf{k}_R|^2} = \frac{2|\mathbf{k}_I|}{|\mathbf{k}_R|}$$

where we assumed that $|\mathbf{k}_R| \gg |\mathbf{k}_I|$ in order to expand the exponential and that $\mathbf{k}_I \cdot \mathbf{k}_R = |\mathbf{k}_I||\mathbf{k}_R|$ so that we have maximum attenuation. This assumption is reasonable as it implies $Q \gg 1$ which would imply that there shouldn't be a significant loss in energy when a wave travels a distance of a wavelength. Defining the local wave number to be $k = |\mathbf{k}_R| + i|\mathbf{k}_I|$ and using the dispersion relation $k = \omega/c$, we have

$$k = \frac{\omega}{c_R + ic_I} = \frac{\omega c_R}{c_R^2 + c_I^2} - i \frac{\omega c_I}{c_R^2 + c_I^2} = |\mathbf{k}_R| + i|\mathbf{k}_I|. \quad (2.24)$$

Thus, in order to introduce attenuation, we can give the velocity a non-zero imaginary part

$$\frac{1}{Q} = \frac{2|\mathbf{k}_I|}{|\mathbf{k}_R|} = -\frac{2c_I}{c_R},$$

with the constraint $c_I < 0$ in order for $Q > 0$. Comparing equations 2.21 and 2.24

$$\alpha_Q = -\frac{\omega c_I}{c_R^2 + c_I^2} = \frac{\omega}{2c_R Q},$$

we see that in order for both approaches to match, we need $Q \gg 1$ which implies $c_R^2 \gg c_I^2$ for the implementation to be well behaved. To conclude this section, we note that if in

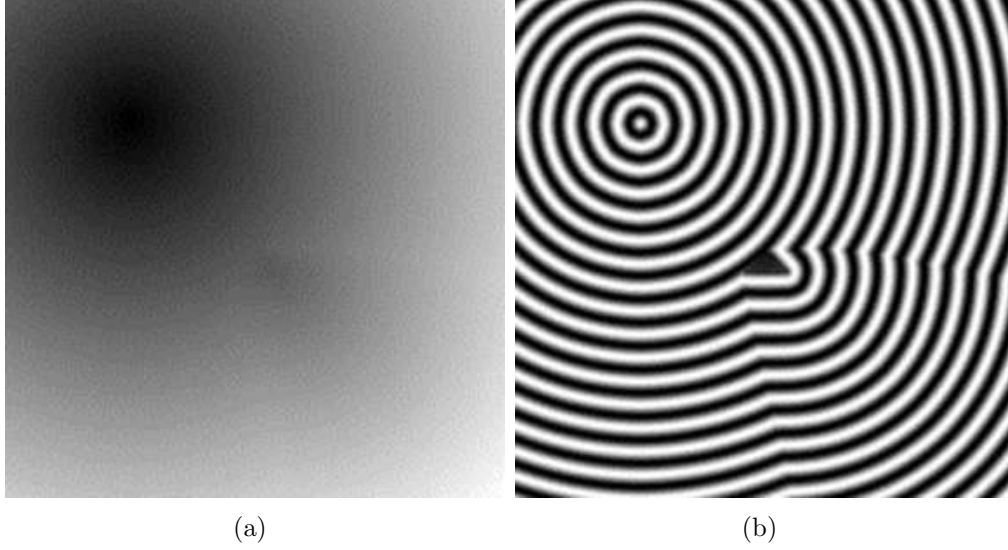


Figure 2.2: Eikonals Travel Times. Shown is the result of a finite difference modeling of the Eikonal equation of a constant background medium with an embedded high sound speed triangle. (a) Eikonals travel times. (b) Contour plots of constant Eikonals.

our development, a plane wave with oscillatory part $\exp[-i\mathbf{k} \cdot \mathbf{r}]$ was used, then we would require $c_I > 0$. This is discussed further in section 2.2.1 and appendix A.3.

2.2.3 High Frequency Ray Approximation

The imaging method of travel time tomography utilizes a high frequency approximation to the acoustic wave equation. Consider the acoustic wave equation in the frequency domain with a position dependent wave number $k(\mathbf{r})$

$$(\nabla^2 + k(\mathbf{r})^2) u(\mathbf{r}, \omega) = 0. \quad (2.25)$$

Define $\tau(\mathbf{r})$, the eikonal, to be a scalar function that represents how the phase of the wave changes with position. Consider the solution to be a plane of the form

$$u(\mathbf{r}, \omega) = \exp[i\omega(\tau(\mathbf{r}) - t)]. \quad (2.26)$$

Substituting equation 2.26 into 2.25 and noting that the sound speed $c(\mathbf{r})^2 = \omega^2/k(\mathbf{r})^2$

$$\frac{i\nabla^2\tau(\mathbf{r})}{\omega} - \nabla\tau(\mathbf{r})^2 + \frac{1}{c(\mathbf{r})^2} = 0.$$

In the limit of infinite frequency, we are left with the Eikonal equation

$$\nabla\tau(\mathbf{r})^2 = \frac{1}{c(\mathbf{r})^2}. \quad (2.27)$$

We use the package FDTIMES [85] to solve equation 2.27 by finite difference methods. The program outputs the eikonal which is the amount of time it takes for a wave to travel from source to grid points. The output travel times and an associated contour map (i.e. *cos* of the travel times) can be seen in Figure 2.2 for a model consisting of a high velocity triangle embedded in a constant sound speed medium.

CHAPTER 3: Numerical Forward Modeling

As developed in chapter 2, we made some physical assumptions on the propagation of acoustic waves in the human breast and derived the acoustic wave equation. Because of the high computation cost of time domain modeling, the efficiency of the frequency domain approach for a multi-source problem, and the ability to naturally incorporate higher wavelength features as we progress from lower to higher frequencies [2], we transformed the acoustic wave equation to the frequency domain, and we model the propagation of ultrasound within the breast using the Helmholtz equation

$$\left(\nabla^2 + \frac{\omega^2}{c(\mathbf{r})^2} \right) u(\mathbf{r}, \omega) = s(\mathbf{r}, \omega). \quad (3.1)$$

Previously, we stated the analytical solution of the Helmholtz equation. However, we must solve it numerically in order to use the solution in an numerical optimization problem. Methods exist to solve the integral equation given in equation 2.2.1. For example, [68] gives a method to solve an integral representation of the Helmholtz equation for application in ultrasound tomography breast imaging. In contrast to an integral representation, we numerically solve the Helmholtz equation by using a finite difference method. In this chapter we will discretize our problem and use the resulting discretized system to produce numerical field values that will be compared to real data whose acquisition is discussed in chapter 4. We will compare the finite difference numerical solution of the Helmholtz equation with the analytical solution.

In our problem, we are interested in the field values $u(\mathbf{r}, \omega)$ created as a result of acoustic radiation emanating from a total of γ sources at positions \mathbf{r}_γ along the ring transducer Γ . In our problem, we consider s to be a point source at positions \mathbf{r}_γ . It can then be expressed as $s(\mathbf{r}, \omega) = s(\omega)\delta(\mathbf{r} - \mathbf{r}_\gamma)$, where δ denotes the delta distribution. Note that the source locations \mathbf{r}_γ also serve as receiver locations for the sampling of the wave field u along

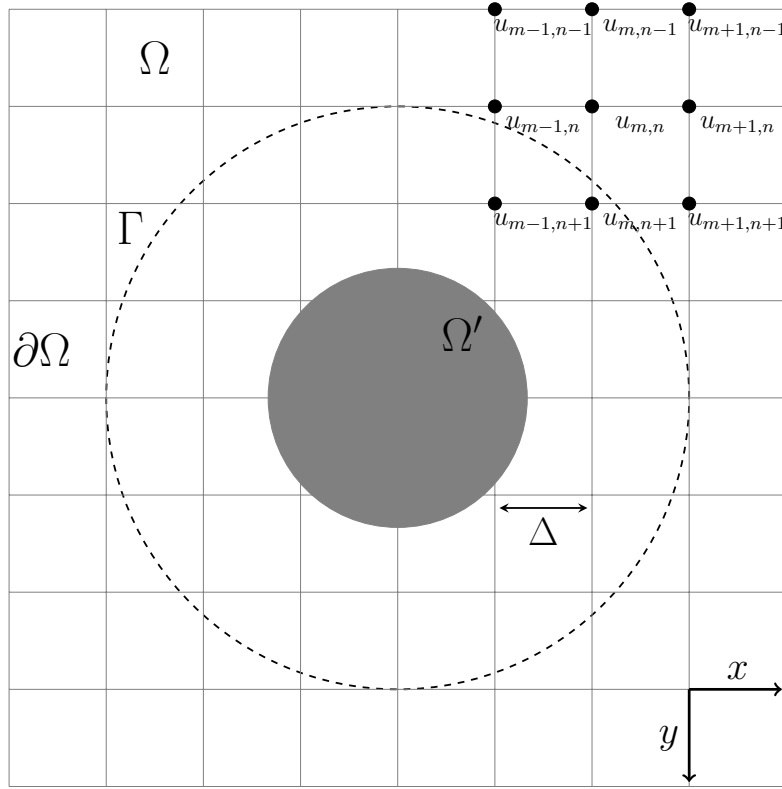


Figure 3.1: Discretized Acquisition Geometry. The domain Ω is split into an evenly spaced grid with spacing Δ . The boundary of Ω is $\partial\Omega$. A transducer ring Γ surrounds the object Ω' that will be imaged. Cartesian coordinates are sampled on the corner points $u_{m,n}$. Direction of positive and negative x and y coordinates are given in lower right hand corner of stencil.

the ring transducer. Also, both the field values u and the sources s are complex valued quantities as they represent the amplitude and phase of the propagating waves and source wavelet, respectively.

3.1 Discretization

In order to use computer programs to numerically solve the above differential equation, we set bounds for the problem by considering only solutions in a square domain $\Omega = [-L/2, L/2] \times [-L/2, L/2]$, where L is big enough to allow the placement of a ring array transducer ring with radius R . The boundary of the domain is denoted $\partial\Omega$. We discretize Ω into a $N \times N$ square grid mesh with uniformly sized cell indices with physical dimensions $\Delta = L/N$. The number of pixels N^2 in the mesh is chosen such that the physical dimension of each pixel is $\Delta = \lambda/n_\lambda$, where λ is the wavelength of the chosen optimization

frequency, and $n_\lambda = 5$ is the number of grid points per wavelength chosen to balance the computation cost, the quality of the reconstructed image, and the mitigation of numerical dispersion. Due to numerical dispersion, choosing $n_\lambda \leq 4$ leads to a complete breakdown of the algorithm. Choosing a value $n_\lambda > 5$ increases the computation time without providing a substantial increase in the quality of the reconstructed image. To compute the wavelength, we use the mean sound speed of the water bath surrounding the breast as a reference value. The discretized acquisition geometry is seen in Figure 3.1. In the new discretized system, the coordinate vector \mathbf{r} becomes $\mathbf{r}_{m,n}$ where

$$\mathbf{r}_{m,n} = (x_m, y_n), \quad x_m = -L/2 + m\Delta, \quad y_n = -L/2 + n\Delta, \quad m, n \in [0, N - 1].$$

The field values $u(\mathbf{r})$ and source function $s(\mathbf{r})$ would then become $u(\mathbf{r}_{m,n})$ and $s(\mathbf{r}_{m,n})$, respectively. For interior points, i.e. $\mathbf{r}_{m,n} \in \Omega$, the Helmholtz operator is discretized using an optimal nine-point finite difference stencils detailed in [86]. The discretized representation of equation 3.1 for the field value $u(\mathbf{r}_{m,n})$ is then given by

$$\begin{aligned} & \left(\nabla^2 + \frac{\omega^2}{c(\mathbf{r}_{m,n})^2} \right) u(\mathbf{r}_{m,n}, \omega) \approx \alpha_1 \frac{u_{m+1,n} + u_{m-1,n+1} - u_{m,n} + u_{m,n+1} + u_{m,n-1}}{\Delta^2} \\ & + (1 - \alpha_1) \frac{u_{m+1,n+1} + u_{m+1,n-1} + u_{m-1,n+1} + u_{m-1,n-1}}{(\sqrt{2}\Delta)^2} \\ & + \frac{\omega^2}{c_{m,n}^2} \left[\alpha_2 + \alpha_3 (u_{m,n} + u_{m-1,n} + u_{m,n+1} + u_{m,n-1}) \right. \\ & \left. + \frac{1 - \alpha_2 - 4\alpha_3}{4} (u_{m+1,n} + u_{m+1,n-1} + u_{m-1,n+1} + u_{m-1,n-1}) \right] = -\delta_{m,n}(\omega), \quad \mathbf{r}_{m,n} \in \Omega. \end{aligned}$$

where the coefficients α_i are determined by minimizing numerical dispersion. The right hand side forcing term $\delta_{m,n}(\omega)$ is the Fourier transform of the source signal $\delta(\mathbf{r}', \omega)$ and is non-zero only when the indices m, n correspond to points on the transducer ring Γ . For $\mathbf{r}_{i,j} \in \partial\Omega$, absorbing boundary conditions are used to dissipate waves on the major faces [87] and the corner points of the boundary [88, 89]. This plays the role of the Sommerfeld radiation condition when deriving the analytical solution in section 2.2.1. The boundary

conditions are such that they do not allow reflection but only outward traveling waves on the boundaries. This is true for waves normally incident on the boundary. However, the efficacy of the absorbing boundary conditions to inhibit the introduction of reflected energy back in to the system becomes progressively worse as waves arrive at more oblique incidence. An example of the absorbing boundary condition on the left face of $\partial\Omega$ is given by

$$\left(\frac{i\omega}{c(\mathbf{r}_{m,n})} \frac{\partial}{\partial x} + \frac{\omega^2}{c(\mathbf{r}_{m,n})^2} + \frac{1}{2} \frac{\partial^2}{\partial y^2} \right) u(\mathbf{r}_{m,n}, \omega) \approx \frac{i\omega}{c_{m,n}} \frac{u_{m+1, -} - u_{m,n}}{\Delta} \\ + \frac{\omega^2}{c_{m,n}^2} u_{m,n} + \frac{1}{2} \frac{u_{m,n+1} - 2u_{m,n} + u_{m,n-1}}{\Delta^2} = 0, \quad \mathbf{r}_{m,n} \in \partial\Omega.$$

For the Top-Left corner point, the boundary condition is given by

$$\left(\frac{\partial}{\partial x} + \frac{\partial}{\partial y} + \frac{3}{2} \frac{i\omega}{c(\mathbf{r}_{m,n})} \right) u(\mathbf{r}_{m,n}, \omega) \approx \frac{u_{m+1,n} - u_{m,n}}{\Delta} \\ + \frac{u_{m,n+1} - u_{m,n}}{\Delta} + \frac{i\omega}{c_{m,n}} u_{m,n} = 0, \quad \mathbf{r}_{m,n} \in \partial\Omega.$$

Further discussion and details of the finite difference stencils are available in Appendix A.

3.2 Matrix Solution

We can now consider every other unknown field value $u(\mathbf{r}_{m,n})$ and stack them into an N^2 dimensional vector \mathbf{u} . Similarly, we define the N^2 dimensional vector \mathbf{s} that has non-zero values only at the grid indices $\mathbf{r}_{m,n}$ that correspond to the position of the transmitting transducer element. The discretized Helmholtz operator is stored in a matrix \mathbf{S} with dimensions $N^2 \times N^2$. The matrix \mathbf{S} is large but very sparse. There are about 9 non-zero values for every N^2 grid points. It is pseudodiagonal because it has nine diagonal bands of non-zero entries corresponding to the coefficients of the nine-point stencil. Its entries depend on the assumed sound speed model and the chosen absorbing boundary conditions. With the above discretization, the Helmholtz equation can be written in matrix form as

$$\mathbf{S}\mathbf{u} = \mathbf{s}, \quad \mathbf{u}, \mathbf{s} \in \mathbb{C}^{N^2}, \quad \mathbf{S} \in \mathbb{C}^{N^2 \times N^2}. \quad (3.2)$$

See Appendix A.8 for an explicit example of the structure of \mathbf{S} . Note that the above equation

needs to be solved for γ sources. Since the matrix \mathbf{S} does not change unless the sound speed model is updated, these systems of equations can be efficiently solved using LU factorization [90, 91]. Once \mathbf{S} has been factored, its LU constituents can be re-used to rapidly solve the system of equations corresponding to each source. This is one reason why the frequency domain waveform tomography method is preferred to the time domain method. We note that the solution \mathbf{u} of equation 3.2 depends on the source vector \mathbf{s} for which we can make an arbitrary initial guess. The guess is scaled by a complex scalar using a method to estimate the source signal (see section 5.2.7). The field values \mathbf{u} are also scaled by the same factor.

3.3 Discussion

3.3.1 Attenuation: Relationship Between Q and Power Loss

From section 2.2.2, we came to the conclusion that we can simulate attenuation by allowing the sound speed to be complex valued. Neglecting geometrical decay ($1/\sqrt{x}$), the amplitude of the wave $A(x)$ at a position x is then given by

$$A(x) = \exp[-\alpha_Q x] = \exp\left[\frac{-\omega x}{2c_R Q}\right], \quad c_I = -\frac{c_R}{2Q}.$$

However, ultrasound attenuation is usually given in terms of power loss. For example, the units of the attenuation coefficient can be $[\alpha] = [\text{dB}/(\text{mm Mhz})]$. In this section we will see how changing the quality factor Q affects the power of the numerically generated wave fields. We define the power loss ΔdB at a pixel location $\mathbf{r}_{m,n}$, for a particular frequency ω and quality factor Q to be

$$\Delta\text{dB} = 20 \log_{10} \left(\frac{u(\mathbf{r}_{m,n}, \omega, Q)}{u(\mathbf{r}_{m,n}, \omega, Q = \infty)} \right),$$

where there is no attenuation when $Q = \infty$ ($c_I = 0$). In this experiment, we use a constant sound speed model of $c = 1500$ m/s, frequencies ranging between 112 and 336 kHz, and Q values between 200 and 20. Using a single transducer to excite the medium, the average power loss per unit length $\overline{\Delta\text{dB}/\bar{x}}$ averaged over all receiver location is given by

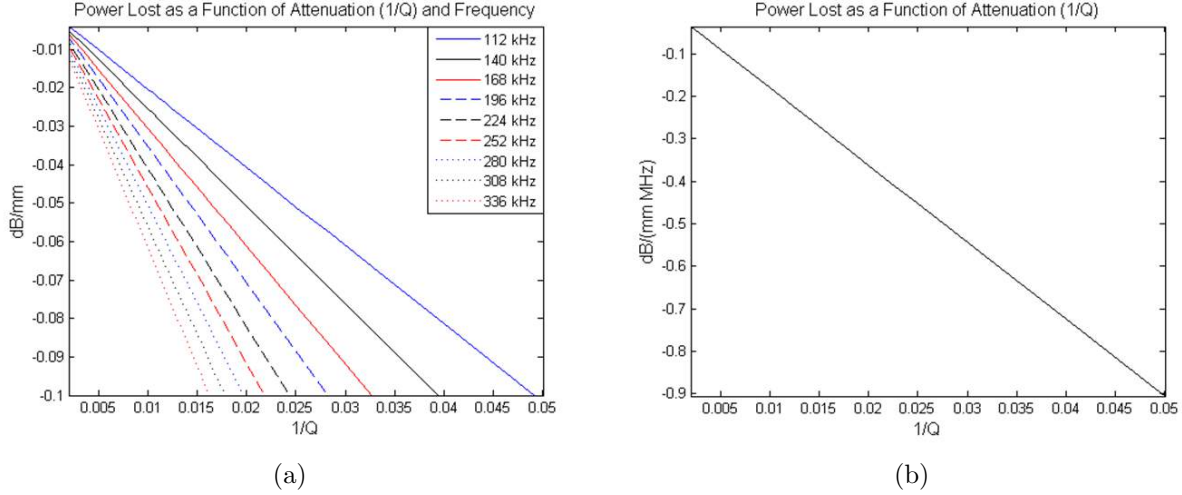


Figure 3.2: Average Power Lost as a Function of Q and Frequency. (a) Power lost per unit distance. (b) Power lost per unit distance. Use the frequency f and not ω when using this figure.

$$\frac{\Delta \overline{\text{dB}}}{\bar{x}} = \frac{1}{\bar{x}} \sum_{\mathbf{r}_{m,n} \in \Gamma} 20 \log_{10} \left(\frac{u(\mathbf{r}_{m,n}, \omega, Q)}{u(\mathbf{r}_{m,n}, \omega, Q = \infty)} \right), \quad (3.3)$$

where \bar{x} is the average propagation distance from the source transducer to receiver transducers. A plot of the expression in equation 3.3 versus $1/Q$ is seen in Figure 3.2(a). By dividing by the frequency ω , we can generate a plot of the average power loss per unit length and frequency as see in Figure 3.2(b). From Figures 3.2(a) and 3.2(b), it can be deduced that the power loss is given by

$$\Delta \overline{\text{dB}} = \frac{20}{\ln 10} \frac{\omega \bar{x}}{2c_R Q}. \quad (3.4)$$

Thus using equation 3.4, we have a simple formula to convert between Q and the average power loss $\Delta \overline{\text{dB}}$.

3.3.2 Reflections From Boundary

The reader may be concerned that a small distance between the transducer ring and the artificial boundary $\partial\Omega$ would cause reflections that would corrupt the sampling of the wave fields u on the transducer ring. This might be further exacerbated by the intuition in the time domain where having a larger Region of Interest (ROI) would allow the omission of

reflected waves by choosing an appropriate time t_{max} to stop sampling the wave field at the transducer location. However in the frequency domain, solutions are essentially integrated over infinite time, and the effects of reflection from artificial boundaries in numerical simulations can be mitigated by appropriate absorbing boundary conditions. This is in contrast to section 2.2.1 where a combination of Dirichlet/Neumann boundary conditions and the Sommerfeld radiation condition gave rise to a unique and physically acceptable solution to the wave equation. A totally reflecting boundary condition, i. e. $u(\mathbf{r}_{m,n}) = 0$, $\mathbf{r}_{m,n} \in \partial\Omega$ would lead to the generation of standing waves for the field values u within the domain Ω . This does not model acoustic wave propagation within the breast and our ultrasound tomography prototypes. Instead, we must use absorbing boundary conditions. In our experience, a 2nd order Engquist and Majda absorbing boundary condition [87] (see section A.3) was quite sufficient at damping waves on the artificial boundary.

3.3.3 Comparison of Analytical Solution and Numerical Approximation

In this section we will compare the numerical reconstruction representing the field values $u(\mathbf{r}, \omega)$ to the analytical solution. It is useful to explore the asymptotic expansion of the 2D Helmholtz Green's function. Combining the Green's function for the 2D Helmholtz equation (i.e. equation 2.19) and the asymptotic expansion ($z = \omega|\mathbf{r} - \mathbf{r}'|/c \rightarrow \infty$) of the Hankel function (see [92]) gives

$$\frac{i}{4}H_0^{(1)}(z) \simeq \frac{i}{4}\sqrt{\frac{2}{\pi z}} \exp\left[i\left(z - \frac{\pi}{4}\right)\right] = \frac{1}{\sqrt{8\pi z}} \exp\left[i\left(z + \frac{\pi}{4}\right)\right].$$

From the asymptotic expansion we see that the field values behave as plane waves $\exp[iz]$ that decay as $1/\sqrt{z}$. This contrasts to the 3D case where the decay behaves as $1/|\mathbf{r} - \mathbf{r}'|$. We will compare the analytical solution $i/4 H_0^{(1)}(z)$ to a numerical simulation. In this comparison we set the sound speed model to a constant value of $c = 1500$ m/s, the frequency to $f = 100$ kHz with $\omega = 2\pi f$, and the source function $s = -1.0/\Delta^2$ at position $\mathbf{r}_0 = (0.11, 0)$ (meters). The real $\text{Re}\{\mathbf{u}\}$ and imaginary $\text{Im}\{\mathbf{u}\}$ numerical wave field values as well as their modulus and phase are shown in Figure 3.3.

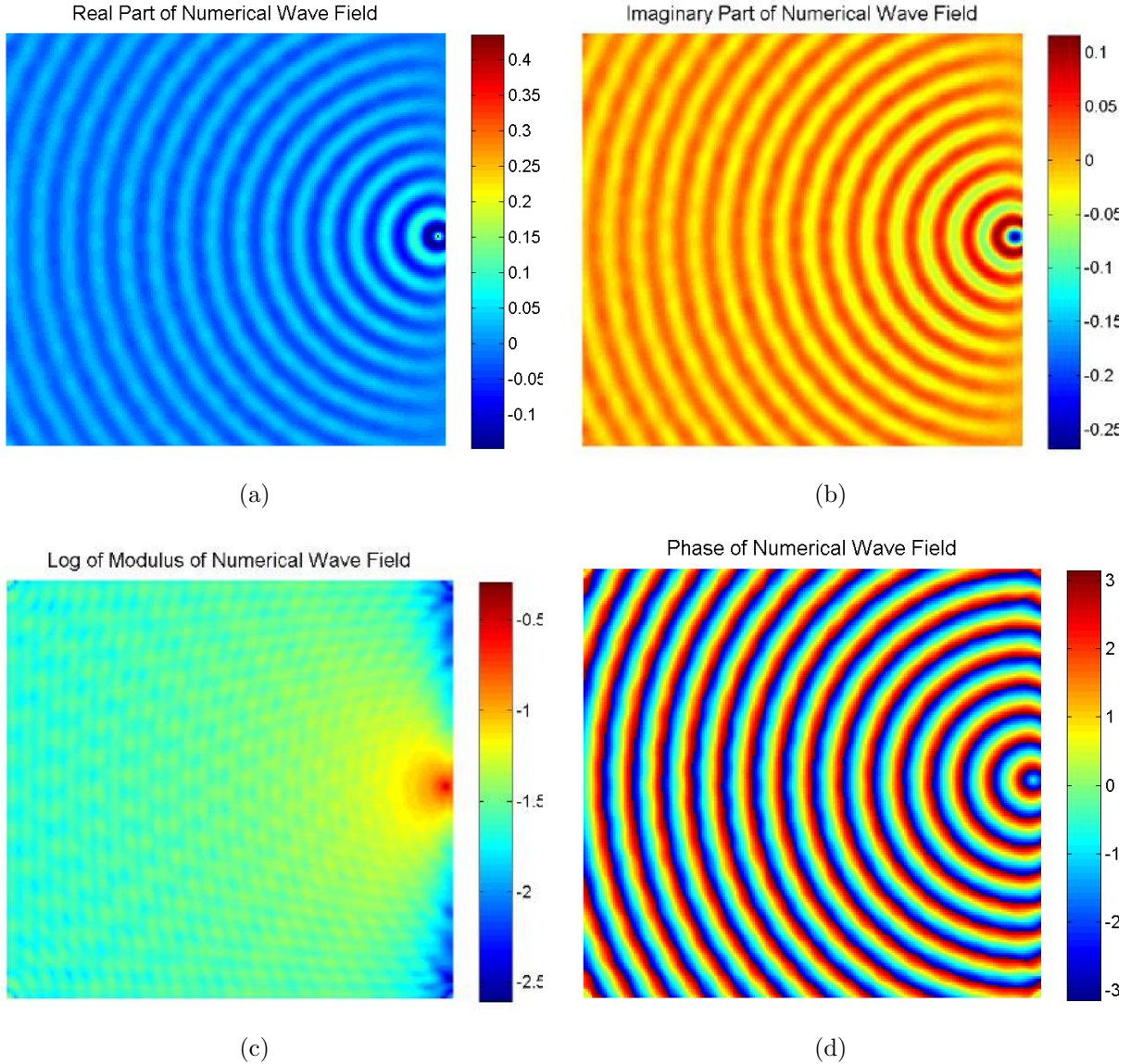


Figure 3.3: Numerical Wave Fields. (a) Real part of numerical wave field $\text{Re}\{\mathbf{u}\}$. (b) Imaginary part of numerical wave field $\text{Im}\{\mathbf{u}\}$. (c) Log of the modulus of the numerical wave field $\log_{10} [|\mathbf{u}|]$. (d) Phase of the numerical wave field $\tan^{-1} [\text{Im}\{\mathbf{u}\}/\text{Re}\{\mathbf{u}\}]$.

Horizontal line profiles of the real and imaginary field values in Figures 3.3(a) and 3.3(b) are compared to the Green's function of the 2D Helmholtz equation in Figure 3.4. We see that the numerical and analytical solutions agree very well up to amplitude normalization. Next, we again compare the numerical and analytical solutions, but with attenuation added via a complex sound speed (see sections 2.2.2 and 3.3.1). Using the same parameters in the previous comparison in Figure 3.4 but with a quality factor of $Q = 50$ ($c = 1500 - i1500/(2 \cdot 50)$), the numerical and analytical solutions with attenuation are shown in Figure 3.5. We

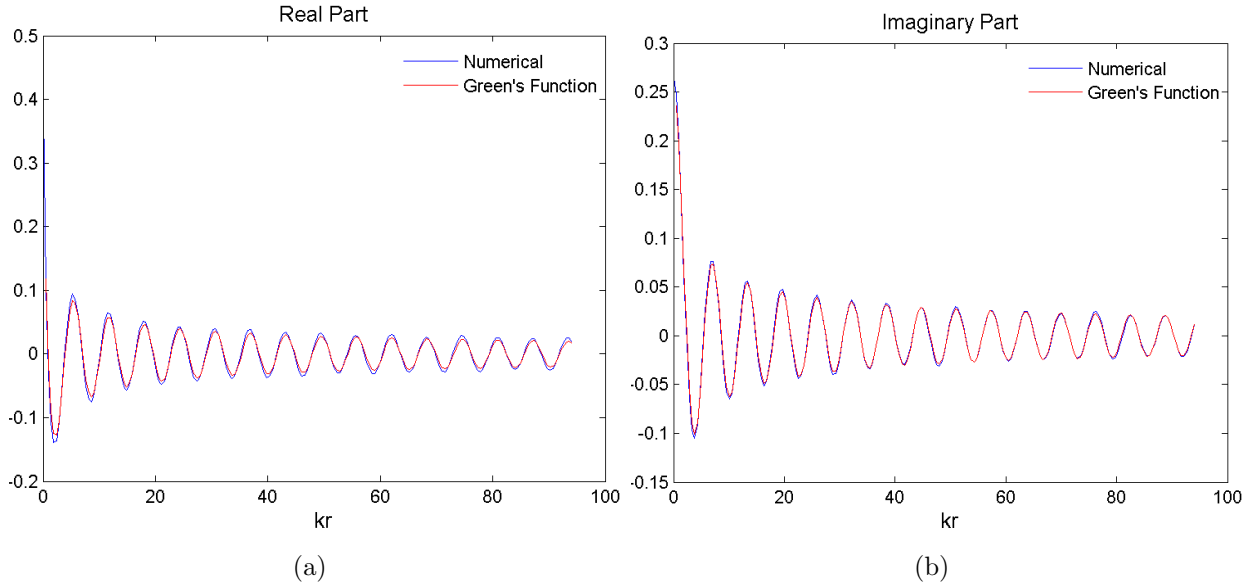


Figure 3.4: Comparison of Numerical and Analytical Solutions. (a) Line profile of real part of numerical wave field $\text{Re}\{\mathbf{u}\}$ and real part of Green's function. (b) Line profile of imaginary part of numerical wave field $\text{Re}\{\mathbf{u}\}$ and imaginary part of Green's function. Graphs are plotted as a function of $kr = k|\mathbf{r} - \mathbf{r}'|$.

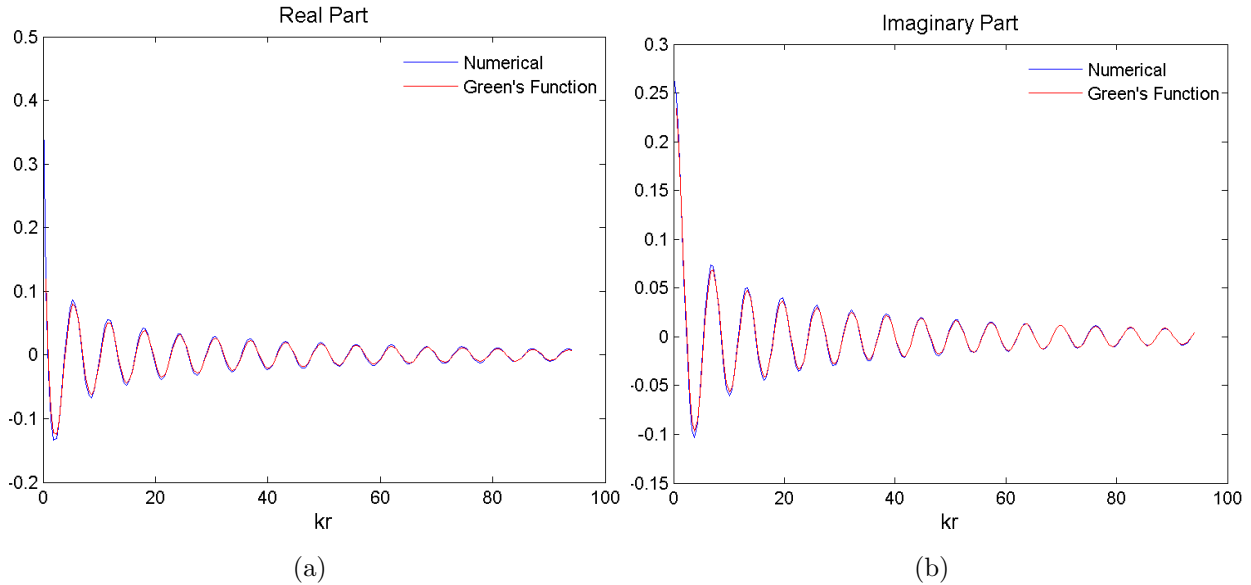


Figure 3.5: Comparison of Numerical and Analytical Solutions With Attenuation. (a) Line profile of real part of numerical wave field $\text{Re}\{\mathbf{u}\}$ and real part of Green's function. (b) Line profile of imaginary part of numerical wave field $\text{Re}\{\mathbf{u}\}$ and imaginary part of Green's function. Graphs are plotted as a function of $kr = k|\mathbf{r} - \mathbf{r}'|$.

see that numerical results, with and without attenuation, agree very well with the theoretical prediction.

CHAPTER 4: Inverse Problem

In this chapter we will discuss the inverse problem and the steps that need to be taken to solve it. We will define the cost function and discuss how it will be minimized using gradient descent methods. This will give an iterative procedure to update the sound speed model. We will then give an explicit formulation of the gradient of the cost function which will be used to update the sound speed model. We will conclude the chapter with numerical reconstructions and experiments which analyze the accuracy and resolution of our method. The reader is referred to [93, 94] for excellent resources on the detailed discussion of the inverse problem.

4.1 Cost Function

Recalling from section 1.6, we would like to estimate a sound speed model \mathbf{c} that generates, upon numerical simulation, simulated measurements $\mathbf{u}_{obs}(\omega, \mathbf{c})$ that best match the experimental measurements $\mathbf{d}_{obs}(\omega)$ (the data acquisition procedure and signal processing leading to $\mathbf{d}_{obs}(\omega)$ will be discussed in Chapter 5). More specifically, we would like to minimize the real valued mean squared error cost function

$$E(\omega, \mathbf{c}) = \frac{1}{2} \mathbf{e}^H(\omega, \mathbf{c}) \mathbf{e}(\omega, \mathbf{c}), \quad (4.1)$$

where H denotes the Hermitian transpose, and \mathbf{e} is the residual mismatch defined as

$$\mathbf{e}(\omega, \mathbf{c}) = \mathbf{u}_{obs}(\omega, \mathbf{c}) - \mathbf{d}_{obs}(\omega).$$

The vectors \mathbf{u}_{obs} and \mathbf{d}_{obs} represent the numerical and experimental wave fields sampled on the transducer aperture Γ for every receiver. Since there are N_T^2 emitter-receiver pairs, $\mathbf{u}_{obs}, \mathbf{d}_{obs} \in \mathbb{C}^{N_T^2}$. In addition, since we discretize our domain Ω in a mesh of size N^2 , the sound speed model $\mathbf{c} \in \mathbb{C}^{N^2}$. If additional *a priori* information is known about the

relationship between the vectors \mathbf{u}_{obs} and \mathbf{d}_{obs} , a data covariance matrix \mathbf{C}_d that contains this information can be incorporated into equation 4.1. If we wish to constrain and smooth the reconstruction process, a regularization term can be incorporated by the use of the Lagrange multiplier λ_R and the regularization operator \mathcal{R} acting on the model space \mathbf{c} . The Lagrange multiplier λ_R balances the contribution of the the original penalty term in equation 4.1 and the regularization term. The cost function with additional *a priori* knowledge and regularization is given by

$$E(\omega, \mathbf{c}) = \frac{1}{2} \mathbf{e}^H(\omega, \mathbf{c}) \mathbf{C}_d^{-1} \mathbf{e}(\omega, \mathbf{c}) + \lambda_R \mathcal{R}(\mathbf{c}).$$

Common regularization operator include the Tikhonov and the Total Variation operators[46, 95]. All of the sound speed reconstructions in this thesis do not use a regularization term except for some of the attenuation reconstructions in section 4.4.2 which use Tikhonov regularization with $\mathcal{R}(\mathbf{c}) = |\Delta \mathbf{c}_I|^2$ which penalizes perturbations $\Delta \mathbf{c}_I$ to the current imaginary sound speed model. Choosing larger and smaller values of λ_R controls the degree to which the update is penalized.

4.2 Linearization of the Cost Function

In this section we linearize the cost function to arrive at an update equation for the sound speed \mathbf{c} . Expanding the cost function E from equation 4.1, but omitting the explicit dependence on ω , and using the notation $\mathbf{u}(\mathbf{c}) = \mathbf{u}_{obs}(\mathbf{c})$ and $\mathbf{d} = \mathbf{d}_{obs}$, we have

$$E(\mathbf{c}) = \frac{1}{2} (\mathbf{u}(\mathbf{c}) - \mathbf{d})^H (\mathbf{u}(\mathbf{c}) - \mathbf{d}).$$

We seek to find the optimum model $\mathbf{c}_{opt} = \underset{\mathbf{c}}{\operatorname{argmin}} E(\mathbf{c})$ by locally optimizing the cost function E about a neighborhood \mathbf{c}_0 . In order to arrive at the optimum solution, we use an iterative procedure where we assume the updated model is given by the previous model with an added perturbation $\Delta \mathbf{c}$

$$\mathbf{c} = \mathbf{c}_0 + \Delta \mathbf{c}.$$

Taylor expanding the cost function E at the updated model location gives

$$E(\mathbf{c}) = E(\mathbf{c}_0 + \Delta\mathbf{c}) = E(\mathbf{c}_0) + \frac{\partial E(\mathbf{c}_0)}{\partial \mathbf{c}} \Delta\mathbf{c} + \frac{1}{2} \frac{\partial^2 E(\mathbf{c}_0)}{\partial \mathbf{c}^2} (\Delta\mathbf{c})^2 + \mathcal{O}\left(\frac{\partial^3}{\partial \mathbf{c}^3}\right). \quad (4.2)$$

Since we are interested in the minimum of the cost function E , we take the derivative of equation 4.2 with respect to \mathbf{c} and set it equal to zero to give

$$0 = \frac{\partial E(\mathbf{c})}{\partial \mathbf{c}} = \frac{\partial E(\mathbf{c}_0)}{\partial \mathbf{c}} + \frac{\partial^2 E(\mathbf{c}_0)}{\partial \mathbf{c}^2} \Delta\mathbf{c}.$$

Which mean that the perturbation $\Delta\mathbf{c}$ is given by

$$\Delta\mathbf{c} = - \left[\frac{\partial^2 E(\mathbf{c}_0)}{\partial \mathbf{c}^2} \right]^{-1} \frac{\partial E(\mathbf{c}_0)}{\partial \mathbf{c}}.$$

The second derivative term is called the Hessian. Explicitly calculating the Hessian results in Newton's method, while a typical approximation to it gives the Gauss-Newton Method.

We can also set the value equal to a positive scalar α giving the Gradient Descent Method.

With this choice, we arrive at the update equation for every iteration i

$$\mathbf{c}^{(i+1)} = \mathbf{c}^{(i)} + \Delta\mathbf{c} = \mathbf{c}^{(i)} - \alpha \frac{\partial E(\mathbf{c}_0)}{\partial \mathbf{c}}.$$

4.3 Gradient Descent Method

To solve the inverse problem for sound speed reconstruction, we use an iterative approach. The starting sound speed model $\mathbf{c}^{(0)}$ is created using a travel time reconstruction method [3]. For each frequency ω , we define a stopping criterion by updating the sound speed a configurable number of times. This is based on balancing computation cost with the quality of the reconstructed image. The quality of the image is a subjective metric which balances the interpretation of the apparent ability of the algorithm to correctly image structures and the introduction of noise and artifacts into the reconstructed image. Often times, the quality can be improved by taking more iterations at a particular frequency or by incorporating higher frequency information. However, there is a point where the improvements in quality

by making further iterations or moving to higher frequencies are negligible when compared to the additional computation cost. An optimal frequency and iteration schedule is a topic of current and ongoing investigation. In the inversion process, we start at the lowest frequency in the set of selected frequencies, and then we move to the next frequency until all frequencies have been used. Given a current estimate $\mathbf{c}^{(i)}$ of the sound speed model, we find the gradient of the cost function at that point. We then update the sound speed in the direction of the steepest descent to obtain a new estimate $\mathbf{c}^{(i+1)}$. The sound speed update can be written as

$$\mathbf{c}^{(i+1)} = \mathbf{c}^{(i)} - \alpha^{(i)} \nabla E(\omega, \mathbf{c}^{(i)}),$$

where α is the step size as determined by a line search method [96], and the gradient $\nabla = \partial/\partial c_R$ or $\partial/\partial c_I$ depending on if the real part c_R or the imaginary part c_I of the sound speed is to be updated. A simple example of the gradient descent method for a toy problem is given in Appendix B.3. When using the line search method in a gradient descent algorithm, one chooses an initial step size α_0 . This choice can be made, for example, based on experience working with the numerical algorithm. The algorithm decides if the step size was appropriate if the cost function decreases sufficiently. An appropriate decrease is dictated by the Wolfe conditions. We only enforce the first condition called the Armijo rule in equation 4.3)

$$E(\mathbf{c}^{(i)} - \alpha^{(i)} \nabla E(\omega, \mathbf{c}^{(i)})) \leq E(\mathbf{c}^{(i)}) - c_1 \alpha^{(i)} \nabla E(\mathbf{c}^{(i)})^H E(\mathbf{c}^{(i)}), \quad (4.3)$$

where c_1 is a positive constant. If the the step size was successful, then we can increase it, for example $\alpha \rightarrow 2\alpha$, for the subsequent iteration. If the cost function did not decrease or did not satisfy the Armijo rule because the algorithm overshot the appropriate location, then we can decrease the step size, for example $\alpha \rightarrow \alpha/2$, and try again. An alternative to the line search method involves finding an optimal step length α which can be chosen by minimizing the cost function E with respect to α (see Appendix B.1). The inversion process can also be improved in terms of computation speed using a conjugate gradient method [97].

4.3.1 Starting Model and Phase Mismatch

In order to ensure that the waveform tomography algorithm converges to a solution close to the global minimum, an accurate starting sound speed model is needed to avoid cycle skipping phase mismatch between the simulated measurement \mathbf{u}_{obs} and the experimental measurements \mathbf{d}_{obs} [98]. For example, let the true phase of a discrete frequency component of the received waveform be $\phi_d = 0$. If an initial sound speed model \mathbf{c}_1 predicts a phase ϕ_1 such that $-\pi < \phi_1 \leq \pi$, then the algorithm will update the sound speed model to \mathbf{c}'_1 in order to minimize the phase mismatch: $\phi_1 \rightarrow \phi_d$. However, if another initial sound speed model \mathbf{c}_2 predicts a phase ϕ_d such that $-3\pi < \phi_2 \leq -\pi$, then the algorithm will update the sound speed model to the wrong local minimum \mathbf{c}'_2 to minimize the phase mismatch: $\phi_2 \rightarrow \phi_d - 2\pi$. We generate our starting model using the travel time tomography method detailed in [3]. The travel time reconstruction algorithm is iterated sufficiently to output a high enough resolution image that avoids phase mismatch due to cycle skipping. However, overiteration is avoided as it introduces strong ray artifacts which are retained throughout the waveform tomography inversion process. Paralleling the need for an accurate starting model, once the inversion process begins, each subsequent update of the sound speed needs to adequately avoid the cycle skipping problem in order to converge in the direction of the global minimum. This requirement becomes stricter as higher frequencies are incorporated into the inversion process.

4.3.2 Calculating the Gradient

From the Appendix B.2, the gradient evaluates as

$$\nabla E = Re \{ \mathbf{J}^H \mathbf{e} \} ,$$

where \mathbf{J} is a $N_T^2 \times N^2$ Fréchet derivative matrix whose elements are given by

$$J_{i,j} = \frac{\partial u_{obs,i}}{\partial c_j} , \quad i = 1, 2, \dots, N_T^2, \quad j = 1, 2, \dots, N^2 , \quad (4.4)$$

where $u_{obs,i}$ and c_j are the i -th and j -th elements of the vectors \mathbf{u}_{obs} and \mathbf{c} , respectively.

We again emphasize that we can take the derivative with respect to the real or imaginary part of the sound speed to update the corresponding parameter of interest. We will not calculate these derivatives explicitly, but we use the approach of [56] and take the derivative of equation 3.2 with respect to the sound speed at each grid point to obtain an expression for the gradient. This yields

$$\frac{\partial \mathbf{u}}{\partial c_j} = -\mathbf{S}^{-1} \frac{\partial \mathbf{S}}{\partial c_j} \mathbf{u} = \mathbf{S}^{-1} \mathbf{f}_j, \quad (4.5)$$

where the inverse operator $(\cdot)^{-1}$ is shorthand for the LU decomposition and inversion process, and $\mathbf{f}_j = (-\partial \mathbf{S} / \partial c_j) \mathbf{u}$ is the “virtual source.” In order to calculate $\partial \mathbf{S} / \partial c_j$, we use the derivatives of the finite difference equations in [86]. Note that equation 4.4 involves the field values \mathbf{u}_{obs} at the transducer grid points, and equation 4.5 involves the field values \mathbf{u} at all grid points. We augment the expression in equation 4.4 to create an augmented Fréchet derivative matrix $\hat{\mathbf{J}}$ of dimensions $N^2 \times N^2$ with coefficients

$$\hat{J}_{i,j} = \frac{\partial u_i}{\partial c_j}, \quad i, j = 1, 2, \dots, N^2,$$

where u_i is the i -th element of the vector \mathbf{u} . Likewise, we augment the residual vector \mathbf{e} with zeros to create an N^2 dimensional vector $\hat{\mathbf{e}}$. Considering each of the column vectors \mathbf{f}_j as a column of a matrix \mathbf{F} , the augmented Fréchet matrix can be written as

$$\hat{\mathbf{J}} = \mathbf{S}^{-1} [\mathbf{f}_1 \dots \mathbf{f}_{N^2}] = \mathbf{S}^{-1} \mathbf{F}.$$

The expression for the gradient in equation 4.3.2 reduces to

$$\nabla E = Re \left\{ \hat{\mathbf{J}}^H \hat{\mathbf{e}} \right\} = Re \left\{ \mathbf{F}^H [\mathbf{S}^{-1}]^H \hat{\mathbf{e}} \right\} = Re \left\{ \mathbf{F}^H \mathbf{v} \right\},$$

where $\mathbf{v} = [\mathbf{S}^{-1}]^H \hat{\mathbf{e}}$ is the back-propagated wave field with the residual acting as a source. Example of gradients are shown in Figure 4.1.

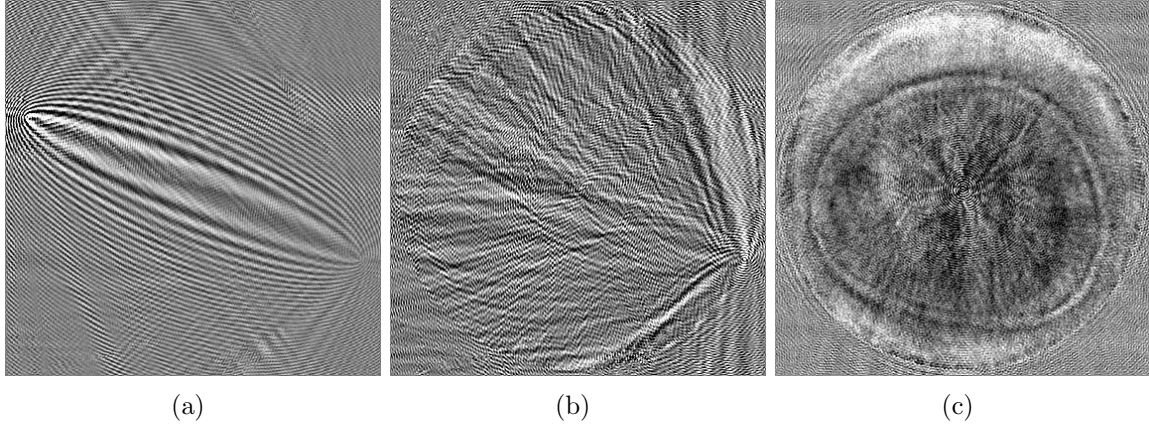


Figure 4.1: The Gradient of the Cost Function. (a) Gradient for one emitter and one receiver. (b) Accumulated gradient for one emitter and all receivers. (c) Accumulated gradient for all emitters and all receivers.

4.4 Numerical Reconstructions: Accuracy and Resolution Analysis

In this section, we will assess the accuracy and resolution of our waveform tomography algorithm. We will first compare the accuracy and resolution of travel time and waveform methods. We qualitatively inspect the reconstruction of a heterogeneous numerical phantom. We will also compare the edge response of a sound speed reconstruction of a homogeneous cylindrical phantom with and without attenuation. The convergence of the algorithm to the true solution will be seen in a plot of the cost function. For these waveform tomography reconstructions, in order to avoid the inverse crime, forward modeling is done using the same frequency domain algorithm but with different discretized parameters. The inverse crime refers to when identical or nearly identical algorithm parameters are used to forward model and invert data in the inverse problem. Next, we will use a time domain acoustic wave propagation algorithm [65] to simulate waveform data. We note that this method of preparing forwarded modeled data completely avoids any problems that might be associated with committing the inverse crime since the observed data is created using an entirely different method. We preprocess and transform the data (see section 5.2) and input it in to our frequency domain waveform tomography algorithm. We perform this experiment on a cylindrical model and a model where two small squares are separated by a fixed distance.

We assess the resolution capabilities of waveform tomography in this scenario by computing the edge response of the cylinder and by seeing how well the spacing between the squares is resolved.

4.4.1 Methods: Experiment 1

True Models

To analyze the resolution and accuracy of our waveform tomography algorithm, we numerically simulate wave propagation on known sound speed distributions which we refer to as “true models.” The goal is to see how well the inversion process reconstructs the true models. In this section, we simulated a heterogeneous sound speed model intended to simulate the sound speed and morphology of structures in the breast, and a cylindrical model consisting of a 50 mm radius 1540 m/s cylinder embedded in a 1470 m/s background that will be used to calculate an edge response. For attenuation reconstructions, we simulated a cylindrical model consisting of a 50 mm radius with $Q = 100$ embedded in a 1540 m/s background sound speed with no attenuation. The true models are seen in Figure 4.2.

Resolution and Accuracy

The resolution is defined by the distance of the edge response between the 10% and 90% values of the data relative to the minimum and maximum values of the reconstruction. The accuracy is measured by the absolute value of the average residual sound speed between the reconstructed image with respect to the true model where the sum is carried over all N_p pixels within a chosen region of interest (ROI) of the reconstructed image

$$accuracy = \left| \frac{1}{N_p} \sum_{i=1}^{N_p} [\mathbf{c}(i)_{true} - \mathbf{c}(i)] \right|, \quad (4.6)$$

where the true model is \mathbf{c}_{true} and the reconstructed image is \mathbf{c} . To see the manner in which the waveform reconstruction converges to the true model as a function of iteration number, we can consider the behavior of the cost function.

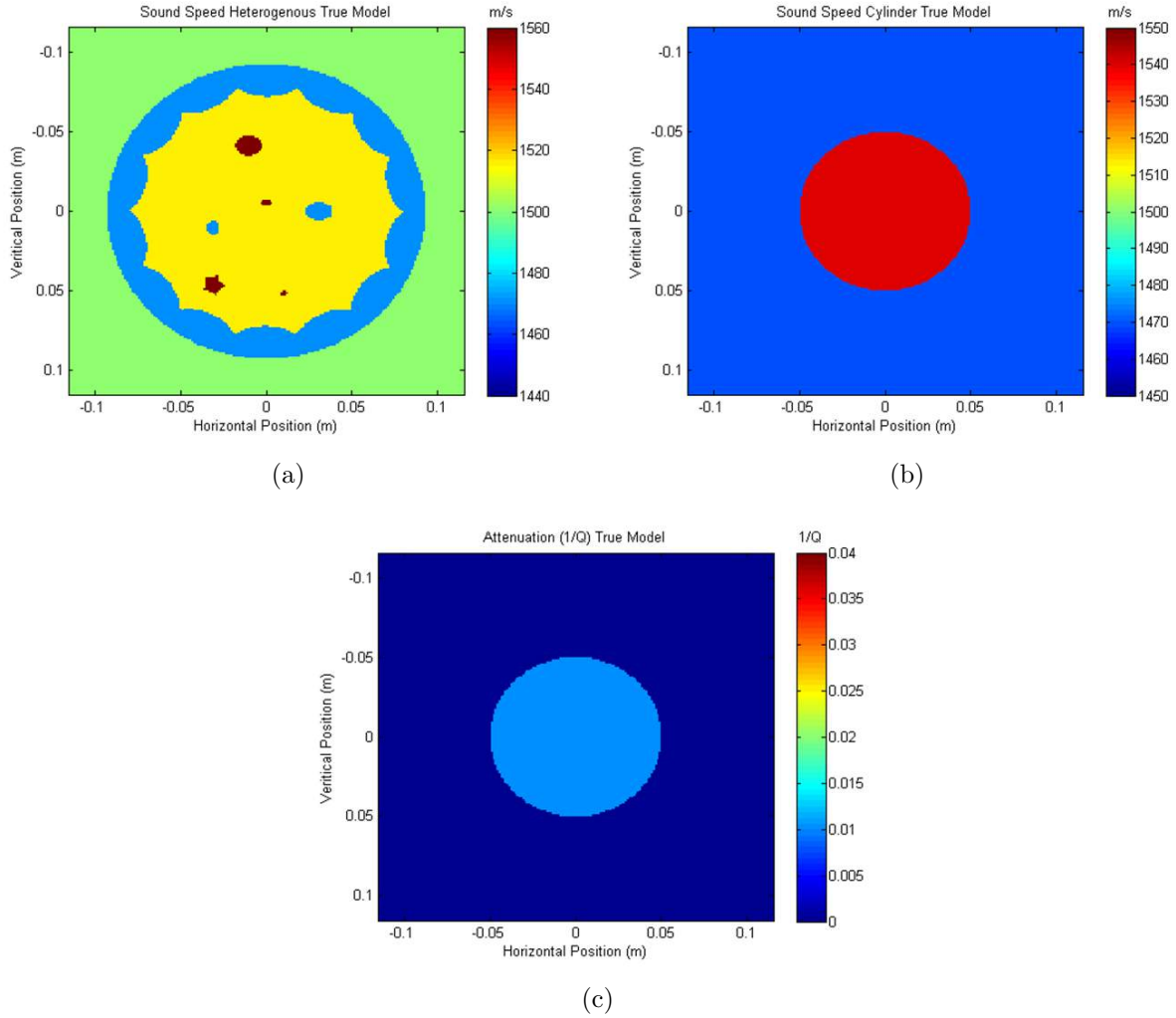


Figure 4.2: Numerical Phantoms True Models. (a) Heterogeneous sound speed phantom. (b) Homogeneous sound speed phantom. (c) Homogeneous attenuation phantom.

Reconstruction Parameters

Ten frequencies ranging from 112 kHz to 364 kHz were used as input to the frequency domain waveform algorithm. Five iterations were done at each frequency to update the model parameter of interest. A fine grid of $\Delta = \lambda/12$ was used to create simulation data in the forward modeling process. To ensure numerical stability for lower frequencies, the number of pixels in the horizontal and vertical directions were equal to 350 pixels. During inversion, in order to not commit the inverse crime, the grid size was taken to be $\Delta = \lambda/10$ or $N = 300$ pixels. We compare the sound speed and attenuation reconstructions separately.

For the sound speed reconstructions, we reconstructed a high sound speed disk 1540 m/s

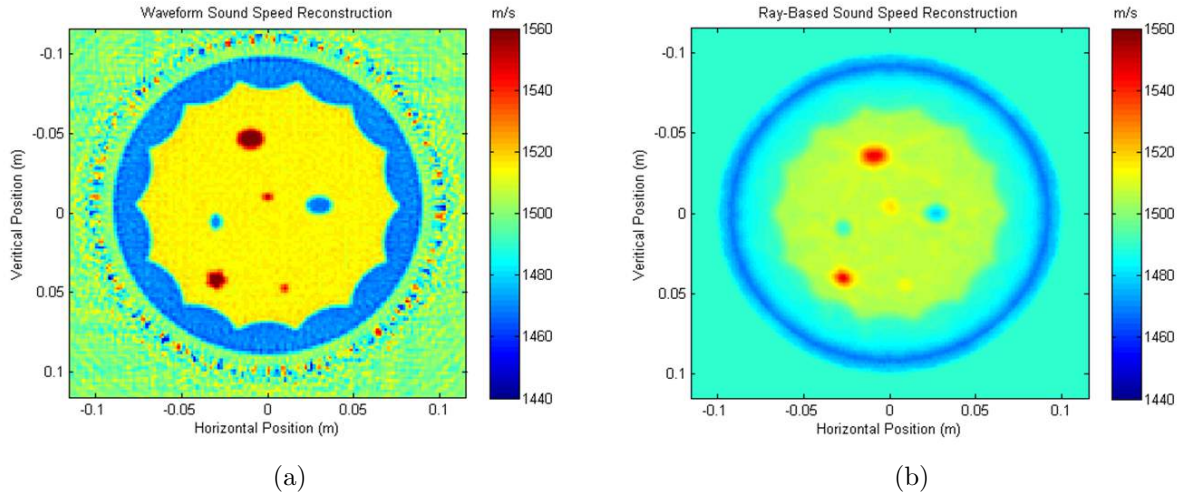


Figure 4.3: Reconstruction of Heterogeneous Sound Speed Phantom. (a) Waveform reconstruction. (b) Travel time reconstruction.

embedded in a low sound speed background medium of 1470 m/s as well as heterogeneous numerical phantom. No attenuation was present anywhere in the model. The starting model was homogeneous with a sound speed of 1500 m/s.

4.4.2 Results and Discussion: Experiment 1

Sound Speed Reconstructions

The waveform and travel time tomography reconstructions of the heterogeneous sound speed phantom is seen in Figure 4.3, while the reconstruction of the homogeneous cylindrical model is seen in Figure 4.4. The waveform tomography reconstruction better resolves the true model when compared to the travel time tomography result. The cascading outer layers over the phantom are clear. The shape of the lesions in the inside of the model, which can have critical diagnostic information [26], are much clearer in the waveform tomography reconstruction. The reconstructed sound speeds of the waveform tomography reconstruction more closely matches the true model. An estimate of the resolution can be given by the distance required for the edge response to rise from 10% to 90%. We use the homogeneous cylindrical model for this testing purpose as well for the determination of accuracy of the reconstruction. A plot profile of the reconstructed images overlaid with the true models allows

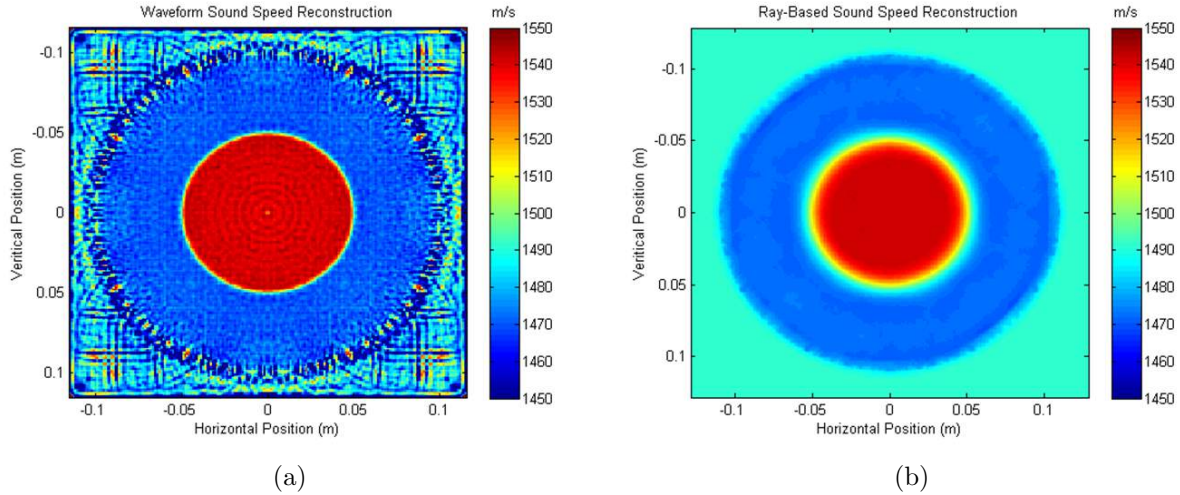


Figure 4.4: Reconstruction of Homogeneous Sound Speed Phantom. (a) Waveform reconstruction. (b) Travel time reconstruction.

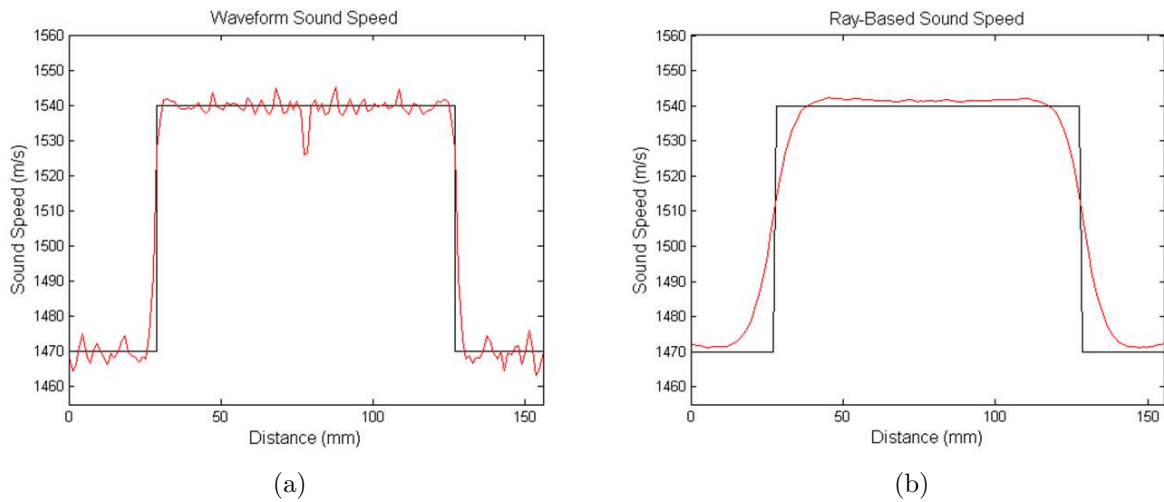


Figure 4.5: Line Profile of Homogeneous Sound Speed Model Reconstructions. (a) Waveform reconstruction profile. (b) Travel time reconstruction profile.

us to compare the resolution of the waveform and travel time tomography reconstructions of the homogeneous cylindrical sound speed model in Figure 4.5. For the travel time and waveform sound speed reconstructions, the resolution corresponds to a distance of approximately 15 mm and 3 mm, respectively. The highest frequency used in the waveform reconstruction was 364 kHz, which for a background sound speed of 1500 m/s corresponds to a wavelength of 4.12 mm. The limiting resolution of the waveform method should then be approximately $\lambda/2 = 2$ mm. For a propagation distance of $L = 200$ mm, the limiting resolution of the travel

time based reconstruction is on the order of the first Fresnel zone: $\sqrt{\lambda L} = 14.7$ mm for a dominant frequency of 1 MHz. From these considerations, we see that the edge response is a fairly accurate measure of the limiting resolution in the sound speed reconstructions. The accuracy of the reconstructions can be assessed by considering the average residual sound speed of the reconstructed sound speed image with respect to the true model. Using an ROI with a radius of 80 mm takes the sound speed transition mismatch in to account while neglecting artifacts near the transducer ring. The travel time and waveform reconstructions yield an average residual sound speed of 3.25 m/s and 0.24 m/s, respectively.

Attenuation Reconstructions

For the attenuation reconstruction, we reconstructed a homogeneous sound speed model of 1540 m/s with an embedded attenuating disk with quality factor $Q = 100$. The starting sound speed model was exact with a homogeneous sound speed of 1540 m/s and the starting attenuation model was homogeneous with a quality factor of $Q = 1000$. Because higher frequencies did not improve the reconstruction, only the first five frequencies were used for the attenuation reconstruction. The attenuation reconstruction has significantly more noise in the reconstructed model. This noise can be suppressed to a degree by incorporating a regularization term as given in equation 4.1. The attenuation reconstruction of the cylindrical attenuation model with and without regularization is seen in Figure 4.6. A plot profile of the reconstructed images overlaid with the true models allows us to compare the the waveform attenuation reconstructions of the cylindrical attenuation model. Profiles of attenuation and attenuation with regularization are seen in Figure 4.7. Due to its complicated nature, the attenuation reconstruction suffers from significant noise. Therefore, it is cumbersome to characterize its resolution in the same manner that was done for the sound speed reconstruction. We will not quote an edge response resolution, but from observing Figures 4.6(a) and 4.7, it can be seen that the attenuation reconstruction does have a fairly sharp interface boundary. Recovering the attenuation information is complicated because it is impossible to separate intrinsic attenuation due to tissue properties and attenuation due

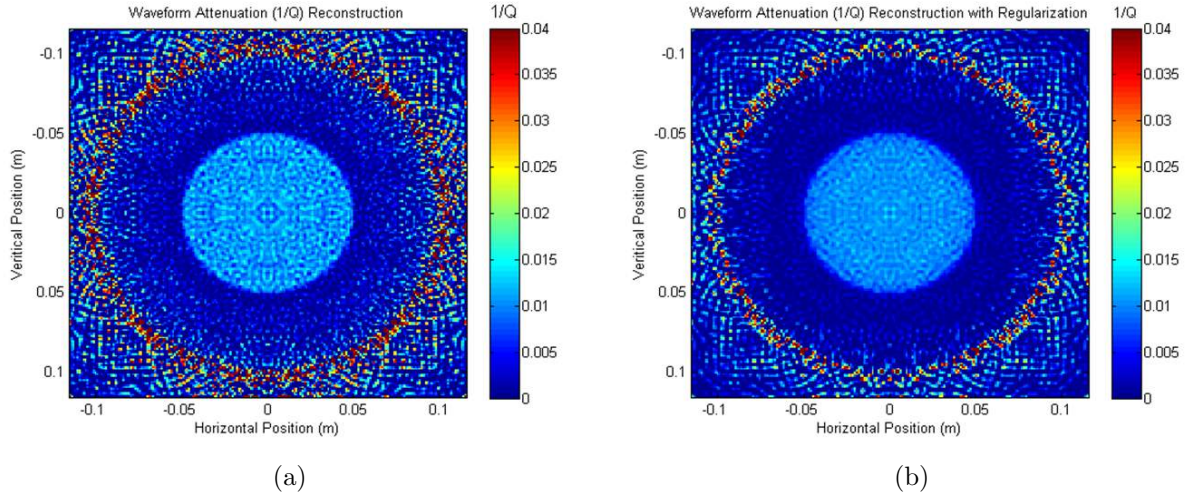


Figure 4.6: Reconstruction of Homogeneous Attenuation Phantom. (a) Waveform reconstruction. (b) Waveform reconstruction with regularization.

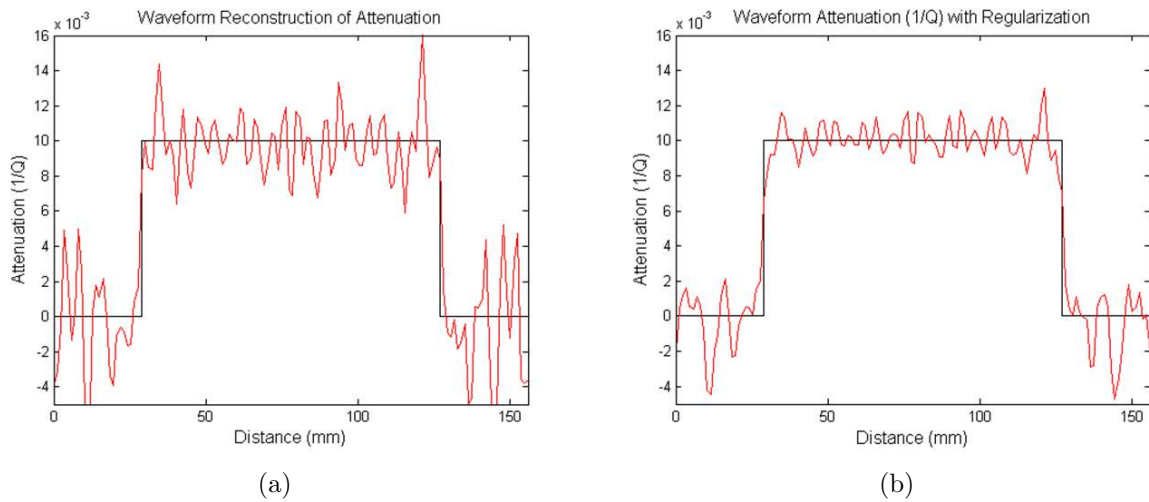


Figure 4.7: Reconstruction of Homogeneous Attenuation Phantom. (a) Waveform attenuation reconstruction. (b) Waveform attenuation reconstruction with regularization.

to velocity inhomogeneties. Taking attenuation into consideration allows for better modeling of the underlying physics and more accurate sound speed reconstructions.

Cost Function vs. Iteration Number

The cost functions for waveform sound speed and attenuation reconstructions as a function of iteration number can be seen in Figure 4.8. It can be seen that the cost functions decrease as a function of iteration indicating that the algorithm is successful in finding sound

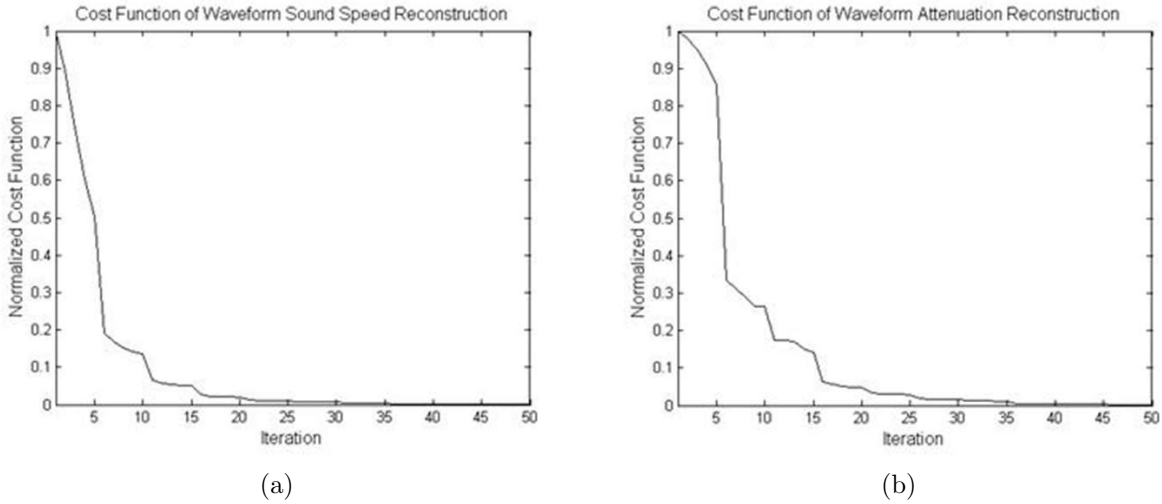


Figure 4.8: Reconstruction of Homogeneous Attenuation Phantom. (a) Waveform reconstruction. (b) Waveform reconstruction with regularization.

speed models which minimize the difference between numerical and experimental pressure field values. Note that in the frequency domain, each discrete frequency has a unique cost function. The cost functions in Figure 4.8 have been normalized so that there is a continuous decrease in their values instead of a dramatic increase every five iterations (which would correspond to moving to the next frequency).

4.4.3 Methods: Experiment 2

In order to simulate a real clinical environment, we examined the limiting resolution of our method by using a time domain waveform algorithm to generate input data for our frequency domain waveform algorithm.

True Models

time domain waveform propagation was simulated on the models seen in Figures 4.9. The first model consists of a 50 mm radius 1540 m/s cylinder embedded in a 1470 m/s background. The second model consists of a two 1 cm width 1540 m/s squares separated by 2 mm embedded in a 1470 m/s background. The separation distance of 2 mm corresponds to a separation of approximately $\lambda/3$, $\lambda/2$, and λ for frequency values of 223, 358, and 615

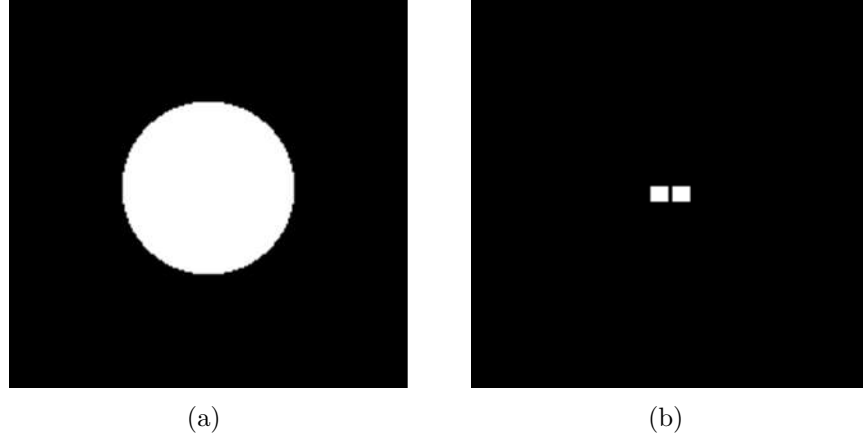


Figure 4.9: Numerical Phantom True Models. (a) 50 mm radius 1540 m/s cylinder embedded in a 1470 m/s background. (b) Two 1 cm width 1540 m/s squares separated by 2 mm embedded in a 1470 m/s background.

kHz, respectively.

Resolution

We use the edge response as given in section 4.4.1 as well as a qualitative metric. The qualitative metric uses visual inspection to see if objects separated by a fixed distance can be resolved as two objects. This is commonly referred to as the number of line pairs that can be resolved per millimeter. Due to intense scattering effects which exist in ultrasound wave propagation, only two objects are used in this comparison as opposed to CT phantoms which typically have many different objects of varying sizes.

Reconstruction Parameters

A circular array of 256 transducers was used in these simulations. Grid-point intervals of $\Delta = 0.1636$ mm, translating into about 15 grid points per wavelength for the highest frequency of approximately 615 kHz used in the inversion algorithm, was used in forward modeling. The direct arrivals of the time domain data were then windowed and tapered before being Fourier transformed into the frequency domain. This data was then sampled for the frequencies that would be used in the inversion.

The sampled data was used as input into our iterative gradient inversion procedure which

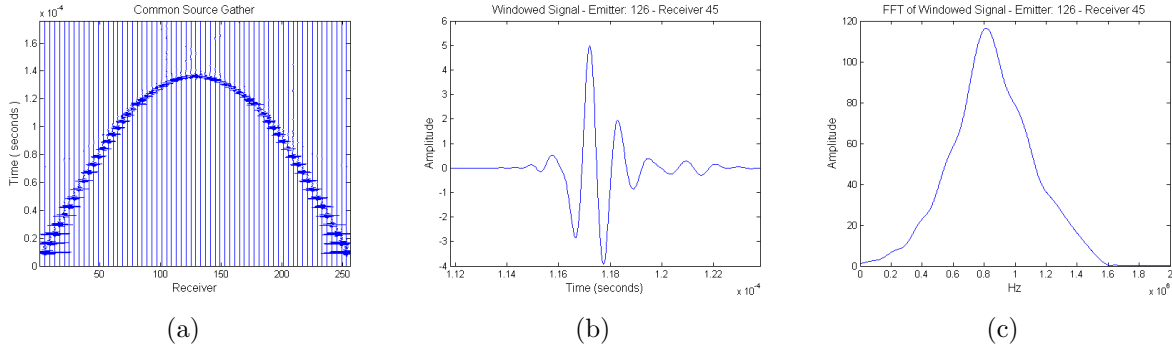


Figure 4.10: Time Domain Waveform Tomography Data. (a) Common source gather for waves propagated through a cylindrical model. (b) Windowed waveform for a particular source receiver pair. (c) Magnitude of Fourier transform of windowed waveform.

compares the forward modeled data with data generated by the frequency domain waveform algorithm. Grid-point intervals of $\Delta = \max \{\lambda/10, \lambda_N\}$ was used for the reconstruction, where λ_N corresponds to the wavelength that would have a mesh size of 300 pixels within the problem domain. The initial sound speed model used for frequency domain algorithm corresponded to the approximate speed of sound in water: 1500 m/s. By comparing both data sets, the sound speed distribution was iteratively updated 5 times for each frequency for a total of 19 frequencies ranging from 108 kHz to 615 kHz.

Every fourth waveform of a common source gather propagated in the time domain through the cylindrical numerical model in Figure 4.9(a) is shown below in Figure 4.10. The windowed portion of a waveform and the magnitude of its Fourier transform are also shown.

4.4.4 Results And Discussion: Experiment 2

The frequency domain waveform reconstructions of both models are shown in Figures 4.11 and 4.13. Midline profiles comparing the reconstructions to the true model are shown in Figures 4.12 and 4.14.

It can be seen that reconstruction of the cylindrical model matches very well with the true model. The 10% and 90% response is given by 1.6 ± 1.1 mm. This compares very well to the results presented in section 4.4.2. If we consider the model with two embedded squares, we see that the resolution is somewhere between λ and $\lambda/2$ since the reconstruction

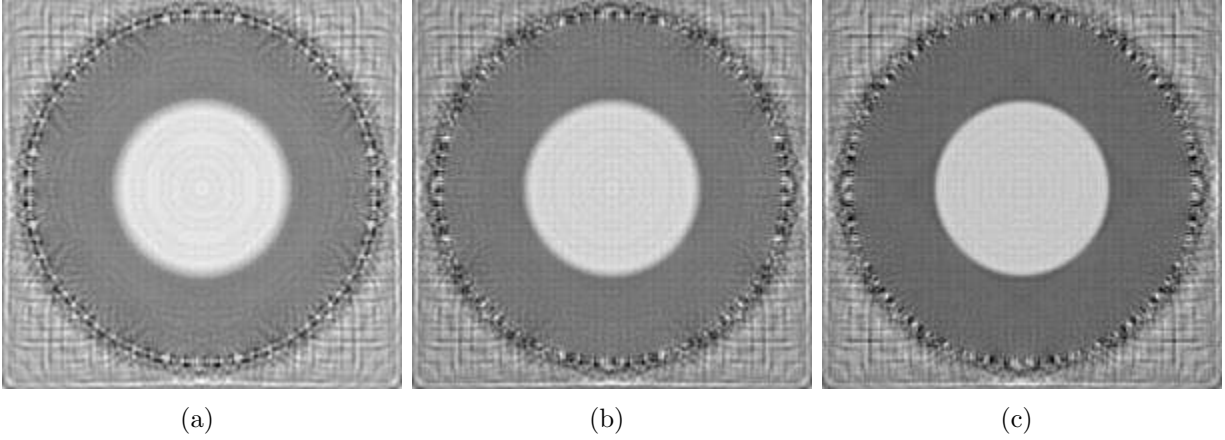


Figure 4.11: Reconstruction of Cylindrical Model. 50 mm radius 1540 m/s cylinder embedded in a 1470 m/s background. Sound speed images of 5th iteration of frequency: (a) 223 kHz, (b) 358 kHz, and (c) 615 kHz.

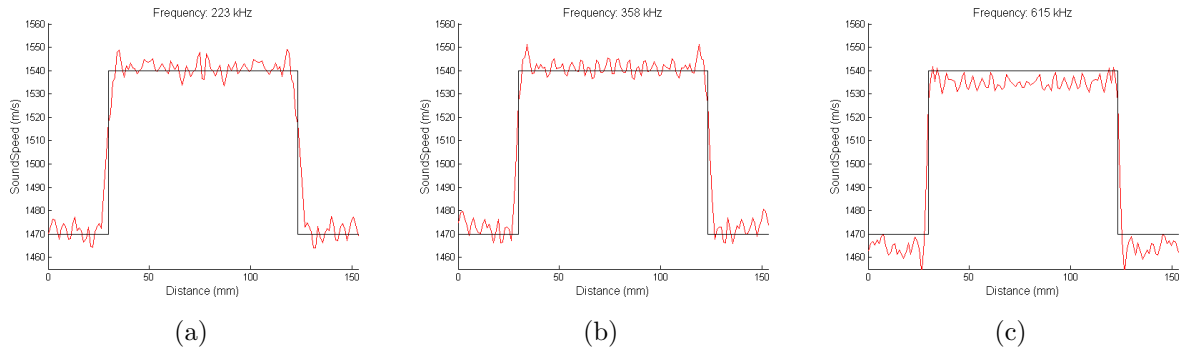


Figure 4.12: Profiles of Reconstruction of Cylindrical Model. 50 mm radius 1540 m/s cylinder embedded in a 1470 m/s background. Midline profiles of 5th iteration of frequency: (a) 223 kHz, (b) 358 kHz, and (c) 615 kHz.

is well resolved in the latter case but not so much in the former. This agrees with the edge responses of both experiments.

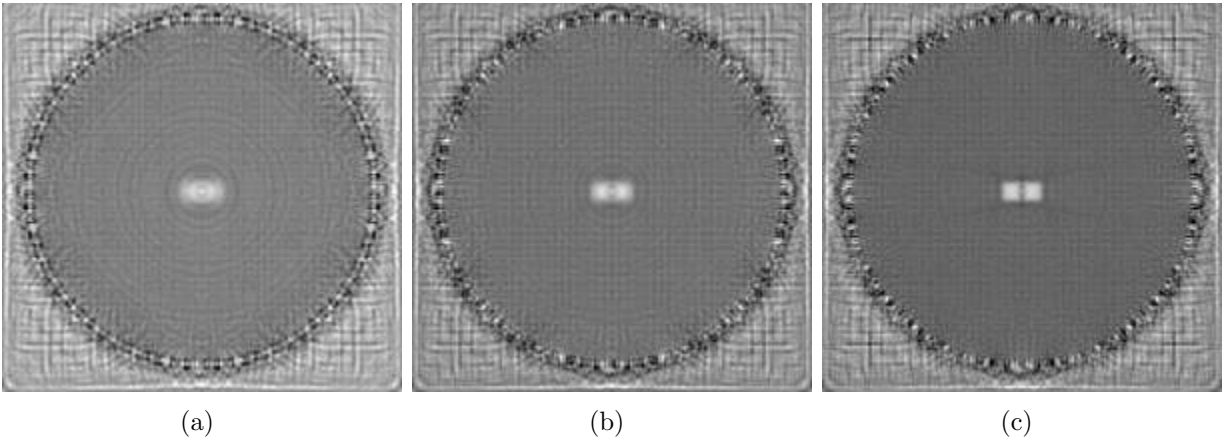


Figure 4.13: Reconstruction of Squares Model. Two 1 cm width 1540 m/s squares separated by 2 mm embedded in a 1470 m/s background. Sound speed images of 5th iteration of frequency: (a) 223 kHz, (b) 358 kHz, and (c) 615 kHz.

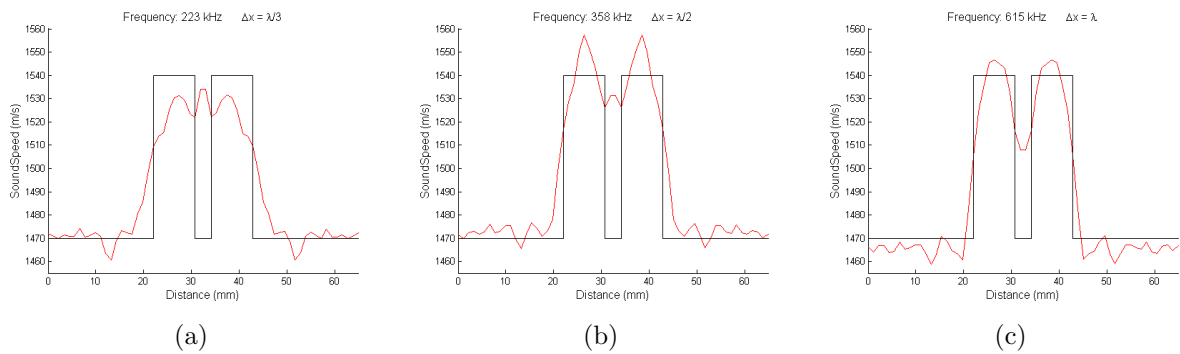


Figure 4.14: Profiles of Reconstruction of Squares Model. Two 1 cm width 1540 m/s squares separated by 2 mm embedded in a 1470 m/s background. Midline profiles of 5th iteration of frequency: (a) 223 kHz, (b) 358 kHz, and (c) 615 kHz.

CHAPTER 5: Acquisition Hardware, Signal Processing, and Other Practical Considerations

In this chapter, we describe the hardware used to gather experimental data and the steps needed for the successful inversion of experimental data. The same steps are applied to data acquired by the two considered tomographic ultrasound units. These include: computing a low resolution sound speed starting model using travel time tomography, applying digital signal processing to the raw signals to extract the frequency components used for the optimization, compensating for the transducer response, and estimating the unknown source signal. We will also discuss other practical considerations and observations that do not fit so well in other chapters.

5.1 Acquisition Hardware

The two ultrasound tomography devices used to gather data are seen in Figure 5.1. The first device [42], an early prototype developed at the Karmanos Cancer Institute, has a ring array transducer with a 100 millimeter radius, 256 transducer elements, and a signal bandwidth centered at 1.5 MHz. The second device [43], a recent prototype developed by



Figure 5.1: Ultrasound Tomography Devices. (a) CURE. (b) SoftVue.

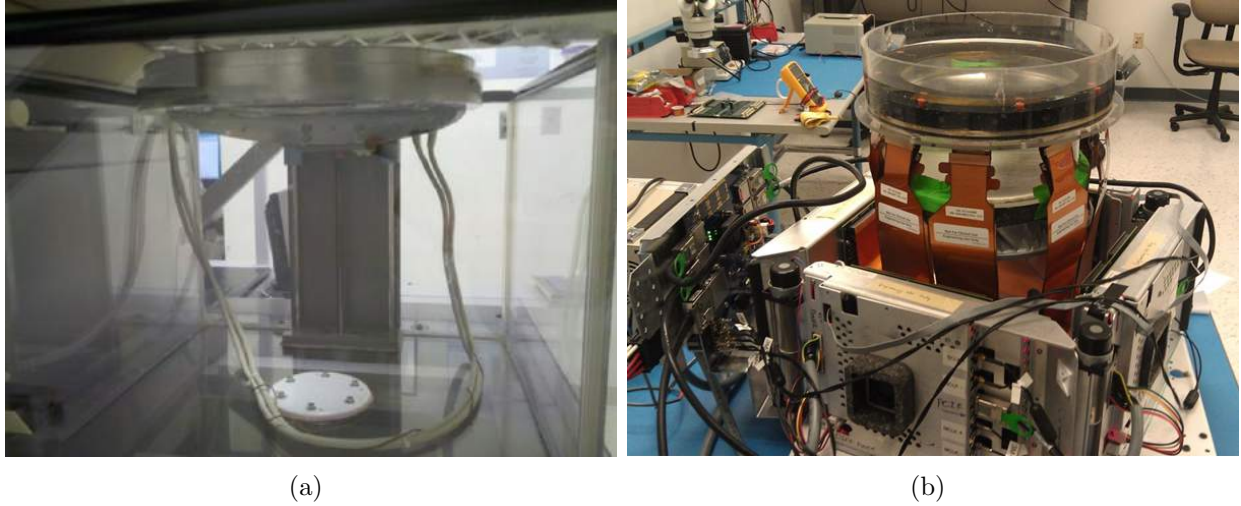


Figure 5.2: Ultrasound Tomography Device Transducer Rings. (a) CURE. (b) SoftVue.

Delphinus Medical Technologies, Inc., has a transducer with a 110 millimeter radius, 2048 transducer elements, and a signal bandwidth centered at 2.75 MHz. Only 256 transducer elements were used in this work to facilitate comparison with the older prototype and to minimize reconstruction time. The two devices, uniquely different in their manufacturing, have different performance properties and provide excellent test cases to assess the robustness of the proposed waveform tomography reconstruction scheme. The transducer rings of both devices are seen in Figure 5.2. An example of a patient exam and the placement of the breast are seen in Figure 1.4.

5.2 Signal Processing

The proposed algorithm works on the frequency components extracted from the raw time series. We use data acquired by the newer ultrasound tomography device for the discussion in this section.

5.2.1 Acquired Ultrasound Data

In Figure 5.3, we see an example of a common shot gather of raw experimental data traversed through a breast with scattered density. A common shot gather is a collection of received time series for all receivers from a pulse excitation by one transmitting transducer.

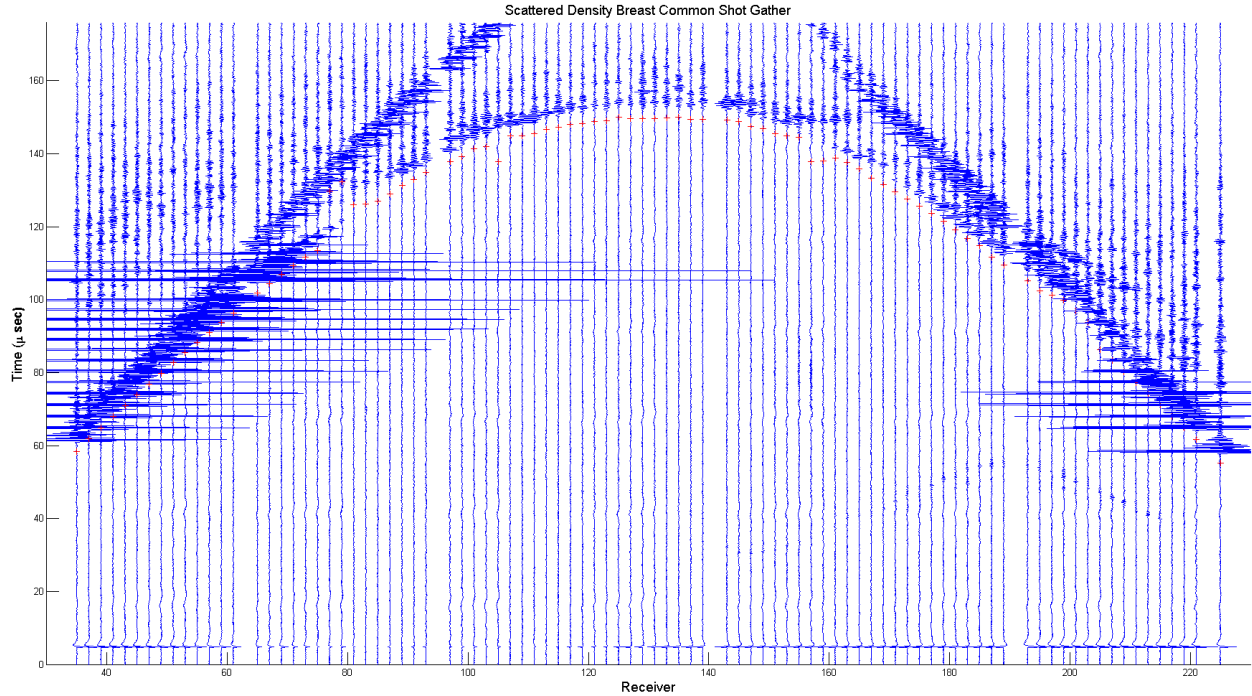


Figure 5.3: Common Shot Gather of Scattered Density Breast. Overlaid are red crosses that are the first arrival times determined by the automatic TOF picking algorithm.

In each plot, the corresponding time-of-flights used for frequency extraction are marked by red crosses. The data has not been processed and represents the raw signals obtained by the experimental device. The amplitudes have been normalized to fit on the plot. More examples of common shot gathers are given in Appendix C. This includes examples of a water shot, a scattered density breast, and an extremely dense breast. Included are the modifications to the received signals due to preprocessing as well as the corresponding frequency spectrums. Note that the presence of an object alters the shape of the waveforms with respect to the water shot. The altered waveforms have decreased amplitude and more complicated wave phenomena. For example, the scattered density breast alters the waveforms less than an extremely dense breast. This can be seen, for example, by comparing the amplitudes of far offset waveform relative to near offset waveforms that haven't traveled through the breast. Since near offset waveforms are not attenuated or scattered by traveling through the breast, their amplitudes are considerable higher than the other waveforms in the common shot gather. Depending on the deformation of the data, the automatic time picker fails to accurately pick the correct travel time. Later arriving reflection events arrive

after the first transmitted portion. These signals are mostly clearly seen in the near offset receivers (i. e. 40–60 and 200–220). Of one particular interest are the two straight lines of waveforms present in the common shot gather figures. This phenomena occurs as a result of waveforms causing multiple scattering events on the transducer ring that further cause more scattering events on the transducer ring. The net result of this resonance is the generation of waveforms along the straight lines seen in the common shot gather figures. Other resonance phenomena can occur as well. For example, resonance noise caused by the power supply can create artifacts in the reconstructed images.

We can select a single waveform of the common shot gather. An example of a single raw time series is seen in Figure 5.4(a). Each time series is processed before injection into the the algorithm. An example of the unfiltered signal, its filtered form, and the corresponding frequency magnitude spectrum is seen in Figure 5.4. The signal processing of the raw time signal is achieved by applying the steps below.

5.2.2 Time Windowing

The time of first arrival for each waveform is evaluated using an automatic travel time estimation method described in [99, 100]. These travel times allow us to define windows which extract the primary transmitted portion of the received waveforms and reject reflected and multi-scattered signals. This is done to force the algorithm to match the primary features of the true sound speed model [69]. The length of the window is chosen so that it includes the contribution of the primary transmitted waveform. Short cosine tapers (approx. 0.5 μ s) are applied to both sides of the window before Fourier transformation to avoid Gibbs phenomena.

5.2.3 Exponential Damping

We dampen the tail of the signal for the same reason we window. A damping profile of the form $\max\{1, \exp[-(t - t_0 - t_d)/\tau]\}$ is applied to every waveform as a means to further focus the inversion process on information contained in the primary transmitted signal. We

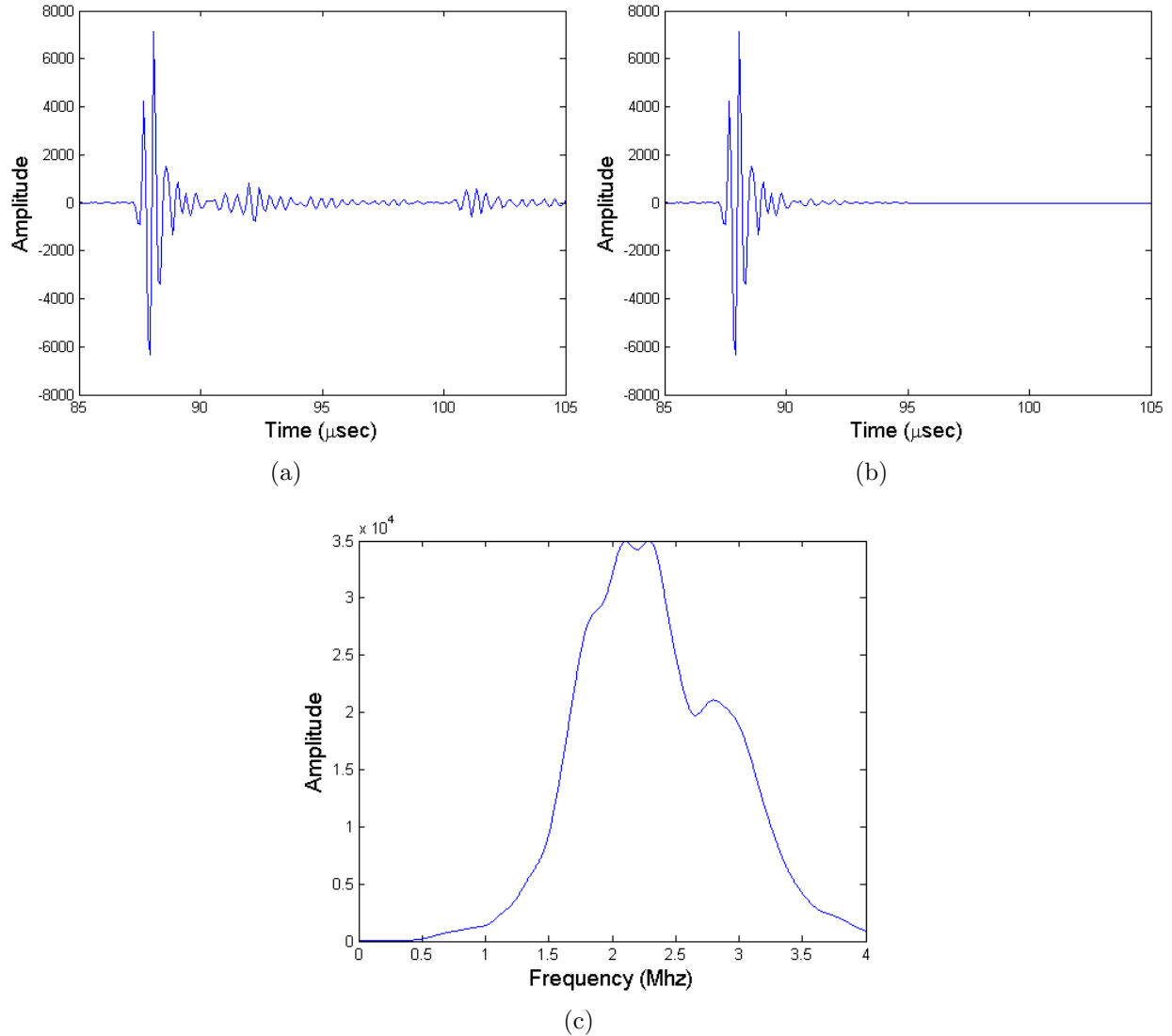


Figure 5.4: Processing of Raw Ultrasound Signal. Data generated by newer prototype. (a) Original waveform. (b) Processed waveform. (c) Magnitude spectrum of processed waveform.

use a value of t_d that begins damping the signal after the main transmitted portion of the waveform (approx. $5 \mu\text{s}$ after the travel time t_0), and a short scaling factor τ (approx. $1 \mu\text{s}$) to quickly attenuate the later portion of the signal that is contaminated by non-transmitted components.

5.2.4 Waveform Selection

A calibration of the ring array transducer [101] and the determination of travel time statistical outliers in the clinical data set allow us to detect faulty transducer elements and

discard waveforms that are too noisy to be included in the reconstruction process. We use an automated calibration method which estimates the position of the transducer elements using travel time measurements done in a water bath at controlled temperature. The calibration method also analyses the power of the transmitted signals to flag faulty transducer elements. For example, the transducer element directional beam profiles make small angle emitter-receiver contributions unreliable. For this reason, we omit waveforms that do not lie within an arc of approximately 270 degrees with respect to the source transducer.

5.2.5 Fourier Transformation

The processed waveforms are then Fourier transformed to extract the frequency components given as input to the optimization process. A typical magnitude spectrum for the new device is shown in Figure 5.4(c). We start the iterative optimization procedure with the lowest frequency that has enough energy (around 400 kHz for the older unit and 500 kHz for the newer unit). We iterate multiple times on that frequency and then move to the next frequency using an increment of 30 kHz up to a maximum frequency of 1 MHz. Since computation cost is not linearly proportional to the size of mesh, and thus, the chosen frequency, the maximum reconstruction frequency of 1 MHz was found to be an appropriate maximum frequency since further improvements in the quality of the reconstructed image were overshadowed by significant increases in computation cost and model mismatch. The chosen optimization process allows us to gradually incorporate shorter wavelength features to prevent the algorithm from being stuck in a local minimum. Experiments have shown that this optimization schedule performs well across all considered data sets. Note that the current transducer ring has not been optimized to operate at such low frequencies. The energy available in the considered frequency range is significantly lower than what is available near the central frequency (Figure 5.4(c)). Thus, further optimization of the acquisition hardware holds great promise for even better image reconstruction quality. This would be especially true for reconstructing images of dense breasts.

5.2.6 Transducer Response

For the simulated data set to best match the experimental one, we must also take the characteristics of the transducer beam profile into account. This can be achieved either by including the transducer response in our propagation model or by modifying the waveforms to best match a simple numerical model that assumes omni-directional point sources. The former approach would require very careful calibration of our algorithm for a successful inversion. For simplicity, we have chosen the latter approach. We normalize the magnitude spectrum of both the simulated and experimental data sets. In other words, we only match the phase of the frequency components in the inversion process. However, neglecting amplitude information may lead to residual artifacts. This is true especially in a propagation medium rich with scattering. In addition, neglecting amplitude information by completely normalizing the magnitude spectrum would void the possibility of *in vivo* attenuation reconstruction.

5.2.7 Source Signal Estimation

In order to solve our forward problem, the input signal s must be known. We could calibrate our transducers and obtain the signal, but that would add an additional layer of complexity to our algorithm. In addition, by estimating the source, we provide an additional degree of freedom to the inversion problem. For a given sound speed model, this is a linear estimation task. We need to find the optimal complex valued source scaling factor s_γ such that the simulated and experimental measurements best match in a mean squared sense. The optimal value is obtained through orthogonal projection [56] and is given by

$$s_\gamma = \frac{\mathbf{d}_{obs}^H \mathbf{u}_{obs}}{\mathbf{u}_{obs}^H \mathbf{u}_{obs}}. \quad (5.1)$$

Using this scaling factor, the source vector and field values are scaled to $\mathbf{s} \rightarrow s_\gamma \mathbf{s}$, and $\mathbf{u} \rightarrow s_\gamma \mathbf{u}$, respectively. The reconstruction algorithm alternates between updating the source signal using the above scaling factor for a known sound speed model and estimating the sound

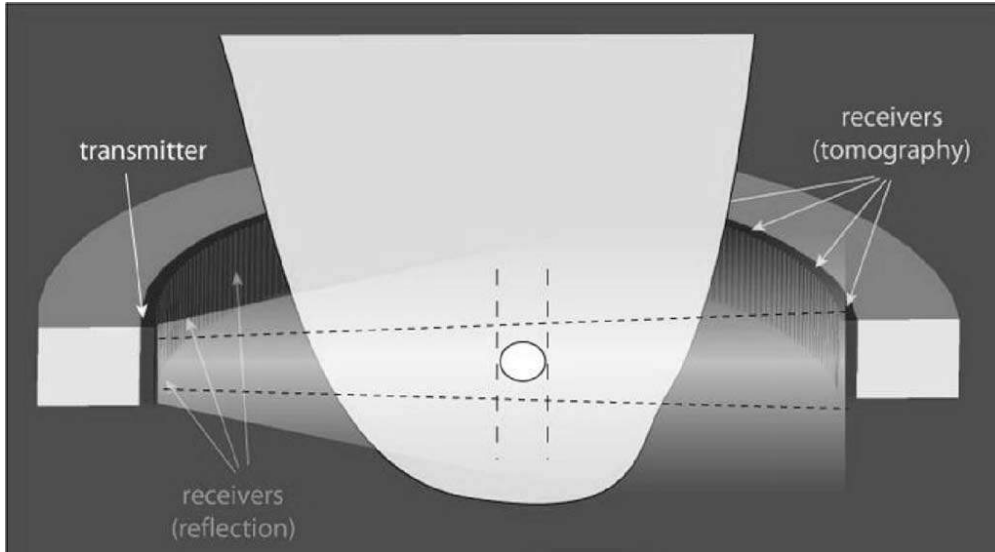


Figure 5.5: Schematic of a Vertical Profile of an Ultrasound Scan.

speed model for a given source signal.

5.3 Other Practical Considerations

In this section, we will discuss some practical considerations and observations of the waveform tomography algorithm. These topics include: the finite slice thickness of transducer ring and its effects on the reconstructed image, the effects of using different numbers of transducers elements, an example of phase mismatch and its relation to convergence, and the computation time of the algorithm.

5.3.1 Slice Thickness and Vertical Beam Profile

We do not use a 3D ultrasound tomography acquisition system (for example [102]), however we use a focusing lens on our ultrasound transducers so that most of the energy is concentrated within the coronal plane. Thus, each coronal slice of the breast integrates the vertical dimension resulting in a finite slice thickness. A schematic of this is seen in Figure 5.5 (source [42]). A complete sampling of the breast is ensured by having an inter-slice spacing less than the slice thickness. When viewing an image, one needs to have in mind that the image is a 2D projection of the all the information present in the 3D cylinder defined by

the slice thickness and the 2D geometry. The finite vertical dimension of the transducers and manufacturing limitations hinder our ability to have images with less slice thickness. Unfortunately, the finite slice thickness of our imaging method results in a degraded z-plane resolution.

Another problem caused by the finite slice thickness of the ultrasound beam is that there are some problems registering sound speed and reflection images due to the sloping breast surface. From Figure 5.5, a pulse emitted from the ultrasound beam at the left hand size of the image will be reflected by the top breast surface (the top dashed line) before the lower breast surface. This will bias the reconstructed image to the shape of the top portion of the beam profile. In contrast, the travel time tomography algorithm will take the fastest time through the breast which will likely be near the bottom. The waveform tomography will take the integrated vertical path since it utilizes the entire waveform. An example of this phenomena is seen in Figure 5.6. In this example, we see a series of slices showing registration problems in a sloping breast. From looking at the reflection and sound speed images corresponding to the same slice, we see that the breast seems to have a different size as defined by its outside contour. This problem is very apparent as we scan closer to the nipple. Again, this is due to the sloping nature of the breast and the manner in which the ultrasound transducer ring receives reflected and transmitted signals. Also, we make a very unrelated observation and note air bubbles creating bright white circular objects artifacts in the bottom row of the reflection images.

5.3.2 Number of Transducer Elements

A test was performed to see the effects of using less emitters in frequency domain waveform tomography. A total of 256 receivers were always used while we changed the number of emitters from 256 to 8 in factors of 2. We used a numerical phantom composed of a 1540 m/s 50 mm disk in a background of 1470 m/s with no attenuation added. Forwarding modeling was done in the frequency domain at 112 kHz with a very fine mesh of $\Delta = \lambda/23$ ($N^2 = 1600$ nodal points). Reconstruction was also done in the frequency domain at 112 kHz but

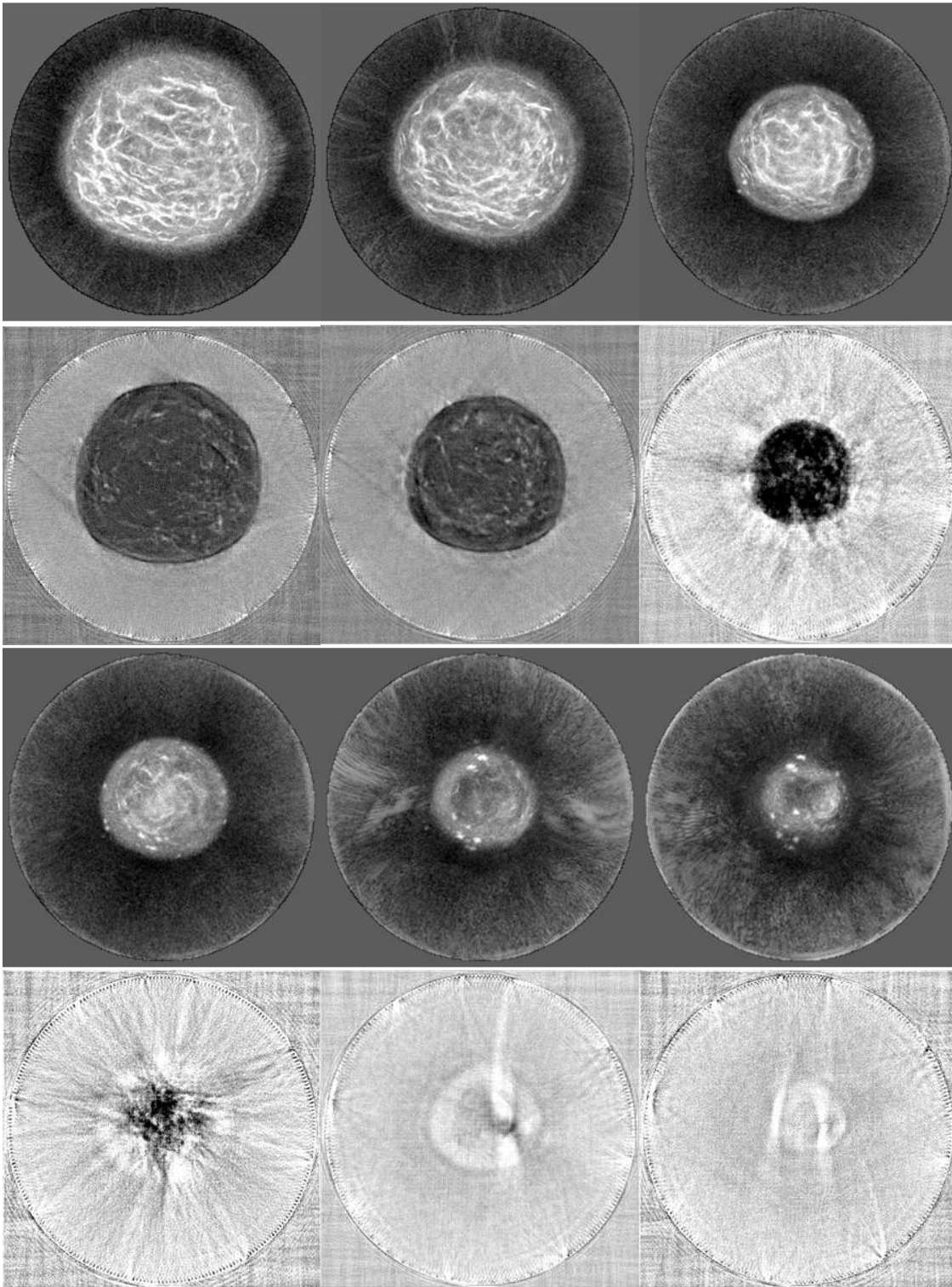


Figure 5.6: Registration Problems in a Sloping Breast. Images consist alternating row of reflection envelope images and waveform sound speed images. Each vertical pair of reflection and sound speed images correspond to the same slice.

with a coarser mesh of $\Delta = \lambda/17$ ($N^2 = 900$ nodal points). The model was updated via gradient methods where we determined the step length at every iteration by line search. The reconstruction results are shown in Figure 5.7. It is seen for this limited test, that a quality reconstruction can still be reconstructed using only 64 emitters. Since the cost of running the algorithm is directly proportional to the number of emitters that are used to insonify the medium, a reduction in the number of emitters will result in a reduction in computation cost. Note that we did not vary the number of receivers in this test. Having more receivers, and thus more data, would improve the quality of the reconstruction process by making the matrix inversion problem more well-posed. For the SoftVue device, we can possibly have 4x more receiving transducer elements. Adding or subtracting the number of receivers will have no practically effect on computation cost since we already solve the numerical wave field for the entire domain. We would just sample more indices of the numerical wave field corresponding to the new receiver locations.

5.3.3 Convergence Based on the Accuracy of the Starting Model

As stated in section 4.3.1, the starting sound speed model is very important for a successful inversion. The starting model needs to be accurate enough to predict numerical wave fields with phases within a π window of the true phase. The most simple test to see this behavior is in a completely homogeneous medium. Consider the inversion of a medium that has a constant sound speed $\mathbf{c} = c$. We can then let $\mathbf{c}_0 = c_0$ for different values of c_0 . We can also vary the operating frequency f ($\omega = 2\pi f$). The result of this experiment is seen in Figure 5.8. We plot the number of iterations it takes for our waveform tomography algorithm to converge to the true model $c = 1500$ m/s given a different initial sound speed c_0 and operating frequency f . We see that at lower frequencies (thus a longer wavelength and oscillation period), a greater mismatch between the true model and the starting model is tolerable. The algorithm takes longer to converge to the true model, but it is still able to converge to it. The longer period of oscillation means that it much easier to satisfy the π criteria of phase mismatch. As the frequency increases, larger offsets no longer satisfy

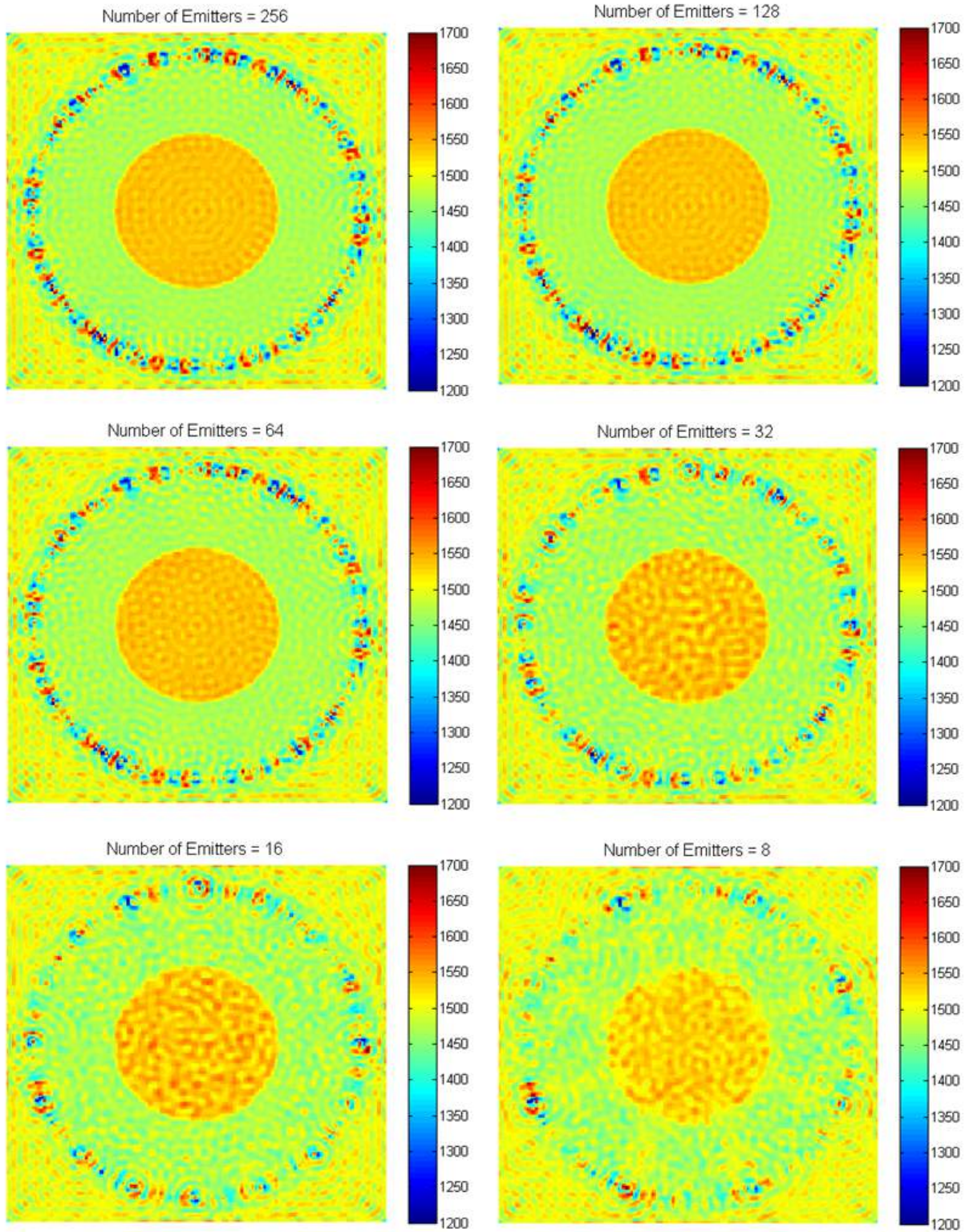


Figure 5.7: Varying Emitters. Reducing the number of emitters used in the reconstruction process affects the quality of the reconstructed image.

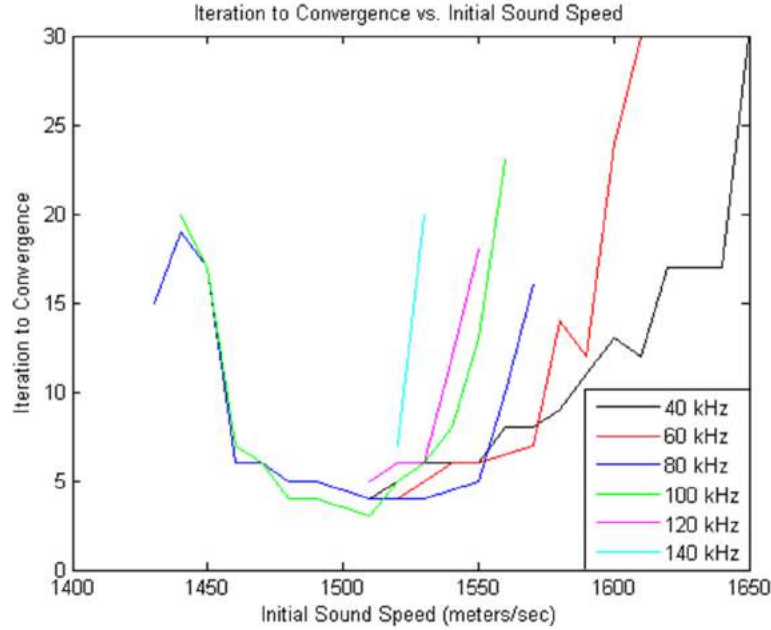


Figure 5.8: Convergence to a Homogeneous Sound Speed Model as a Function of the Starting Sound Speed Model and Operating Frequency.

the π criteria since the period of oscillation has decreased. For example, for an operating frequency of 60 kHz, a starting model of 1650 m/s would not converge to the true model of 1500 m/s. Note that we have plotted both negative and positive offsets for only 80 and 100 kHz. Also, even if we start with the exact solution, various factors, for example the estimation of the source signal, forces the algorithm to find sound speed models that explain the difference between numerical wave fields and experimental wave fields (which in this case are also numerical). Since changing a reconstruction parameter would change the numerical field values created, it would still take a finite number of iterations to converge to the true model even if the exact solution was given.

5.3.4 Computation Time

When comparing travel time and waveform tomography methods, one of the biggest drawbacks of the waveform approach is computation time. Since we are solving a very large system of equations, we are constrained by the capabilities of current matrix inversion methods and hardware capabilities. The later restriction can be alleviated by simply waiting

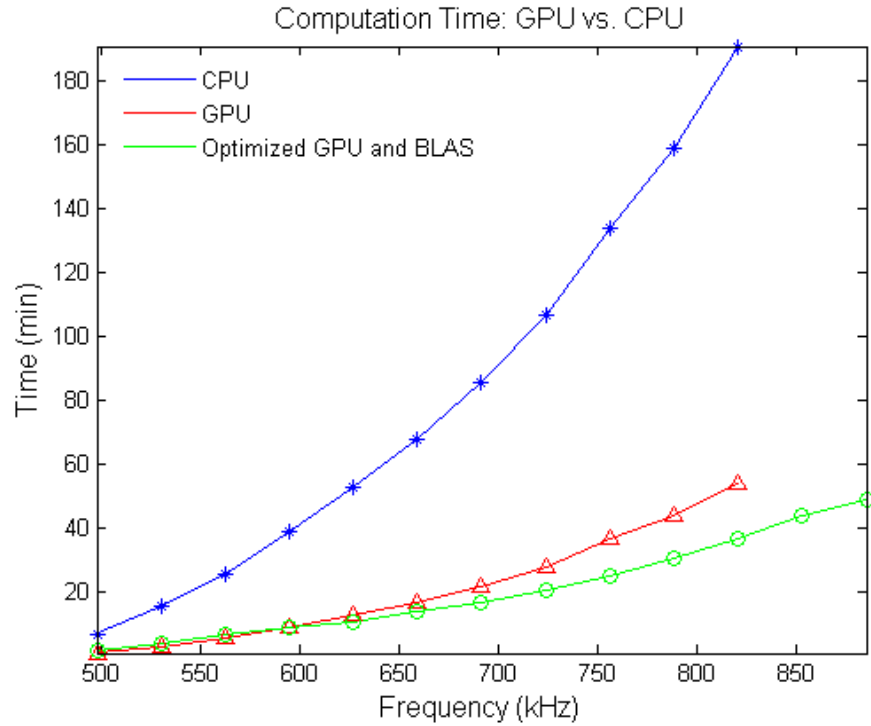


Figure 5.9: Computation Time: GPU vs. CPU. The total accumulated time is displayed on the y-axis.

until faster processors become available. The former restriction is more difficult to deal with. For example, we use a highly optimized LU decomposition method [91] to solve the system of equations in equation 3.2. We use this method because once we factor the matrix \mathbf{S} representing the discretized Helmholtz operator into its LU form: $\mathbf{S} \rightarrow \mathbf{LU}$, we can rapidly apply the factors $(\mathbf{LU})^{-1}$ to different source vectors \mathbf{s} representing excitation from different source transducer locations. We can use graphical processing units (GPUs) to improve computation time by parallelizing serial threads [103]. This significantly reduces the time needed to apply the LU factors to source vectors. However, not all problems are “highly parallelizable.” For example, a “for loop” that loops over an array and increments the value of each element of the array by 1 is a highly parallelizable problem. However, if we apply an operator on an element of the array that depends on other elements of the array, then it is not as parallelizable as the simple addition example. The LU decomposition step is a bottle neck for GPU capabilities. For example, the LU decomposition algorithm must find the pivot locations (i.e. reducing a matrix to row-echelon form [104]) which are necessary

to determine the final LU factored form. This step and other steps in the LU factorization procedure are not highly parallelizable. However, research is being done on applying GPUs to this problem. Regardless, applying GPUs to the parallelizable portion of our matrix inversion method greatly improves the computation speed. Dr. Cuiping Li implemented GPUs in our waveform tomography algorithm and the results are shown in Figure 5.9. It can be seen that the GPU method greatly reduces the computation speed of the method. By optimizing the Basic Linear Algebra Subprograms (BLAS) libraries, further improvements are made in the computation time. By experimenting with the fitting of the data in Figure 5.9, we found that the computational cost is quadratically proportional to the modeled frequency. This agrees with a derivation given in [83]. As a final comment in this section, we note that frequency domain waveform methods are faster than time domain approaches since we only model a finite number of the frequency components in a signal. The frequency domain approach also has the advantage that one can end the iteration procedure of incorporating higher frequencies at any desired time. If clinically requirements dictate a certain time frame, then those requirements can be met at the expense of the quality of the final image.

CHAPTER 6: In Vivo Sound Speed Imaging

In this chapter, we will present the results of applying our waveform tomography algorithm to experimentally gathered data. We will first give a comparison of waveform and travel time tomography methods. This will include the *ex vivo* sound speed reconstruction of a tissue mimicking phantom and *in vivo* sound speed reconstructions of patient data. We will next compare *in vivo* waveform tomography sound speed images to MRI to show that there are many concordant findings across the two modalities. Note that we are not presenting attenuation reconstructions of experimentally gathered data as additional work is required for the successful inversion of attenuation properties.

6.1 Comparison of Waveform and Travel Time Tomography

In this section, we present *in vivo* waveform and travel time tomography reconstruction results. We highlight the improvements made upon existing travel time imaging methods and the robustness of the proposed algorithm to data acquired by the two considered ultrasound tomography units. Note that our goal is not to compare the two units in terms of image reconstruction quality, but to demonstrate the applicability of the algorithm to data sets acquired with different devices.

6.1.1 Physical Phantom Results

A physical tissue mimicking breast phantom, built by Dr. Ernest Madsen of the University of Wisconsin, was used to assess the real-world reconstruction ability of our algorithm. It has been previously used in the studies presented in [3, 42]. An x-ray computed tomography (CT) image of the phantom is shown in Figure 6.1(c). The phantom has scanning characteristics of a highly scattering predominantly parenchymal breast, and it has two embedded high speed tumors and two low sound speed fat inclusions which are surrounded by a cascading

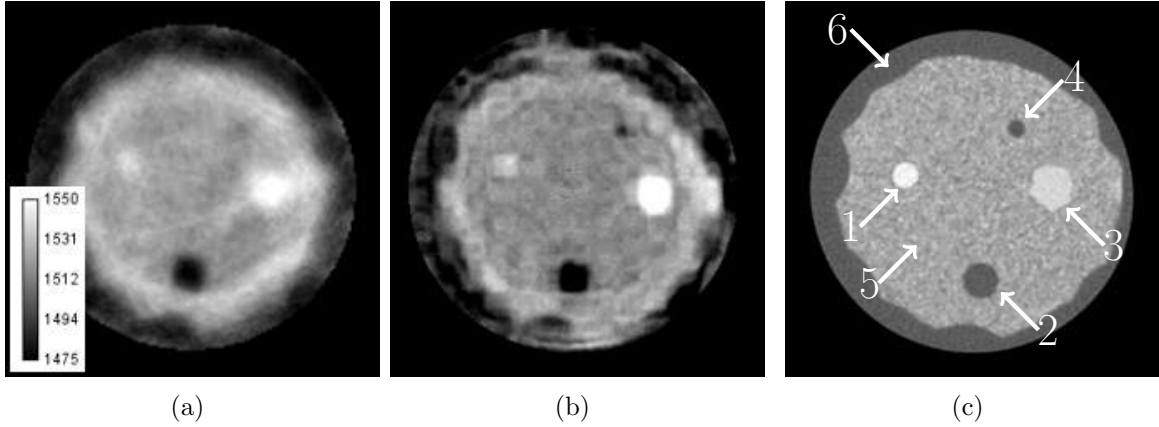


Figure 6.1: Reconstructions of Physical Breast Phantom. Data acquired by older ultrasound tomography unit. Gray scale values in the sound speed images correspond to a range of 1475–1550 m/s. Brighter areas correspond to higher sound speed. (a) Travel time tomography method. (b) Waveform tomography method. (c) Computed tomography reference with arrow overlays labeling structures: (1) Small tumor, (2) Large fat deposit, (3) Large tumor, (4) Small Fat deposit, (5) Glandular tissue, (6) Subcutaneous fat layer.

subcutaneous fat layer that is further surrounded by a layer of skin. The travel time and waveform tomography reconstruction results of data obtained from the old prototype are shown in Figure 6.1. An x-ray computed tomography (CT) scan is also shown in Figure 6.1(c) to highlight concordant findings. Note the phantom images have been manually masked so that the reader can focus on the contained lesions instead of artifacts outside the field of view. Also, in comparison to *in vivo* patients scans, the temperature of the water bath was approximately 22 °C.

Morphological Comparison

The waveform tomography reconstruction method show significant improvements in the morphological quality of the reconstructed image over the method based on travel times. For example, the inclusion at 1 o'clock is clearly visible in the higher resolution waveform image while it is barely visible in the travel time tomography image. In addition to finding smaller lesions, the shape and margins of the larger lesions in the waveform image are better delineated and match more closely the CT reconstruction. Since the shape and margins of tissues, including tumors, cysts, and parenchyma have critical diagnostic value in the

Structure	Reference Values	Travel Time Rec. ($\mu \pm \sigma$)	Waveform Rec. ($\mu \pm \sigma$)
Large tumor	1559	1551 ± 10	1551 ± 5
Small tumor	1549	1542 ± 2	1535 ± 3
Large fat deposit	1470	1501 ± 10	1490 ± 9
Small fat deposit	1470	1524 ± 3	1511 ± 4
Glandular tissue	1515	1528 ± 3	1521 ± 3

Table 6.1: Comparison of Reference Values (m/s) to Travel Time and Waveform Tomography Reconstructions of Breast Phantom. Values are reported using the mean sound speed μ in the ROI and the corresponding standard deviation σ .

assessment of disease [26], an observer would be able to make a more accurate diagnosis with the additional information present in the waveform reconstruction.

Quantitative Comparison

We assess the accuracy of the reconstructed sound speed values by selecting a region of interest (ROI) around the structures labeled in Figure 6.1(c). Each ROI is contoured to match the morphological feature of the imaged lesion. For an ROI of N pixels, we obtain the mean sound speed μ and unbiased standard deviation σ as given by

$$\mu = \frac{1}{N} \sum_{i=1}^N c(i), \quad \sigma^2 = \frac{1}{N-1} \sum_{i=1}^N [c(i) - \mu]^2 .$$

We then compare the obtained sound speeds to references values reported by the manufacturer. Table 6.1 summarizes these results.

In most cases, the reconstructed sound speed values are very similar, especially within the error of the measurements, and close to the reference values. However, there was a significant lapse in time between the creation of the phantom and its scanning using our older ultrasound tomography unit. It is likely that the phantom degraded over that time. Thus, the reference values are not reliable estimates of the true sound speed of the phantom at the time of scanning. What is of importance is the trend in sound speed. For example, the large tumor should have greater sound speed than the small tumor. We can see that both the waveform and travel time methods agree with these trends. The recovered sound speed

of the small tumor and fat deposit is most problematic. Due to their small size, we approach the resolution limitations of waveform tomography when the highest reconstructed frequency is 1 MHz. Due to volume averaging effects and convergence issues, the reconstructed sound speeds of the lesions are averaged with the adjacent glandular tissue leading to skewed sound speed values. By looking at the values in Table 6.1, we see that the waveform reconstructions have significant variance in the reported sound speed values. This could be reduced and smoothed by incorporating a regularization penalty to the cost function. For example, a Tikhonov penalty would help balance data fitting and image roughness by prohibiting updates which significantly change the sound speed [95].

6.1.2 Artifacts

Artifacts are present in both the travel time and waveform reconstruction. The most significant artifact in the travel time sound speed images are streaks or ray artifacts arising around regions of higher tissue contrast. This is seen to some degree in the phantom reconstruction in Figure 6.1(a), but are more clearly seen in the *in vivo* reconstructions in Figures 6.2 and 6.3 (top row). The ray artifacts are distracting because they mask the true morphology contained in the margins of the tumor. Morphological information can aid in the assessment of the presence of one breast structure over another (i.e. parenchyma or tumor) or relative risk (i.e. malignant or benign).

The waveform results contain other artifacts. These arise from the hardware, phase matching, and the accuracy of the starting model. The waveform images reconstructed by the older prototype have significantly more artifacts than the newer prototype due to bad transducer elements whose corrupted data is discarded by the calibration process. These are readily seen within the regions corresponding to water in Figures 6.2 and 6.3 (bottom rows). This can lead to problems in imaging the skin contour of the breast. Due to poor signal quality, other problems exist near the chest wall or when the imaging ring is filled to capacity. Also, the presence of more signal energy at 400 kHz and the different acquisition hardware alters the overall perception of the old prototype images. A phase mismatch also

results in artifacts within the reconstructed image. For example, the waveform phantom image in Figure 6.1(b) contains aberrations which look like false contours or clouds on the outer portions of the cascading skin layer (11, 1, and 6 o'clock positions). They arise from a phase offset induced on the reconstructed wavelets. This phase mismatch occurs as a result of the impedance mismatch between the water and the outer skin layer of the tissue mimicking breast phantom and the finite vertical dimension of the ultrasound transducer which confuses the origins of received signals from the sloping edges of the insonified object. The false contours of rapidly sloping objects is proportional to the degree of sloping and is worst near the nipple of the breast. Problems pertaining to the imaging of the outer skin is not as important as the success of imaging clinically relevant features (tumors, cysts, parenchyma, etc.) which are better resolved by using the waveform technique. Ray artifacts inherited from the travel time starting model also corrupt the waveform images. An example is seen in Figure 6.2(a). This issue will be addressed in future work.

6.1.3 In Vivo Results

The usefulness of the waveform tomography method is most clearly seen in the improvements made in imaging the sound speed of *in vivo* structures. To highlight the robustness of the method, we present images reconstructed from data acquired by both the old and new ultrasound tomography units. These reconstructions include examples of the bulk breast tissue and parenchyma, small tumors, and large tumors. Note that each reconstructed image corresponds uniquely to a different patient. We also demonstrate the accuracy of our *in vivo* sound speed reconstructions by imaging a saline breast implant with known sound speed. In section 6.2, we show the validity of our waveform tomography method by demonstrating concordant findings with MRI.

Morphological Comparison

The sound speed reconstructions of data recorded by the older prototype are shown in Figure 6.2. The top row corresponds to the travel time reconstruction method while

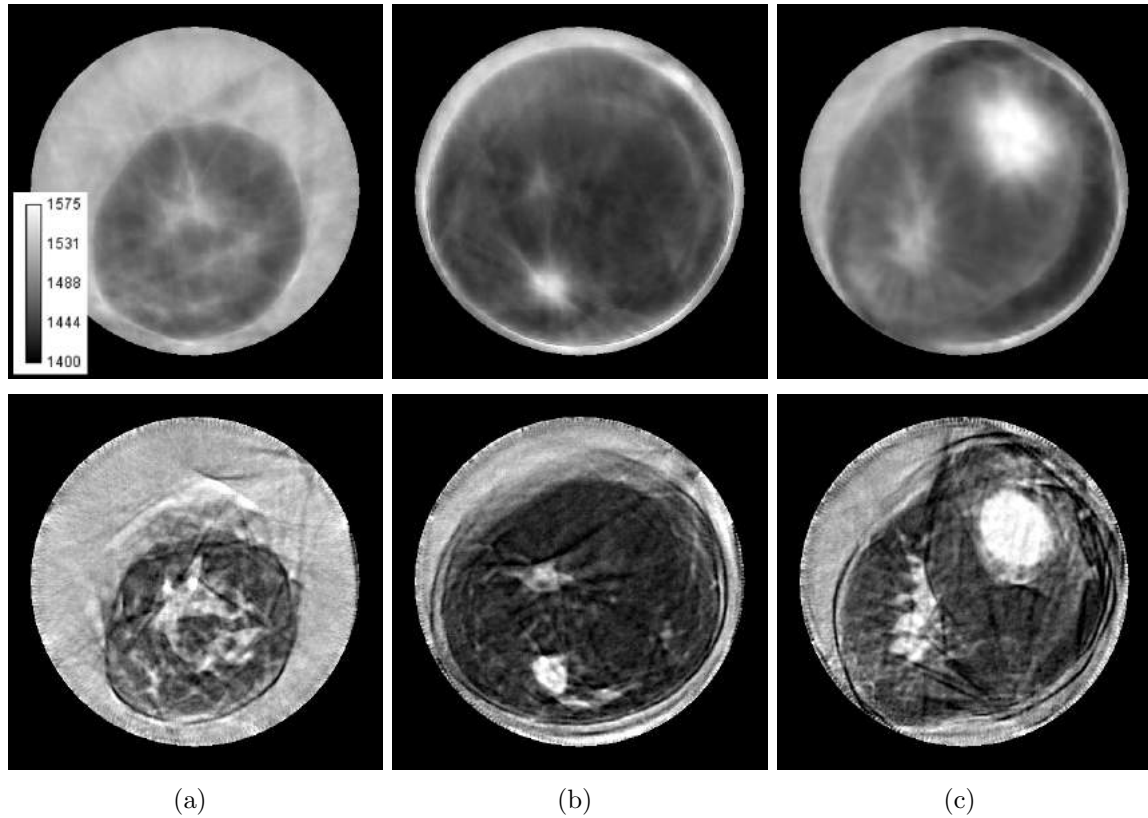


Figure 6.2: Comparison of Travel Time (top row) and Waveform (bottom row) Reconstruction Methods. Data acquired using older ultrasound tomography unit. Gray scale values in the sound speed images correspond to a range of 1400–1575 m/s. Brighter areas correspond to higher sound speed. (a) Complex parenchyma shape. (b) 1.5 cm tumor. (c) 4 cm tumor (1 o'clock) and parenchyma (9 o'clock).

the bottom corresponds to the waveform method. In Figure 6.2(a), we see an example of parenchymal tissue (white) embedded in fat (black). Improvements are made with the waveform reconstruction (bottom row). The cascading layers of the parenchymal tissue are revealed with great clarity in the waveform image where only a fuzzy image marred with ray artifacts is revealed by the travel time reconstruction method (top row). In addition, ray artifacts are clearly seen in the travel time reconstructions. In Figures 6.2(b) and 6.2(c), we see examples of a smaller (approx. 1.5 cm at 6 o'clock) and larger (approx. 4 cm at 1 o'clock) tumors, respectively. As stated before, many structures in the breast can be uniquely identified by their sound speed. However, when dealing with structures with similar sound speed, the improvements made in the delineating the margins of unknown breast structures are of utmost importance [26]. These margins facilitate the differentiation of parenchyma

and other breast structures from malignant and benign masses. The improvements made with the waveform reconstruction allows an observer to better classify the unknown lesions as tumors when, for example, an identification of parenchyma might have resulted from the travel time reconstruction image.

One problem present in these reconstructions is the accurate delineation of the outer contour of the breast. For example, by comparing the waveform and travel time images in Figures 6.2(b) and 6.2(c), one can see that there is some discrepancy in the imaging of the boundary of the breast. This is most problematic as we reach the chest wall, regions where the breast rapidly slopes, or regions where fat/skin folds enter the field of view of the scanner. By comparing to our B-mode reflection images, it is seen that the contours produced by the waveform tomography are more accurate than the travel time tomography.

The sound speed reconstructions of data recorded by the newer prototype is shown in Figure 6.3. In Figure 6.3(a), we see another example of breast parenchyma. Unlike the big cascading layers in Figure 6.2(a), Figure 6.3(a) shows a patient with very fine parenchymal strands. When compared to the travel time tomography reconstruction in Figure 6.3, which only has a faint hint of some of these detailed structure, the delineation of these fine strands is a testament to the resolving power of waveform tomography. In Figures 6.3(b) and 6.3(c), we see examples of a smaller (approx. 1 cm at 9 o'clock) and larger (approx. 4 cm at 3 o'clock) tumors, respectively. As was stated before, a proper reconstruction of the margins of a tumors aids in the best identification of unknown masses. Note the very fine structures resolved in all the cases shown in Figure 6.3.

Quantitative Comparison

From Figures 6.2 and 6.3, it can be seen that the sound speed of waveform reconstructions tend to be lower in fatty regions while being accentuated in tumors and parenchyma. As in section 6.1.1, this can partially be explained by volume averaging effects and convergence issues. An explicit comparison of waveform and travel time sound speeds is shown in Figure 6.4 where a vertical line profile has been taken through the tumor in 6.3(c). From the

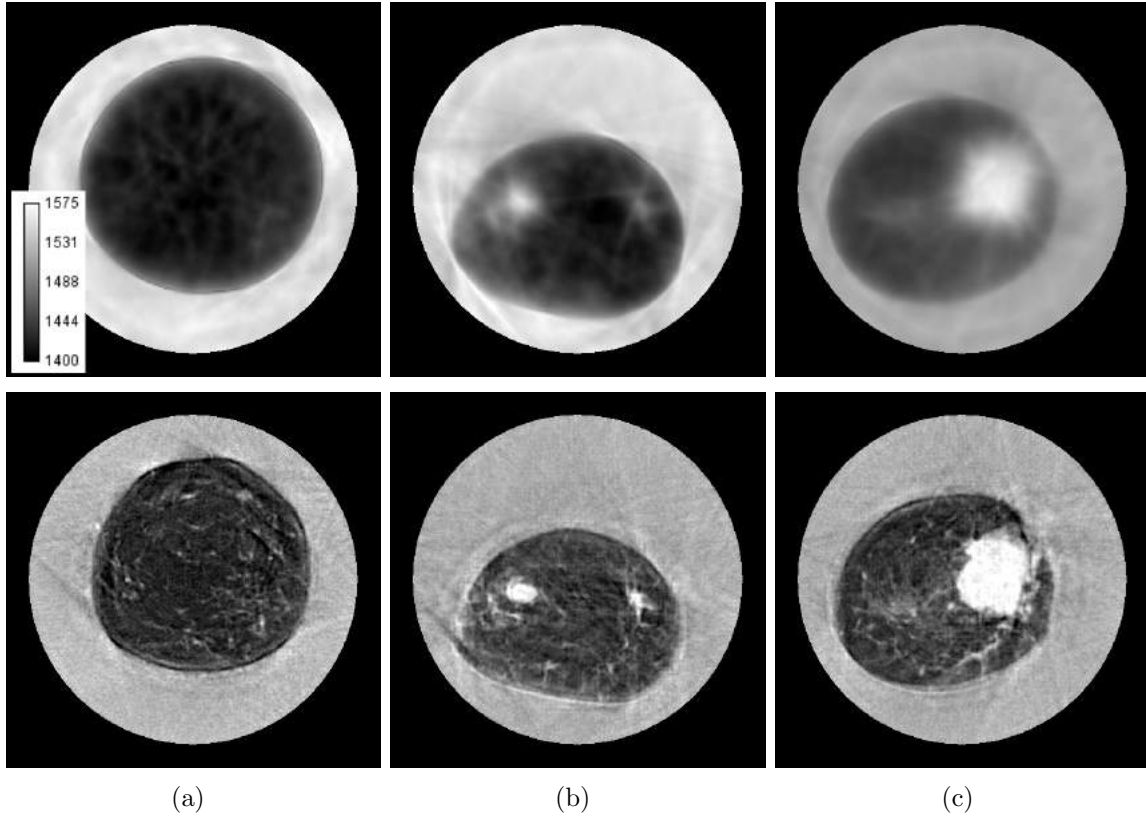


Figure 6.3: Comparison of Travel Time (top row) and Waveform (bottom row) Reconstruction Methods. Data acquired using newer ultrasound tomography unit. Gray scale values in the sound speed images correspond to a range of 1400–1575 m/s. Brighter areas correspond to higher sound speed. (a) Very fine parenchyma patterns. (b) 1 cm tumor (10 o'clock). (c) 4 cm tumor (3 o'clock).

profiles, it can be seen that travel time tomography tends to overestimate fat sound speeds while underestimating tumor sound speeds. In addition, the improvements in resolution are apparent through the increased sharpness of the edge response of the line profiles. In section 6.1.1, we presented quantitative sound speed measurements for a tissue mimicking phantom. We demonstrate the *in vivo* accuracy of quantitative sound speed measurements by imaging a saline breast implant as shown in Figure 6.5. Saline breast implants contain an outer silicone shell filled with a sterile saline solution [105]. Typical saline is composed of 0.9% NaCl solution. Using an empirical formula [106], we calculated the sound speed of the saline implant assuming a body temperature of 37 °C, a salinity of 0.9%, and a pressure of 1 atm to predict a sound speed of 1535 m/s. Drawing a 25 mm radius circular ROI within the center of the implant gives an average sound speed μ with error σ of 1533 ± 3 m/s and

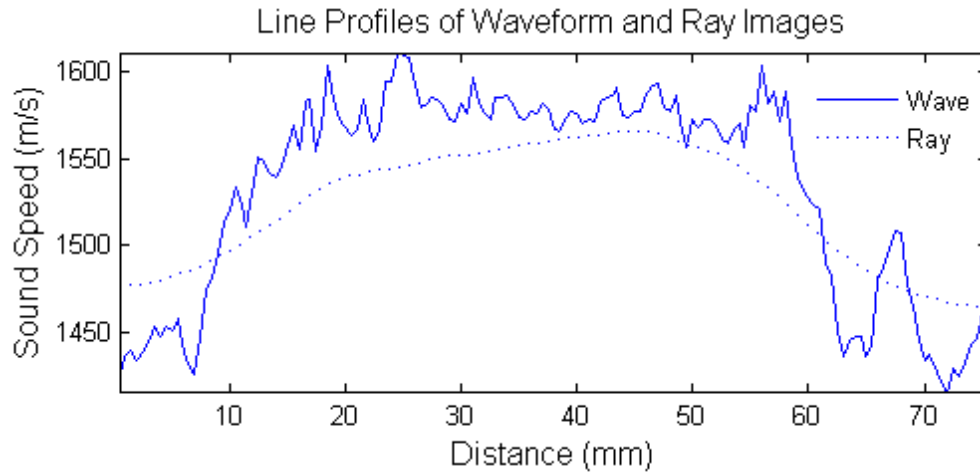


Figure 6.4: Vertical Line Profile Through the Tumor in Figure 6.3(c)

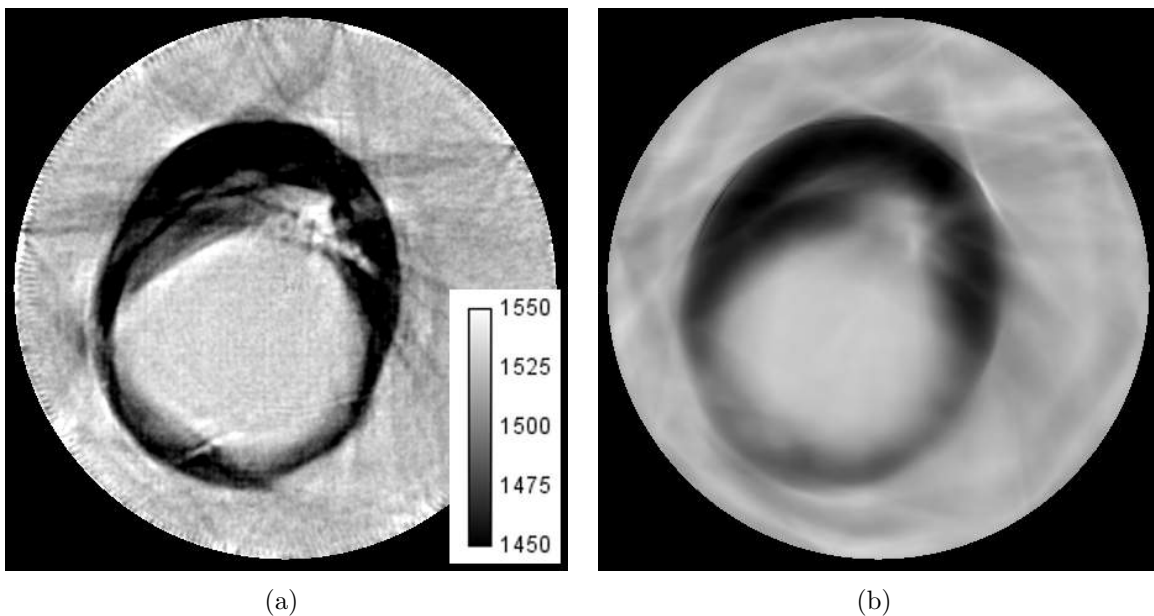


Figure 6.5: Saline Breast Implant Reconstructions. Gray scale values in the sound speed images correspond to a range of 1450–1550 m/s. Brighter areas correspond to higher sound speed. (a) Waveform tomography method. (b) Travel time tomography method.

1528 ± 1 m/s for waveform and travel time reconstructions, respectively. Thus, we see that sound speed of the breast implant is fairly uniform across measurements from three different modalities. This should give some verification to the quantitative capabilities of waveform tomography sound speed imaging and clear up some of the inconsistencies in the measured sound speed values reported in section 6.1.1.

6.2 Comparison to MRI

In this section, we present a comparison of waveform tomography sound speed images to MRI. We will show examples of data gathered by both ultrasound tomography prototypes. We compared our waveform tomograms with MRI (Figures 6.6 and 6.7 for data obtained by the old prototype; Figures 6.8 and 6.9 for data obtained by the new prototype). For the images in Figures 6.6, 6.7, 6.8, and 6.9, arrows mark some of the corresponding areas. Note that it is difficult to perfectly register the images created by both modalities. Aside from typical registration problems, it is particularly difficult in this case because the coronal slices of the waveform tomography images are at an angle with respect to MRI due to the differences in the positioning of the breast in the acquisition process. In particular, the breast is suspended in water during acquisition by our tomographic ultrasound unit. Thus, in order to identify structures that are present in one slice of the waveform tomography image, several slices of the MRI reconstruction may be needed. Likewise, several waveform tomography images might be needed to register a single MR image. Also, waveform tomography sound speed images corresponding to the new system had their the gray scale values inverted to improve visualization and comparison with the T1 weighted MRI sequence that was used. Thus, for these images, darker areas correspond to regions of higher sound speed. For the older system, no such inversion was made as the MRI sequences that were used were T1 weighted gadolinium enhanced fat suppressed sequences. For these sequences, regions such as parenchyma or tumors, which prefer to uptake gadolinium, are bright as in the original gray scale convention of waveform tomography sound speed images. MRI breast images were also resampled from their original transverse orientation and projected into the coronal plane to match the orientation of waveform tomography.

In Figure 6.6(a), a large tumor is present at 1 o'clock. The shape and margins of the tumor are well reconstructed by waveform tomography. Hints of the central necrosis of the tumor are also present in the waveform tomography reconstruction (Figure 6.6(a)). Some of the filamentary structure of the tumor is discernible. For example, the small strand at

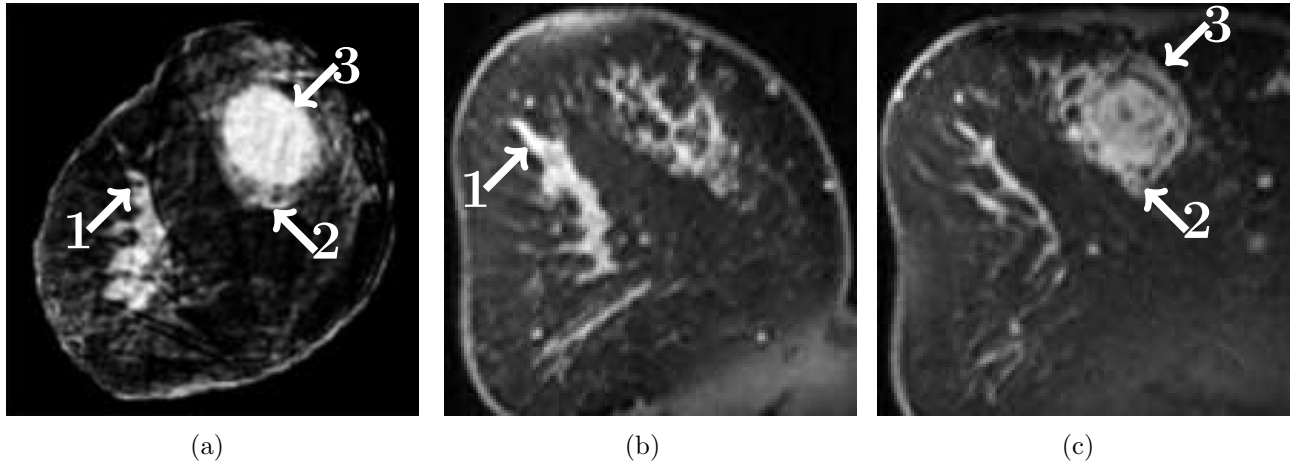


Figure 6.6: Comparison of Waveform Tomography Reconstruction to MRI. Combinations of numbers and arrows indicate the corresponding tissues for comparison. Data was acquired by the old prototype. (a) Waveform sound speed; (b) MR slice with corresponding parenchyma; (c) MR slice with corresponding tumor.

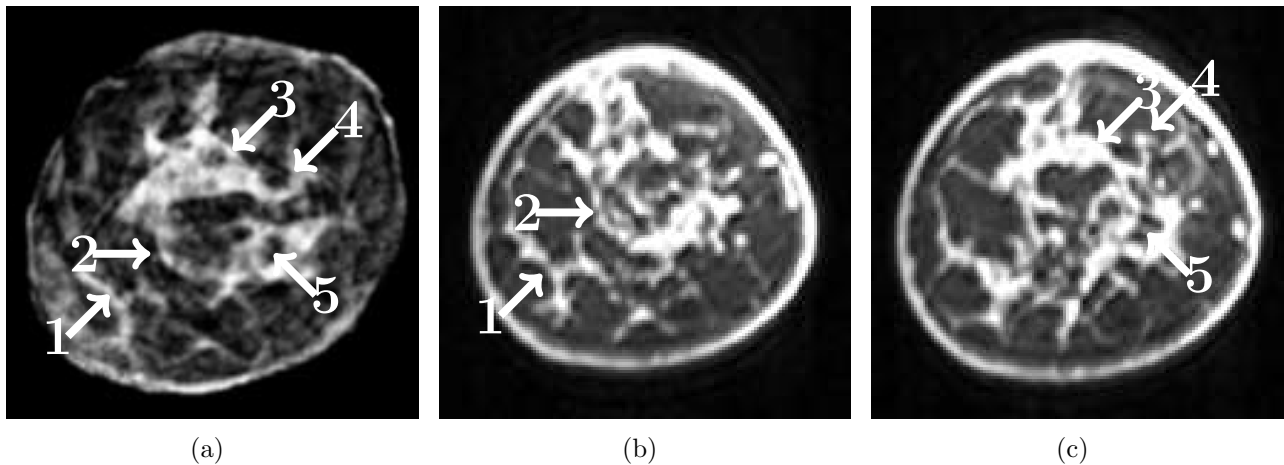


Figure 6.7: Comparison of Waveform Tomography Reconstruction to MRI. Combinations of numbers and arrows indicate the corresponding tissues for comparison. Data was acquired by the old prototype. (a) Waveform sound speed; (b) and (c) Corresponding MRI slices.

the inferior portion of the tumor is present in both Figures 6.6(a) and 6.6(c). In addition, the shape of the dense tissue structures at 8 o'clock in Figure 6.6(a) matches well with that of MRI in Figure 6.6(b). In Figure 6.7, the waveform inversion (Figure 6.7(a)) of breast parenchyma is compared to MRI (Figures 6.7(b) and 6.7(c)). The overall shape of the parenchyma matches very well. In Figures 6.8(a) and 6.8(b), the waveform inversion reveals a small tumor at 10 o'clock. Both the tumor and filamentary structures match very well

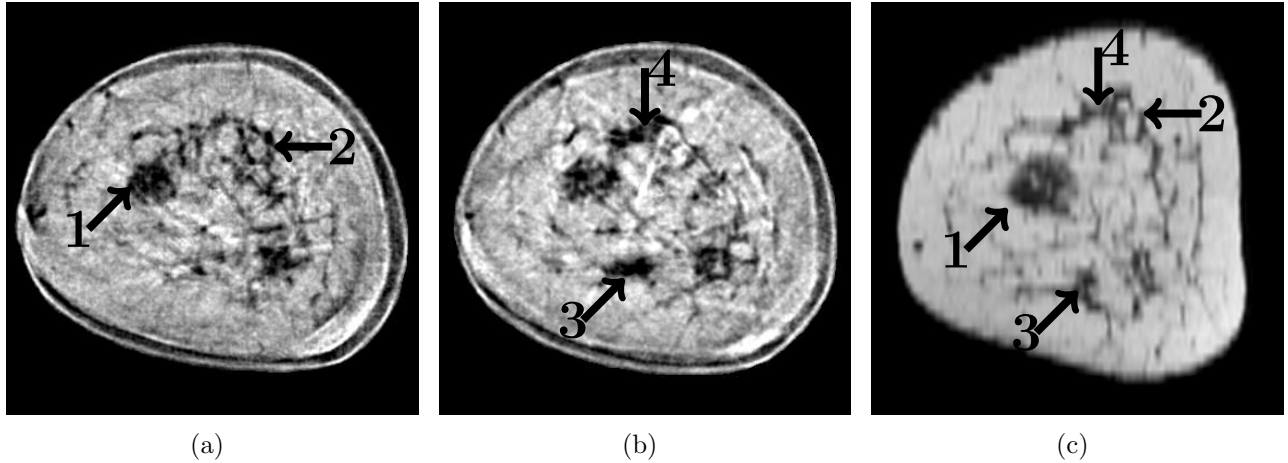


Figure 6.8: Comparison of Waveform Tomography Reconstruction to MRI. Combinations of numbers and arrows indicate the corresponding tissues for comparison. Data was acquired by the new prototype. Gray scale values of the waveform tomography image have been inverted to better match the MR image. (a) Waveform sound speed; (b) Waveform sound speed; (c) MR slice with corresponding tumor and parenchyma.

with MRI in Figure 6.8(c). In Figure 6.9, very fine parenchymal structures are imaged in a very similar fashion by both waveform tomography and MRI. Overall, there is a great deal of concordance between our preliminary waveform tomography sound speed images and the well established modality of MRI. Morphological comparison of the shape of complex parenchyma and other breast features verifies the capabilities of waveform tomography to image real structures. The high quality images obtained by reconstructing both data sets highlights the robustness of the algorithm. Note that some of these patients were scanned by the older system while others were scanned by the new system. Images were manually masked to highlight the comparison of breast tissue. As a conclusion to this section, in Figure 6.10 we give more examples of the fine parenchymal breast structures shown in Figure 6.9.

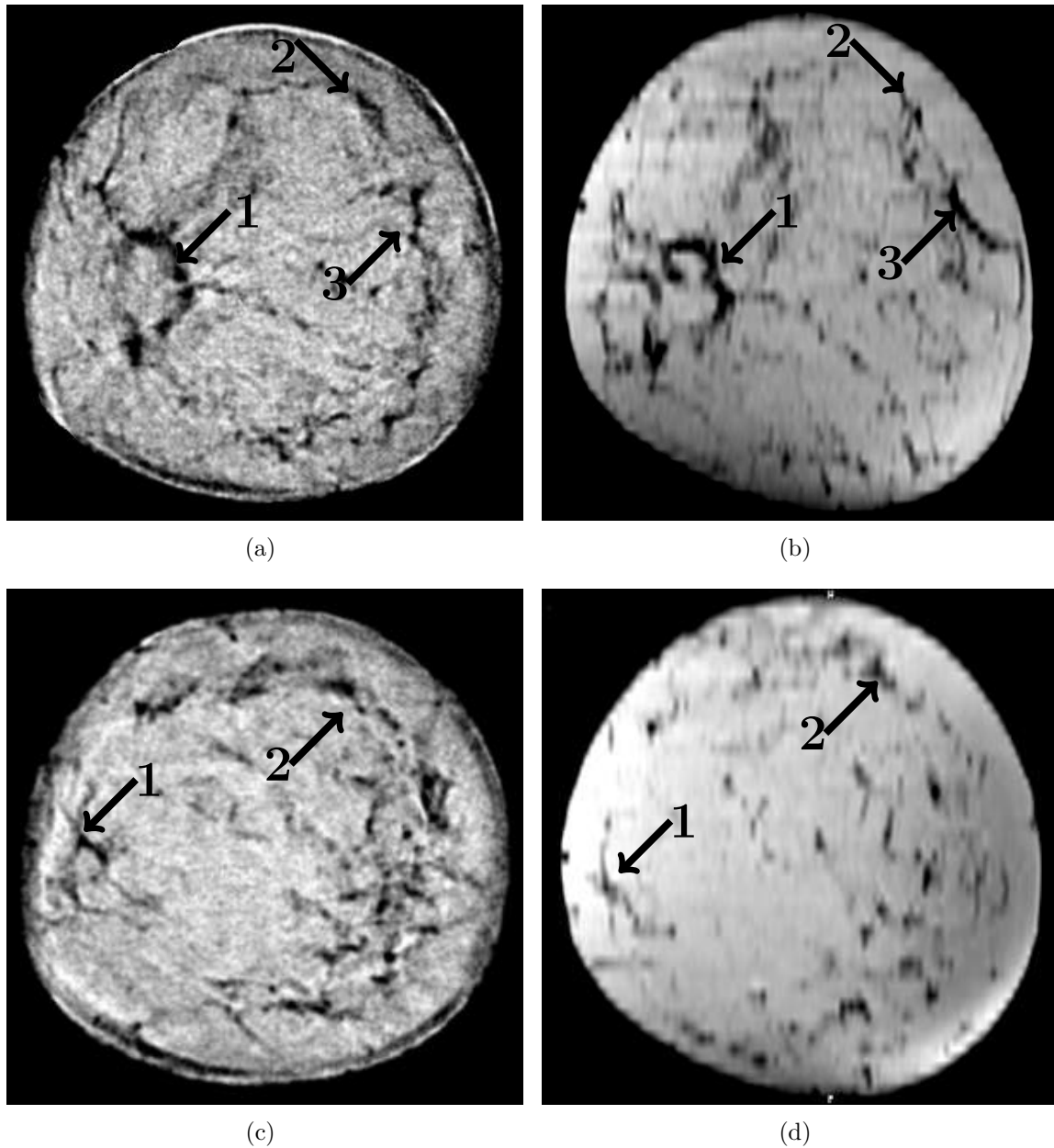
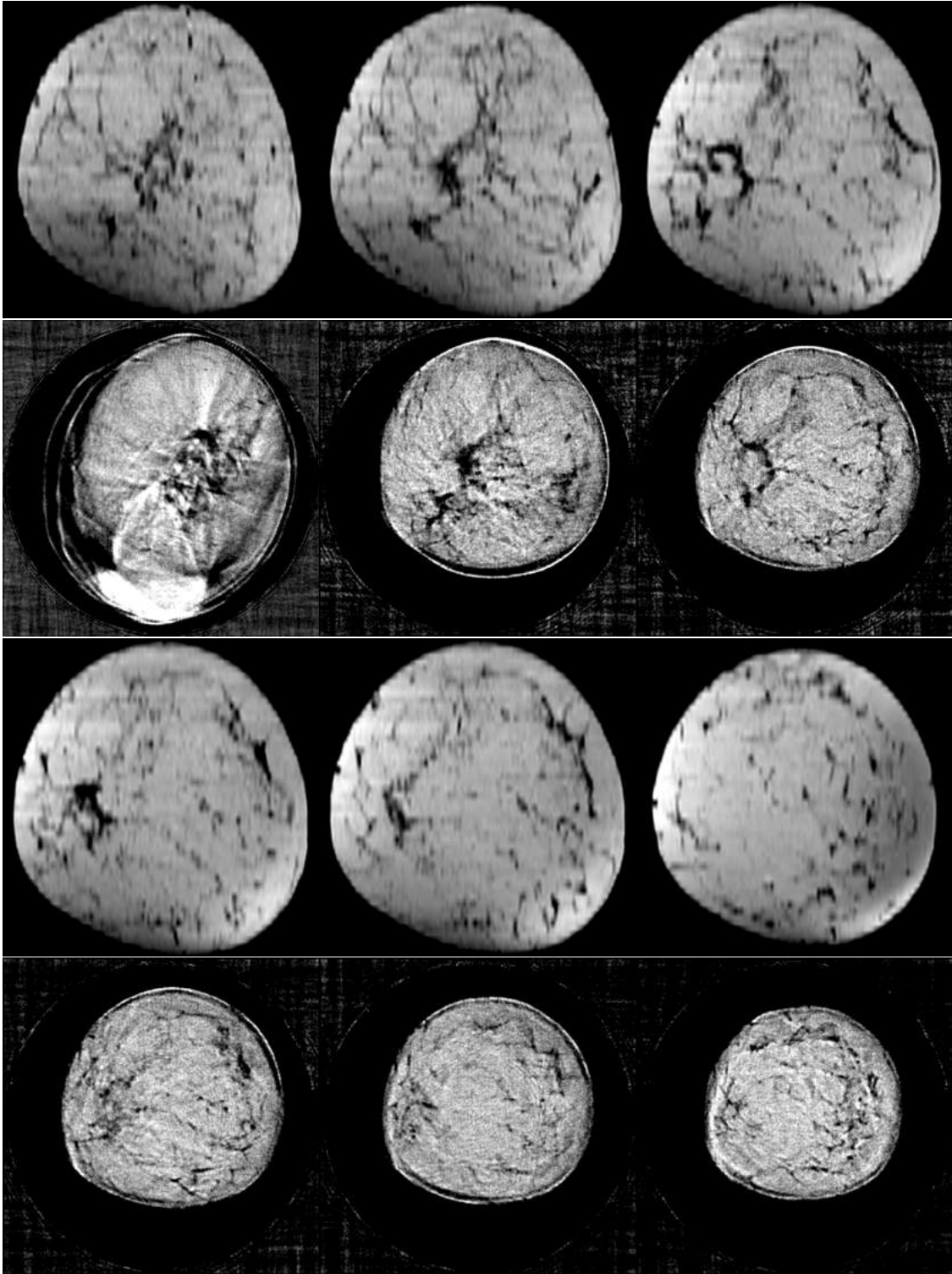


Figure 6.9: Comparison of Waveform Tomography Reconstruction to MRI. Combinations of numbers and arrows indicate the corresponding tissues for comparison. Data was acquired by the new prototype. Gray scale values of the waveform tomography image have been inverted to better match the MR image. (a) Waveform sound speed; (b) Corresponding MRI slice; (c) Waveform sound speed; (d) Corresponding MRI slice.



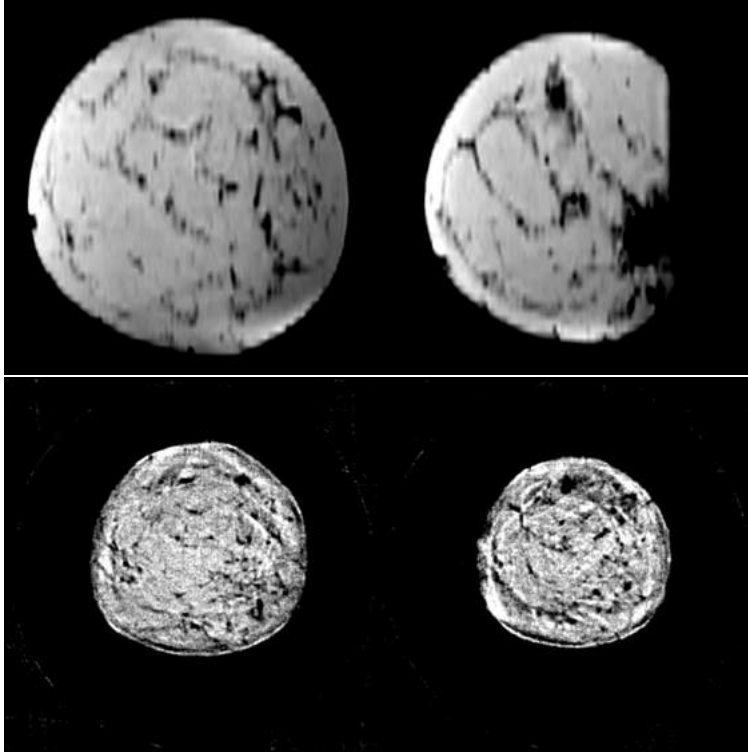


Figure 6.10: Series of MR and Waveform Tomography Sound Speed Images. Images consist of alternating rows of MR images and waveform sound speed images. Each vertical pair of MR and sound speed images correspond to approximately the same location in the patient.

CHAPTER 7: Clinical Use

A major motivation for pursuing the waveform sound speed imaging method is the hope that it would be useful in a clinical setting. Having demonstrated the capabilities of the waveform algorithm to accurately obtain morphological and quantitative sound speed information, we assess its performance in a clinical setting by following the work-up of different patients who were eventually diagnosed with either malignant or benign breast diseases. We present summaries of the clinical reports used to diagnosis the patient and where appropriate and available, the corresponding mammograms, hand-held ultrasound (HHUS) scans, MR scans, waveform tomography sound speed images, and tomographic reflection images. We surmise the possible role that waveform tomography would have in screening and diagnosing a patient given our limited experimentation. Note that we will not evaluate the use of attenuation in these clinical cases. However, reliable and accurate attenuation measurements should aid in the specificity of ultrasound tomography breast examinations. In Figure 7.1, we see the definition of the anatomic planes [107] as well as other terminology associated with anatomic locations in medicine [108, 109]. We will also make use of some of the lexicon used to describe tumors as given in [14, 26].

7.1 Methods

7.1.1 Patient Selection

In an ongoing HIPAA compliant and IRB approved clinical study, 300 women were scanned by an ultrasound tomography device to further evaluate masses that were previously detected and diagnosed by biopsy, MRI, mammography, and/or standard ultrasound. Data obtained from a subset of 11 women was used in this study. Patients were chosen based on confirmed breast masses. The patient data included 4 cancers, 8 fibroadenomas, and 7 cysts. The ultrasound waveform tomography (USWT) method allowed visualization of

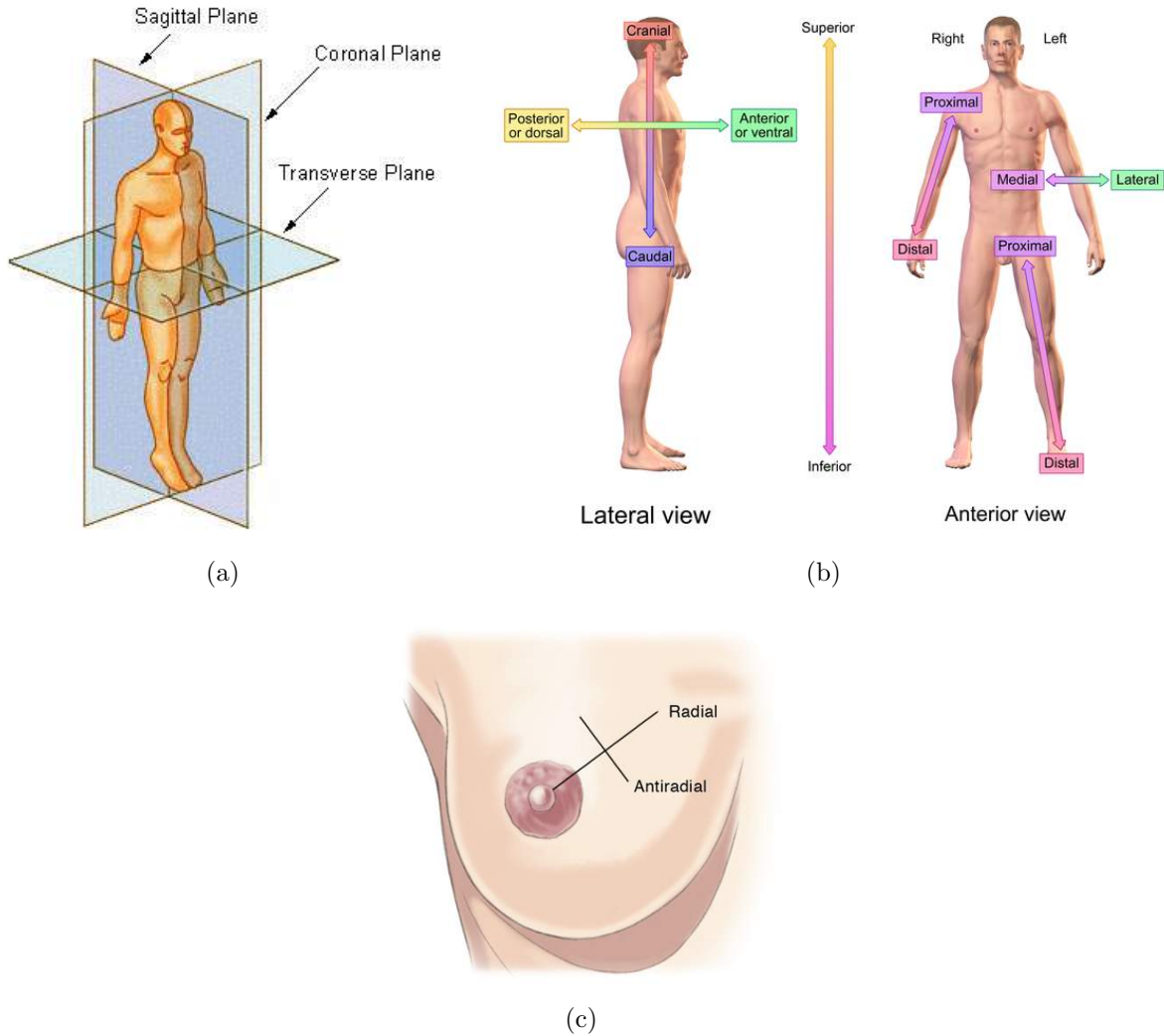


Figure 7.1: Directional References. Schematic of body planes and commonly used terminology to describe anatomic location.

breast anatomy including normal fibroglandular tissue of varying density, benign tumors such as cysts and fibroadenomas, and malignant tumors of varying sizes. Area analysis compared the size of tumors across different modalities. Quantitative analysis of the sound speed imaging technique is also presented.

7.1.2 Quantitative Sound Speed Analysis

In order to determine the sound speed of a tumor or other breast tissue, a region of interest (ROI) was drawn in our USWT sound speed images around what was visually determined to be the margin of the tumor/tissues. The mean sound speed μ in the ROI is given by the

mean sound speed of all N pixels corresponding to the ROI

$$\mu = \frac{1}{N} \sum_{i=1}^N c_i.$$

The error in the measurement is given by the standard deviation of the sound speed values in the ROI

$$\sigma = \sqrt{\frac{1}{N-1} \sum_{i=1}^N (c_i - \mu)^2}.$$

When multiple measurements from different lesions were averaged, the error is given by the propagation of the individual errors in addition to the standard deviation of the averaged values.

For tumors that were difficult to detect or determine the extent of their margins, B-mode UST images served as a guide for ROI selection. The sound speed of fibroglandular regions were determined by selecting ROIs around regions of fibroglandular tissue surrounding the tumor location in order to determine the background parenchymal enhancement of the tumor. The sound speed of fatty regions was determined by placing a circular ROI in that region while taking special care to avoid as much fibro-glandular tissue as possible.

After obtaining mean sound speed values for various lesions, it was useful to window and level the grayscale of the sound speed image to correspond to the mean sound speed of the lesion. For example, for the evaluation of fibroadenomas in one of the clinical case examples, windowing and leveling the sound speed image to a range consistent with the sound speed of fibroadenomas might help an observer locate other similar lesions. In addition, when the grayscale is limited to a narrower window, variations in the sound speed are more readily apparent. For example, this might help in the imaging of necrotic tissue within a tumor.

7.1.3 Qualitative and Area Comparison to Other Imaging Modalities

USWT sound speed images were compared to other imaging modalities in order to establish concordant findings and to compare the manner in which the breast tissue image was

reconstructed and displayed. USWT sound speed images were compared to HHUS, mammography, both T1 weighted and T1 weighted gadolinium enhanced fat suppressed MRI images, UST B-mode reflection images, and UST travel time sound speed images. Note that it was difficult to perfectly register images across different modalities.

For the case of MRI comparison, MRI images were converted from their native axial orientation and resampled in the coronal plane to match the orientation of USWT. A breast was freely suspended in air during MRI acquisition while a breast was submerged in water during an UST tomography scan acquired by our clinical prototype. The effects of gravity and buoyancy then distorted the visualization of the breast. Thus, in order to register breast architecture between MRI and USWT, multiple slices of either modality were needed to see breast features present in the other modality. A problem with the grayscale values of the USWT sound speed images arose when comparing to T1 weighted MRI. Areas of higher sound speed such as breast fibroglandular tissue and tumors were bright due to our original grayscale convention. In T1 weighted MRI, these regions were dark. Thus, we found the best solution that maximizes image quality for both modalities was to invert the grayscale of the USWT sound speed images such that darker/brighter areas corresponded to higher/lower sound speed. Note that this problem did not exist when comparing USWT sound speed to T1 weighted contrast enhanced fat suppressed MRI sequences as areas such as tumors and fibro-glandular tissue were brighter after contrast enhancement and fat suppression.

Comparison to HHUS and mammography was done by matching features present in both modalities with patient reports and the USWT sound speed image. Comparison to UST reflection B-mode images and travel time sound speed images were done by comparing the image slices corresponding to both modalities. We also performed area analysis to compare the size of tumors across different modalities. This analysis was done by determining the area of an ellipsoid as given by the length, width, and/or heights measurements of the imaged lesions across the different modalities.

Type.	Average (m/s).	Maximum (m/s).	Minimum (m/s).	Average Background Enhancement (m/s).
Cancer	1542 ± 42	1568 ± 22	1506 ± 18	59 ± 35
Fibroadenoma	1583 ± 19	1600 ± 19	1569 ± 18	48 ± 20
Cyst	1561 ± 25	1591 ± 15	1535 ± 22	54 ± 10
Fat	1439 ± 20	1460 ± 18	1403 ± 33	-71 ± 31

Table 7.1: Sound Speed Analysis of Various Tissue Types. The average background enhancement is with respect to the surrounding fibroglandular tissues.

7.1.4 Clinical Application

The clinical application of the USWT sound speed imaging method was determined by reviewing the case reports of different patients. We will present an in-depth analysis for 5 of the 11 patients used in this study. These cases included a combination of younger and older women with varying breast densities and varying lesion types including cysts, fibroadenomas, and cancers. We compared the original purpose of breast evaluation (i.e. palpable lumps, routine mammogram), the outcome of the evaluation (i.e. mammography occult but visible via HHUS), patient age, and breast density to the ability of the various imaging modalities to properly diagnose the patient. We then assessed what role USWT might play in this workflow and how the morphological and quantitative information provided by USWT might change or improve diagnostic performance.

7.2 Results and Discussion

7.2.1 Quantitative Sound Speed Analysis

Table 7.1 summaries the quantitative sound speed analysis of cancers, fibroadenomas, cysts, and fat. The reported average background enhancement is with respect to areas of fibroglandular tissue adjacent to the various tissue types. For the tumors, the mean average background enhancement is 53 ± 20 m/s.

The sound speed of fat as reconstructed by USWT agreed with many different studies [32, 33, 34, 35, 46]. The fat sound speed values in these studies ranged from about 1410-1490 m/s.

In particular, [35] reported the sound speed of breast fat to be 1436 ± 18 m/s. The USWT reconstruction of malignant and benign tumor sound speeds both agrees and disagrees with other studies. References [34, 46] reported that the sound speed of cancers are generally higher than benign tumors. For example, [34] gave an average cancer and fibroadenoma sound speed of 1531 ± 36 m/s and 1500 ± 27 m/s, respectively, while [46] which used our previous travel timetomography sound speed imaging method, gave an average cancer and benign tumor sound speeds of 1548 ± 27 m/s and 1513 ± 27 m/s. Our USWT results showed that fibroadenomas and cysts tend to have a higher relative sound speed while cancers ranged from about 1500-1570 m/s. This agrees with [33] which reported cancers with a sound speed range of 1470-1610 m/s and fibroadenomas with a sound speed range of 1560-1600 m/s. It also agreed with [32] which reported a cancer sound speed range of 1465-1573 m/s. In particular, [35] gave cancer, fibroadenoma, and cyst sound speeds of 1550 ± 35 m/s, 1584 ± 27 m/s, and 1568 ± 40 m/s. Thus, we conclude that the sound speed of fat, to be conservative, is at least below 1500 m/s. In addition, tumor sound speeds can have a wide sound speed range.

7.2.2 Case 1 - Small Cancer in Younger Female with Scattered Density (SV029)

A 35-year-old female with a palpable mass and no family history of breast cancer came for her first mammogram. A bilateral diagnostic mammogram and subsequent spot compressions revealed scattered areas of fibroglandular density and a 2.1 circumscribed irregular mass with no architectural distortion. A cranial-caudal mammogram is seen in Figure 7.2(a). The tumor location corresponds to the location of biopsy clip (bright spot in center and lower third of image). Hand-Held ultrasound (HUS) was recommended which revealed an irregular mass with indistinct margins, posterior shadowing, and peripheral vascular flow measuring 2.8 cm x 2.4 cm (length x height in radial plane) and 2.5 cm x 2.4 cm (length x height in anti-radial plane) in size (Figure 7.2(b)). The radial and anti-radial breast planes are shown in Figure 7.1(c). Using the volume of an ellipsoid $V = 4/3\pi lwh$, this give an approximate volume of 70 cm^3 . Ultrasound (US) guided core biopsy and the subsequent

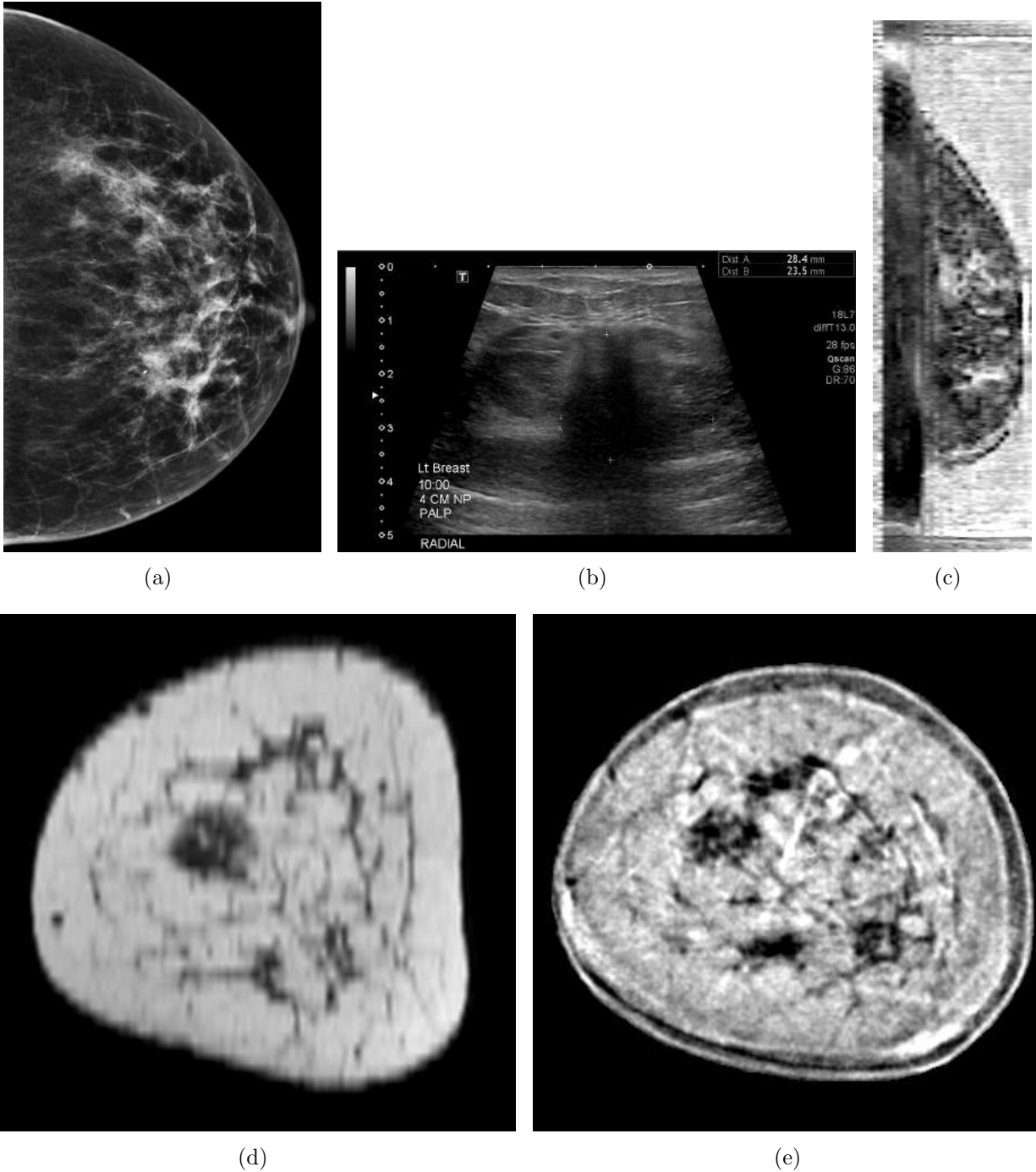


Figure 7.2: Images Corresponding to Case 1. (a) Cranial-Caudal mammogram. (b) Hand-Held ultrasound. (c) Waveform sound speed re-sampled in sagittal plane. (d) MRI. (e) Waveform sound speed with inverted gray scale.

pathology report revealed a poorly differentiated invasive ductal carcinoma. A bilateral MRI examination was performed to reveal a mass indicative of malignancy. Its size is 2.6 cm (TR) x 2.7 cm (AP) x 2.8 cm (CC) (Figure 7.2(d)). The abbreviations TR, AP, and CC mean

“transverse”, “anterior-posterior”, and “cranial-caudal” (see Figure 7.1). The approximate volume would then be 82 cm^3 . The patient was scanned with ultrasound tomography (UST) and ultrasound waveform tomography (USWT) was applied to create a USWT sound speed map of the breast (Figure 7.2(e)). Viewing the USWT image stack reveals a 2.3 cm (TR) x 2.3 cm (AP) x 2.0 cm (CC) tumor with irregular shape and indistinct margins. The approximate volume would then be 44 cm^3 . As in section 6.1.1, mean sound speed values were determined by masking ROIs around the margins of the tumor, the fibroglandular region at 1 o'clock, and the fatty breast region at 7 o'clock. This gave mean sound speed values of $1526 \pm 15 \text{ m/s}$, $1479 \pm 25 \text{ m/s}$, and $1450 \pm 14 \text{ m/s}$, respectively.

The purpose of this example is to demonstrate the capability of USWT to find a small approximately 2 cm cancer in a young 35-year-old female with a palpable mass and no prior family history of breast cancer. The size of the mass implies that it could have been detected prior to palpation if a baseline mammogram and subsequent screening mammograms were available. However, given the age of the woman, regular screening mammography would still not have been recommended for at least another five years [9]. This has important consequences in the screening of at risk dense breasted young women. From the mammogram, it is difficult to make a conclusive diagnosis about the nature of the mass. HHUS was needed to help make this diagnosis without the use of biopsy. Comparison of USWT to T1 weighted MRI reveals a great deal of concordant findings between the two modalities. The shape of the tumor and the branching patterns of the fibroglandular region at 1 o'clock are very similar. The shape of parenchyma at the caudal region of the image is also similar in that both patterns do not show mass effect. Comparison of USWT sound speed to T1 and T1 weighted contrast enhanced fat suppressed MRI implies that areas of higher sound speed have lower T1s since bright areas in the sound speed image correspond to dark areas in the T1 MRI image. Also, areas of higher sound speed tend to absorb more contrast agent since bright areas in the sound speed image correspond to bright areas in the T1 contrast enhanced fat suppressed image. The volume reported by MRI and HHUS agree fairly well.

Due to problems with the anterior-posterior resolution, artifacts near the chest wall (see

Figure 7.2(c)), and the deformation of the breast in water, it is hard to be confident in the concordance of the anterior-posterior extent of the tumor in the waveform image of this patient. However, the measurements in the coronal plane match very well between MRI, HHUS, and USWT.

7.2.3 Case 2 - Multiple Fibroadenomas in Younger Female with Heterogeneous Density (SV162)

A 34-year-old female with multiple bilateral palpable lumps came for a follow up bilateral HHUS examination. Sonographic examination of the both breasts revealed multiple well-defined hypoechoic solid masses with no vascular flow and a sonographic appearance characteristic of benign fibroadenomas (Figure 7.3(a)). The largest mass in the left breast is at the 12:30 position 8 cm from the nipple and measures 2.5 cm x 1.9 cm (length x height in radial plane) and 2.7 cm x 1.9 cm (length x height in anti-radial plane). We approximate an ellipsoid area of $A = \pi lw = \pi \times 2.5 \text{ cm} \times 2.7 \text{ cm} = 21 \text{ cm}^2$. The sonographic characteristics compounded with the fact the lesions have been stable for more than two years is compatible with multiple benign fibroadenomas. Thus, no additional biopsy or imaging procedures were recommended. The patient was then scanned using UST and USWT was applied to create a USWT sound speed map of the breast as seen in Figure 7.3(c). Note that the B-mode reflection image is also shown for comparison in Figure 7.3(b) to highlight the concordant cyst shape. Viewing the USWT image corresponding to the approximate location of the largest mass in the left breast reveals a 3.0 cm (long axis) x 2.4 cm (short axis) tumor with lobular shape and well-defined margins. Volumetric comparison was not done as the entire image stack was not reconstructed. However, the area was determined to be approximately 23 cm². Mean sound speed values were determined by masking ROIs around the margins of the tumor, the surrounding fibroglandular region, and a fatty region of the breast. This gave mean sound speed values of 1570 +/- 19 m/s, 1511 +/- 30 m/s, and 1460 +/- 18 m/s, respectively. In Figure 7.3(d), the windowing and leveling of the grayscale values of the USWT sound speed image is set such that the minimum and maximum sound speed is 1550

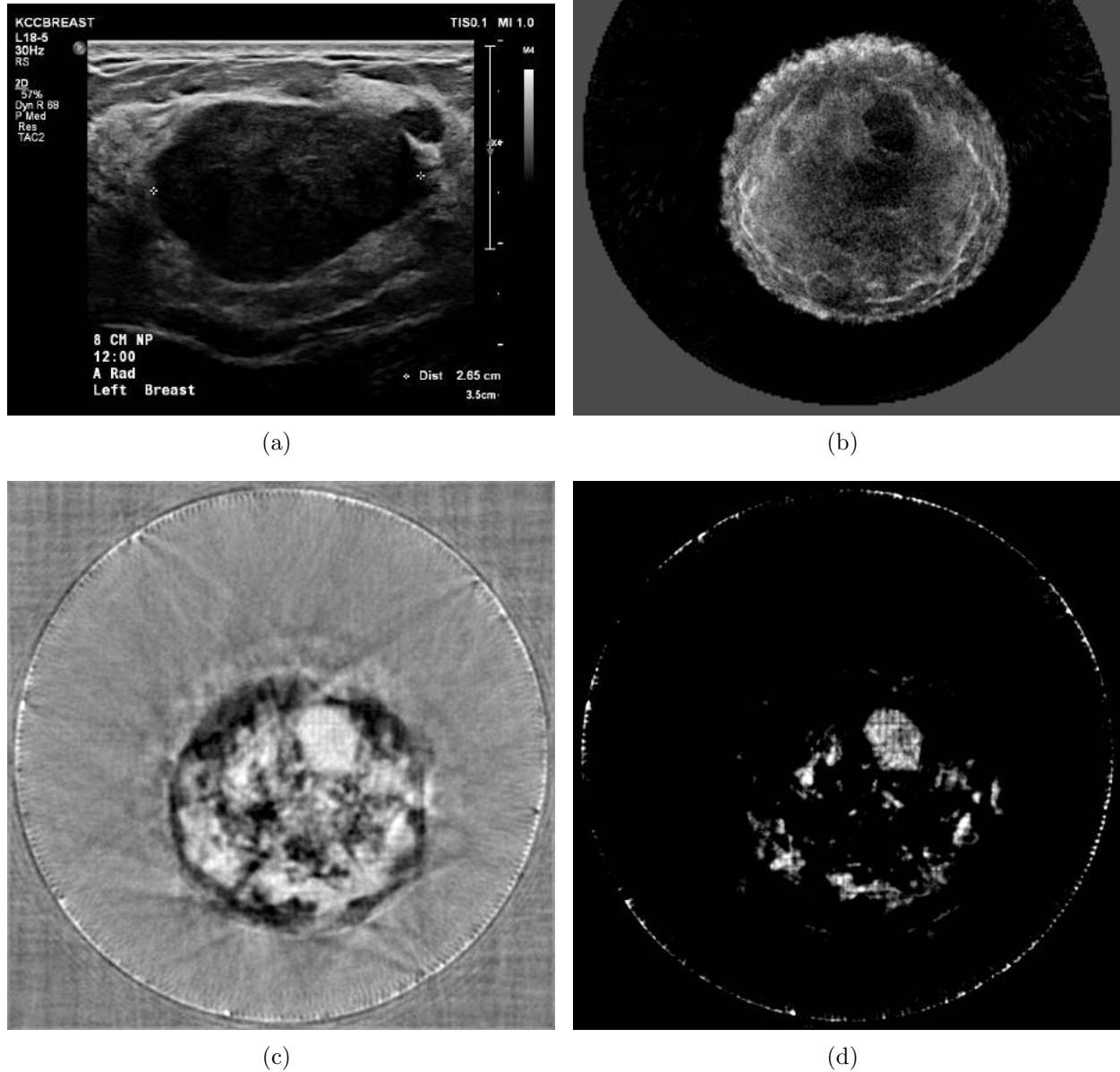


Figure 7.3: Images Corresponding to Case 2. (a) Hand-Held ultrasound. (b) Reflection envelope. (c) Waveform sound speed. (d) Waveform sound speed with preferential window and leveling.

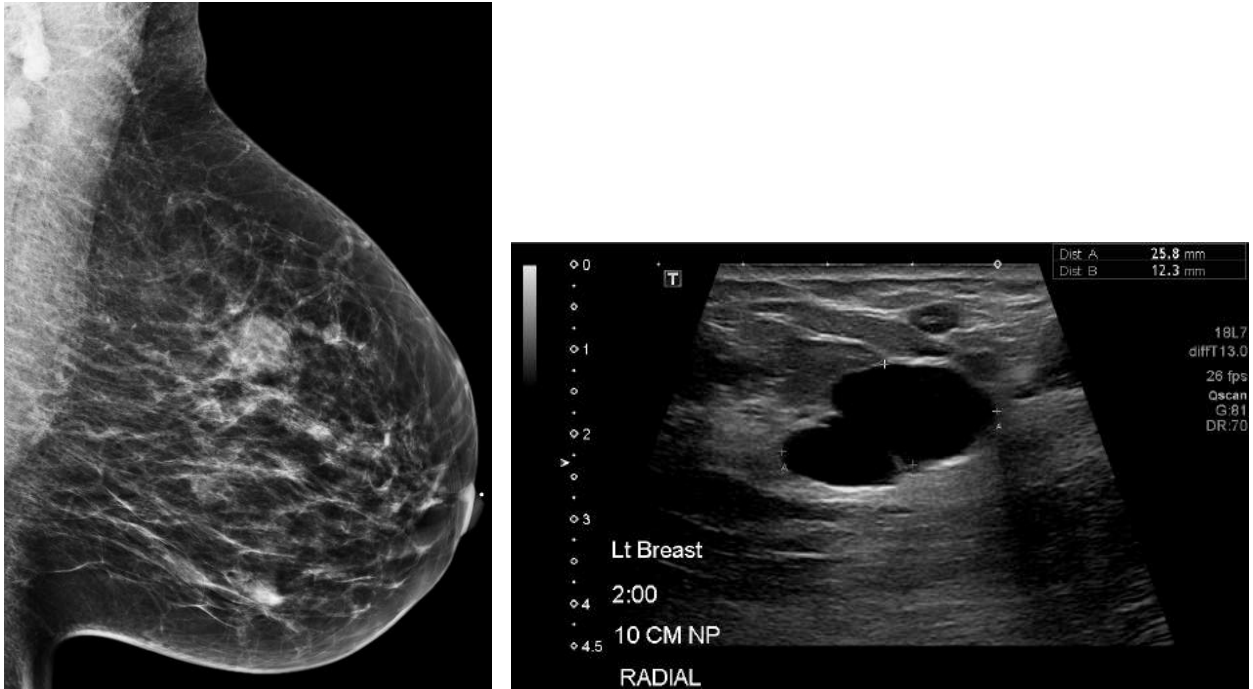
m/s and 1600 m/s.

This example illustrates the ability of USWT to image benign fibroadenomas in a younger 34-year-old female with heterogeneously dense breasts and multiple benign lesions. The shape and margins of the benign tumor are consistent with the appearance of shapes and

margins of tumors as presented in HHUS. The approximate area of the lesion also matches fairly well in HHUS and USWT. The sound speed values of the large fibroadenoma is consistent with the values reported in some studies. By finding a proper window and level setting dependent on the overall sound speed of the breast that is scanned and the type of lesion one is interested in, additional information can be obtained through simple contrast adjustment. By windowing to a range consistent with what might match for particular type of fibroadenoma that has a high sound speed, the shapes of what might be similar lesions are revealed. These regions, to some degree, correspond to the regions of hypoechogenicity in the B-mode reflection image. Thus in line with the patient report, we believe these regions might correspond to additional benign fibroadenomas. Using UST with additional USWT sound speed imaging avoids the ionizing radiation of mammography and could serve to monitor the possible growth of malignancy in patients with dense breasts and a history of benign breast disease.

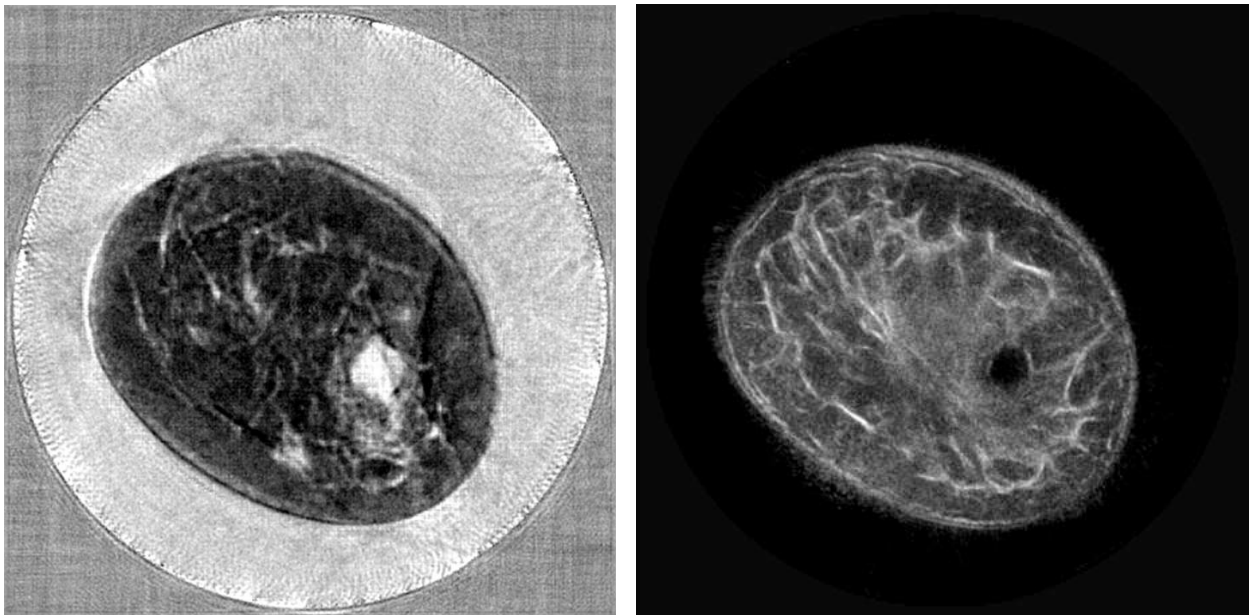
7.2.4 Case 3 - Benign Cyst in Older Female with Scattered Density (SV113)

A 47-year-old female was called back for a diagnostic mammogram (see Figure 7.4(a)) after a suspicious mass was found in a previous visit. Additional spot compression views were obtained and a persistent 3 cm mass was seen. Subsequent HHUS revealed a well-defined anechoic structure with enhanced through transmission and a lack of vascular flow measuring 2.6 cm x 1.2 cm (length x height in radial plane) and 1.7 cm x 1.2 cm (length x height in anti-radial plane) (see Figure 7.4(b)). The HHUS findings were consistent with a benign simple cyst and the lesion area corresponded to the area of mammographic concern. The patient was then scanned using UST and USWT was applied to create a USWT sound speed map of the breast in Figure 7.4(c). Viewing the USWT image reveals a mass at the 4 o'clock position measuring 2.3 cm (long axis) x 1.8 cm (short axis) with lobular shape and well-defined margins. Mean sound speed values were determined by masking ROIs around the margins of the tumor, the fibroglandular region surrounding the tumor, and a fatty portion of the breast. This gave mean sound speed values of 1535 +/- 22 m/s, 1474 +/-



(a)

(b)



(c)

(d)

Figure 7.4: Images Corresponding to Case 3. (a) Mediolateral Oblique Mammogram. (b) Hand-Held ultrasound. (c) Waveform sound speed. (d) Reflection envelope.

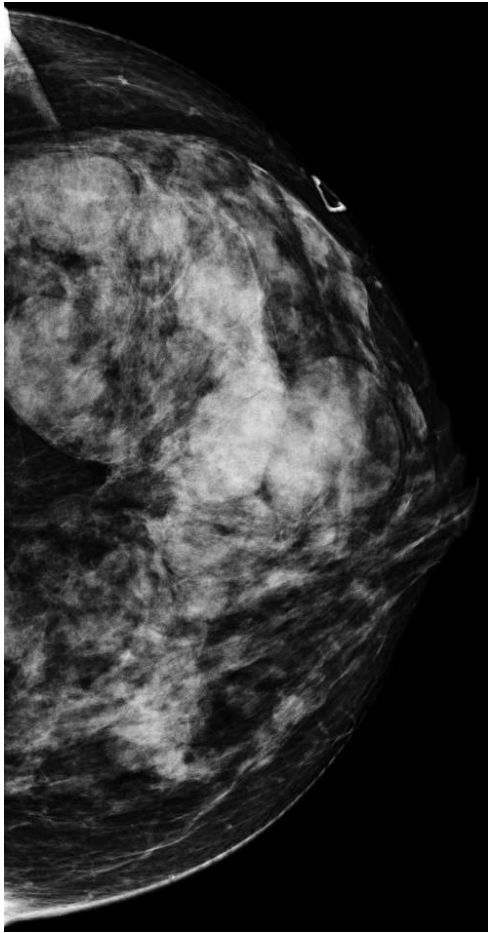
22 m/s, and 1438 \pm 15 m/s, respectively. A reflection envelope image is also shown in Figure 7.4(d) to highlight the concordant shapes of the cyst and to highlight similar fine parenchymal patterns in the breast.

This is an example of a cyst in a breast with scattered fibroglandular density. As was the in the case 1, it is difficult to make a definitive diagnosis based on the mammogram alone. HHUS was needed to help make this diagnosis without the use of biopsy. The shape and margins of the benign cyst matches fairly well across HHUS, USWT, and UST reflection images. The size/area of the tumor is also fairly consistent between HHUS and USWT. Our hope is to use the different imaging capabilities of UST (reflection, sound, attenuation) to make a definite diagnosis of malignant or benign breast disease. Thus, we could avoid the ionizing radiation of mammography and the operator dependence of HHUS. Note that in order to have confidence in the imaging capabilities of any modality, a large data base of reconstructed images from different types of disease and patients are needed. Based on the knowledge gained from studying the database, an observer will be trained to recognize features in an unknown sample.

7.2.5 Case 4 - Benign Cysts in Older Female with Extremely Dense Breasts (SV077)

A 51-year-old female with a history of cysts and bilateral palpating lumps had a bilateral diagnostic mammogram exam as shown in Figure 7.5(a). The breasts were extremely dense which obscures the viewing of mammograms. Circumscribed isodense masses were seen but with little change compared to previous mammograms. No spiculated masses or microcalcifications developed. Areas of palpable concern were marked with triangular shaped fiducial markers. HHUS of the breasts revealed multiple anechoic simple cysts with imperceptible walls, enhanced through transmission, and no internal solid component. An example of what we believe to be the area corresponding to the waveform sound speed image shown in Figure 7.5(c) is seen in Figure 7.5(b).

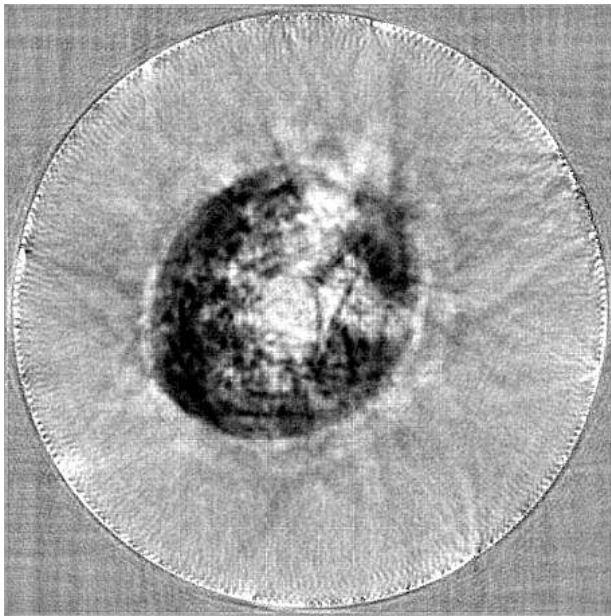
The patient was then scanned using UST and USWT was applied to create a USWT sound speed map of the breast in Figure 7.5(c). Viewing the USWT image reveals two masses, one 3.0 (long axis) x 2.4 (shorter axis) cm mass with mean sound speed 1545 +/- 17 m/s near the center of the breast and another 1.8 (TR) x 1.5 (CC) cm mass with mean sound speed 1561 +/- 15 closer to the edge. The shape and margins as revealed by the waveform



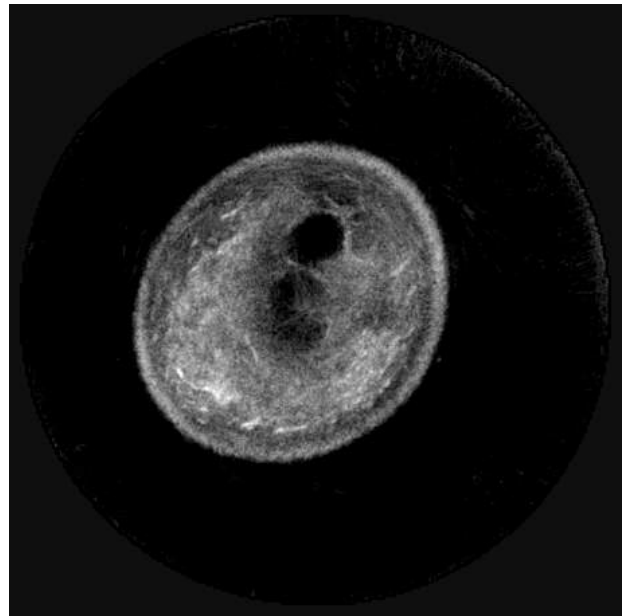
(a)



(b)



(c)



(d)

Figure 7.5: Images Corresponding to Case 4. (a) Cranial-Caudal mammogram. (b) Hand-Held ultrasound. (c) Waveform sound speed. (d) Reflection envelope.

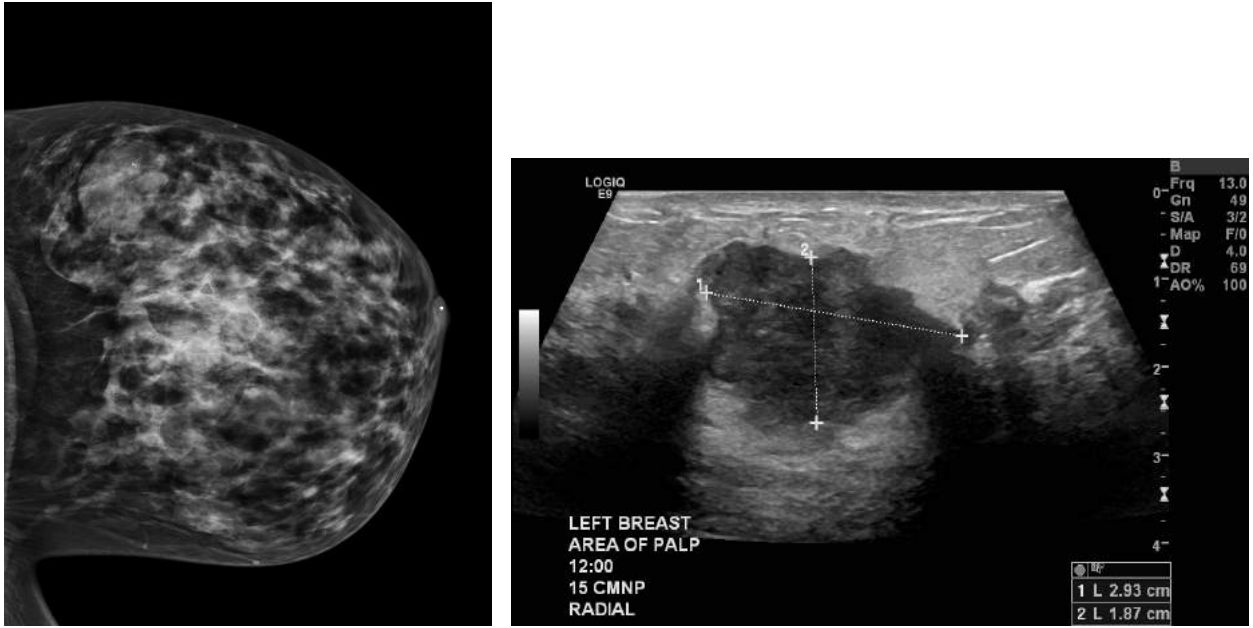
sound speed image are fairly well defined for the central cyst but more diffuse for the upper cyst. In contrast, the reflection envelope image (Figure 7.5(d)) reveals a well-defined mass at the outer edge and a more diffuse mass at the center. The Mean sound speeds of the fibroglandular region surrounding the tumor and a fatty region of the breast are 1524 ± 24 m/s and 1444 ± 22 m/s, respectively.

In this example we highlight the difficulty of using mammograms to find masses in dense breasts. The high amount of fibroglandular content greatly obscures the readability of a mammogram. In this breast, many cysts were present. We have not shown all the imaged lesions using HHUS, but have given an example in this section as well as the lesions presented in Figures 1.3(a) and 1.3(b). When there are many lesions present, then there would be a higher chance that the operator would not locate one. Since UST is automatic (up to initial breast alignment in the imaging chamber), there should be a significant improvement in the reproducibility of a breast scan. Due to problems in registering images, we have not made a comparison of the spatial extent of the tumors. We comment that their relative shape, margins, and sound speed of the tumors as revealed by UST are consistent with benign cysts.

7.2.6 Case 5 - Large Cancer in Older Female with Extremely Dense Breasts (SV161)

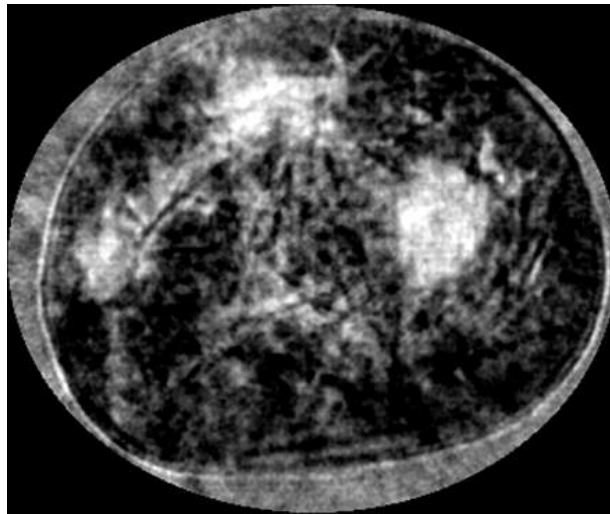
A 54-year-old female with prior history of benign breast disease and a palpable area of concern had a diagnostic mammogram performed. Prior mammograms were not available for comparison. The diagnostic exam revealed an extremely dense breast with a circumscribed mass and an associated biopsy clip corresponding to a prior benign finding. In addition, a lobular mass measuring 4.3 cm (AP) was found in the palpable area of concern (see Figure 7.6(a)).

Subsequent HHUS revealed an irregular hypoechoic mass with internal vascularity measuring 2.9 x 1.9 (length x height in radial plane) and 4.0 cm x 1.9 cm (length x height in anti-radial plane) (see Figure 7.6(b)). Pathology revealed a poorly differentiated grade 3 ductal carcinoma. The patient was then scanned using UST and USWT was applied to create a USWT sound speed map of the breast in Figure 7.6(c). Viewing the USWT image



(a)

(b)



(c)

Figure 7.6: Images Corresponding to Case 5. (a) Mammogram. (b) Hand-Held ultrasound. (c) Waveform sound speed.

reveals two masses, one cancer at the 12 o'clock position measuring 4.5 cm (long axis) x 2.2 cm (short axis) with mean sound speed 1567 ± 25 m/s and one fibroadenoma at the 3 o'clock position measuring 3.9 cm (long axis) x 3.0 cm (short axis) cm mass with mean sound speed 1573 ± 27 m/s. Mean sound speeds of the fibroglandular region surrounding the cancer and of a fatty region in the breast were 1504 ± 31 m/s and 1459 ± 23 m/s, respectively.

In this example, we find a cancer in an extremely dense breast. Again, an extremely dense breast hinders the ability of a radiologist to make an informed diagnosis based on mammography alone. HHUS was needed to help determine if the lesion imaged by mammography was benign or malignant. Since HHUS revealed a lesion with more diffuse and irregular margins, a biopsy was recommended. USWT sound speed images revealed masses with dimensions consistent with the HHUS findings. The cancer at the 12 o'clock position has diffuse boundaries and is not well-defined. The fibroadenoma at the 3 o'clock position is significantly more regular and lobular shaped. Since the sound speed of both lesions are very similar, it is difficult to make a diagnosis based on sound speed alone. However the shapes and margins of these tumors are consistent with what would be expected for a cancer and fibroadenoma. By using USWT sound speed imaging, we have shown an example where we were able to differentiate between malignant and benign tumors in an extremely dense breast.

CHAPTER 8: Conclusions

Breast cancer, a leading cause of cancer mortality, affects over 200,000 American women every year. Finding a cancer as early as possible will allow a patient to receive the best care. Current methods to detect breast cancer are deficient. Mammography as a screening tool leads to a significant improvement in the ability of a radiologist to make an informed diagnosis, however, the modality uses ionizing radiation, painful compression, and lacks specificity when used in women with dense breasts. An increase in specificity and thus a reduction in unneeded biopsies can be achieved by using hand-held ultrasound as an adjunct diagnostic tool. The shape and margins of unknown masses in B-mode reflection images provided by hand-held ultrasound can help distinguish malignant and benign tumors. The severe operator dependence of hand-held ultrasound limits its usefulness as a trained operator must navigate the breast volume where it is difficult to interpret the 3D breast using 2D slices in the radial and anti-radial planes. This can lead to unidentified lesions. In addition, only the reflected signals are used to assess the morphology of breast structures. Another great tool for the diagnosis of breast disease is MRI. It works very well, but its use in a screening environment is prohibitive due to its extreme operating cost.

A possible remedy to the various deficiencies listed above is the use of ultrasound tomography. Ultrasound tomography is virtually operator independent and uses no painful compression or ionizing radiation. Like MRI, and unlike mammography and hand-held ultrasound, ultrasound tomography is capable of completely imaging the breast by creating a series of 2D coronal tomographic slices. It is capable of producing B-mode reflection images akin to hand-held ultrasound in addition to capturing the transmitted signals which can be used to image transmission properties such as sound speed and attenuation. By using both the reflective and transmission properties of the breast, it is hoped that ultrasound tomography has increased sensitivity and specificity when compared to mammography and

hand-held ultrasound. This would be especially hopeful in dense breasted women who are at an increased cancer risk due to higher cancer incidence and mammographically occult lesions.

In this thesis, we have developed an ultrasound waveform tomography algorithm that estimates the sound speed of breast tissue to aid with the detection and diagnosis of breast cancer. In contrast to previous travel time tomography methods that used first arrival travel times to obtain the sound speed of the breast, the adopted method is based on the principles of full waveform inversion which models and utilizes the entire pressure wave field that is generated by acoustic excitation. In order to mitigate the extreme computation cost of full waveform modeling, we model acoustic wave propagation in the frequency domain by inverting a subset of the frequencies spanning the signal bandwidth of our ultrasound devices. We numerically simulate 2D acoustic wave propagation by using matrix inversion methods to solve a finite-difference matrix representation of the Helmholtz operator. We then solve the inverse problem by first forming a cost function defined as the difference between numerically and experimentally acquired pressure field data. We minimize the cost function in the least squares sense by using a gradient descent method which iteratively finds sound speed distributions which upon numerical forward modeling generates numerical pressure fields which best match the experimental data. Note that in order to successfully apply waveform tomography methods to experimentally gathered data, we require a method to properly preprocess experimental data. Note that in this thesis we have not presented *in vivo* waveform tomography attenuation reconstructions via a complex sound speed inversion. Additional research is required for the successful inversion of *in vivo* waveform tomography attenuation images. However, we can invert for attenuation using numerical simulations.

We have found that waveform tomography sound speed images have significantly improved resolution and accuracy when compared to travel time tomography methods. Numerical experiments reveal that the resolution of waveform tomography sound speed imaging is on the order of the ultrasound wavelength λ while the resolution of the travel time tomography is on the order of the first Fresnel zone $\sqrt{\lambda L}$, where L is the propagation distance

of the ultrasound wave. *Ex vivo* and *in vivo* experiments have shown that there is great improvements in the quality of the reconstructed images as most significantly highlighted by improvements in the shape and margins of tumors which are critical for an accurate diagnosis of breast disease. In addition, very fine parenchymal patterns of breast tissue are revealed by waveform tomography methods when only a fuzzy and blurred image was seen using travel time tomography methods.

Waveform tomography sound speed images have the potential to be a viable modality in a clinical setting. By comparing waveform tomography sound speed images to MRI, we have demonstrated a great deal of concordant findings. This ranges from the shape and margin of tumors as well as the imaging of very fine parenchymal patterns. We have also assessed the possible clinical role waveform tomography sound speed images might have in the diagnosis of unknown breast disease. We have shown that it is capable of imaging benign and malignant lesions in dense breast tissue which is a difficult environment for mammography. We believe that the use of waveform tomography sound speed imaging, ultrasound tomography B-mode imaging, and the attenuation properties of the breast can have a positive value in the prognosis of a patient. This belief can be verified or denied based on future studies which examine a large patient population.

In conclusion, we have presented a preliminary study of ultrasound waveform tomography sound speed imaging for the detection of breast disease. The improvements made upon our previous travel time based sound speed images are significant. The apparent improved contrast, better resolution, and more accurate margin delineation have the potential to greatly increase the clinical value of breast sound speed images. When compared to MRI, we see that the waveform tomography method has a great deal of concordant findings and can function as a poor man's MRI. By considering the impact of waveform tomography techniques in a clinical setting, it was shown that it can make a positive value in the life and prognosis of a patient. Current research is focusing on optimizing the algorithm, reducing the reconstruction time, and improving the reconstruction accuracy by reducing artifacts, investigating a more optimal transducer design, and using more transducers in the reconstruction process.

In addition, we are investigating the reconstruction of attenuation for *in vivo* data via the inversion of a complex valued sound speed.

APPENDIX A: Finite Difference Stencil

A.1 Real and Imaginary Parts of Slowness and its Derivatives

$$\begin{aligned}
\operatorname{Re}\left\{\frac{1}{c}\right\} &= \frac{c_R}{|c|^2} & \operatorname{Im}\left\{\frac{1}{c}\right\} &= \frac{-c_I}{|c|^2} \\
\operatorname{Re}\left\{\frac{1}{c^2}\right\} &= \frac{c_R^2 - c_I^2}{|c|^4} & \operatorname{Im}\left\{\frac{1}{c^2}\right\} &= \frac{-2c_R c_I}{|c|^4} \\
\operatorname{Re}\left\{\frac{\partial}{\partial c_R} \frac{1}{c}\right\} &= \frac{c_I^2 - c_R^2}{|c|^4} & \operatorname{Im}\left\{\frac{\partial}{\partial c_R} \frac{1}{c}\right\} &= \frac{2c_R c_I}{|c|^4} \\
\operatorname{Re}\left\{\frac{\partial}{\partial c_I} \frac{1}{c}\right\} &= \frac{-2c_R c_I}{|c|^4} & \operatorname{Im}\left\{\frac{\partial}{\partial c_I} \frac{1}{c}\right\} &= \frac{c_I^2 - c_R^2}{|c|^4} \\
\operatorname{Re}\left\{\frac{\partial}{\partial c_R} \frac{1}{c^2}\right\} &= \frac{2c_R(3c_I^2 - c_R^2)}{|c|^6} & \operatorname{Im}\left\{\frac{\partial}{\partial c_R} \frac{1}{c^2}\right\} &= \frac{2c_I(3c_R^2 - c_I^2)}{|c|^6} \\
\operatorname{Re}\left\{\frac{\partial}{\partial c_I} \frac{1}{c^2}\right\} &= \frac{-2c_I(3c_R^2 - c_I^2)}{|c|^6} & \operatorname{Im}\left\{\frac{\partial}{\partial c_I} \frac{1}{c^2}\right\} &= \frac{2c_R(3c_I^2 - c_R^2)}{|c|^6}
\end{aligned}$$

A.2 S Matrix: Interior Points

The discretized acquisition geometry is shown in Figure 3.1. The stencil for the field values $u_{m,n}$ are labeled according to the diagram in Figure A.1 where the positive x are given by index $m+1$, and the positive y values are given by index $n+1$. The stencil satisfies

$$\begin{aligned}
&\alpha_1 \frac{u_{m+1,n} + u_{m-1,n+1} - u_{m,n} + u_{m,n+1} + u_{m,n-1}}{\Delta^2} \\
&+ (1 - \alpha_1) \frac{u_{m+1,n+1} + u_{m+1,n-1} + u_{m-1,n+1} + u_{m-1,n-1}}{(\sqrt{2}\Delta)^2} \\
&+ \frac{\omega^2}{c_{m,n}^2} \left[\alpha_2 + \alpha_3 (u_{m,n} + u_{m-1,n} + u_{m,n+1} + u_{m,n-1}) \right. \\
&\left. + \frac{1 - \alpha_2 - 4\alpha_3}{4} (u_{m+1,n} + u_{m+1,n-1} + u_{m-1,n+1} + u_{m-1,n-1}) \right] = -\delta_{m,n}(\omega).
\end{aligned} \tag{A.1}$$

Or collecting terms for the notation used in the implementation code

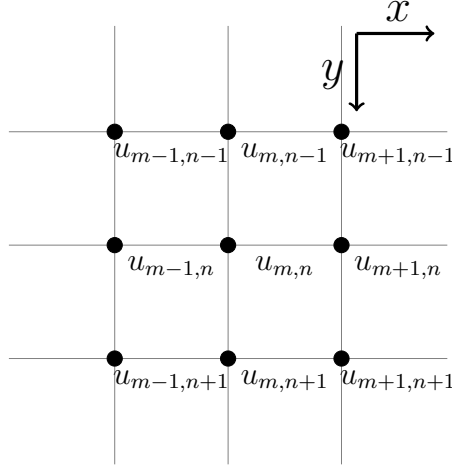


Figure A.1: Finite Difference Stencil. Field values $u_{m,n}$ are sampled on the corner points.

$$\begin{aligned}
& u_{m,n} \left(-\frac{4\alpha_1}{\Delta^2} - \frac{2(1-\alpha_1)}{\Delta^2} + \frac{\alpha_2\omega^2}{c_{m,n}^2} \right) + (u_{m+1,n} + u_{m-1,n} + u_{m,n+1} + u_{m,n-1}) \left(\frac{\alpha_1}{\Delta^2} + \frac{\alpha_3\omega^2}{c_{m,n}^2} \right) \\
& + (u_{m+1,n+1} + u_{m+1,n-1} + u_{m-1,n+1} + u_{m-1,n-1}) \left(\frac{(1-\alpha_1)}{2\Delta^2} + \frac{(1-\alpha_2-4\alpha_3)}{4} \frac{\omega^2}{c_{m,n}^2} \right) \\
& = -\delta_{m,n}(\omega).
\end{aligned} \tag{A.2}$$

Note that when $\alpha_1 = \alpha_2 = 1$ and $\alpha_3 = 0$, the optimal nine point stencil reduces to the typical Laplacian stencil. The real and imaginary parts of $1/c_{m,n}^2$ are then taken when inserting the discretized equation into arrays in the code.

A.3 S Matrix: Boundary Points

We model absorbing boundary conditions on the boundary $\partial\Omega$ by forcing only outward propagating wave solutions on the boundary [87]. In this development, we have followed the notation used in [87]. Therefore, we assume a plane wave of form $\exp[-i\mathbf{k} \cdot \mathbf{r}]$ which has an opposite sign to the discussion in sections 2.2.1 and 2.2.2. Thus, implementing the boundary conditions as outlined in this section would lead to a fundamental solution as given by the Hankel function of the second kind as opposed to the first kind. It would also require using $c_I > 0$ for attenuation to behave properly. For the left boundary, which we will force to only allow leftward propagating solutions, the 2nd order Engquist and Majda boundary condition

is given by

$$\left(\frac{1}{c} \frac{\partial^2}{\partial x \partial t} - \frac{1}{c^2} \frac{\partial^2}{\partial t^2} + \frac{1}{2} \frac{\partial^2}{\partial y^2} \right) u(\mathbf{r}, t)|_{\mathbf{r} \in \partial\Omega} = 0. \quad (\text{A.3})$$

Transforming into the frequency domain

$$\left(\frac{i\omega}{c} \frac{\partial}{\partial x} + \frac{\omega^2}{c^2} + \frac{1}{2} \frac{\partial^2}{\partial y^2} \right) u(\mathbf{r}, \omega)|_{\mathbf{r} \in \partial\Omega} = 0. \quad (\text{A.4})$$

Using only a 5 point stencil for the Laplacian and a forward difference for the first derivative term, the stencil satisfies

$$\frac{i\omega}{c_{m,n}} \frac{u_{m+1, -} - u_{m,n}}{\Delta} + \frac{\omega^2}{c_{m,n}^2} u_{m,n} + \frac{1}{2} \frac{u_{m,n+1} - 2u_{m,n} + u_{m,n-1}}{\Delta^2} = 0. \quad (\text{A.5})$$

Collecting terms for the notation use in implementation

$$u_{m,n} \left(\frac{\omega^2}{c_{m,n}^2} - \frac{1}{\Delta^2} - \frac{i\omega}{c_{m,n}} \frac{1}{\Delta} \right) + u_{m+1, -} \left(\frac{i\omega}{c_{m,n}} \frac{1}{\Delta} \right) + (u_{m,n+1} + u_{m,n-1}) \left(\frac{1}{2\Delta^2} \right) = 0. \quad (\text{A.6})$$

Expressions in terms of real and imaginary components will be explicitly given as terms involving i complicate matters.

$$\begin{aligned} \text{Real} \rightarrow & u_{m,n} \left(\omega^2 \text{Re}\{1/c_{m,n}^2\} - \frac{1}{\Delta^2} + \frac{\omega}{\Delta} \text{Im}\{1/c_{m,n}\} \right) \\ & + u_{m+1, -} \left(-\frac{\omega}{\Delta} \text{Im}\{1/c_{m,n}\} \right) + (u_{m,n+1} + u_{m,n-1}) \frac{1}{2\Delta^2} = 0, \\ \text{Imaginary} \rightarrow & u_{m,n} \left(\omega^2 \text{Im}\{1/c_{m,n}^2\} - \frac{\omega}{\Delta} \text{Re}\{1/c_{m,n}\} \right) + u_{m+1, -} \frac{\omega}{\Delta} \text{Re}\{1/c_{m,n}\} = 0. \end{aligned} \quad (\text{A.7})$$

A.4 S Matrix: Corner Points

Modeling the corners is a special case (see [88] or [89]). For the Top-Left corner, the equation satisfied is

$$\left(\frac{\partial}{\partial x} + \frac{\partial}{\partial y} + \frac{3}{2} \frac{1}{c} \frac{\partial}{\partial t} \right) u(\mathbf{r}, t)|_{\mathbf{r} \in \partial\Omega} = 0. \quad (\text{A.8})$$

Transforming into the frequency domain

$$\left(\frac{\partial}{\partial x} + \frac{\partial}{\partial y} + \frac{3i\omega}{2c} \right) u(\mathbf{r}, \omega)|_{\mathbf{r} \in \partial\Omega} = 0. \quad (\text{A.9})$$

Using forward differences for the first derivative terms, the stencil satisfies

$$\frac{u_{m+1,n} - u_{m,n}}{\Delta} + \frac{u_{m,n+1} - u_{m,n}}{\Delta} + \frac{i\omega}{c_{m,n}} u_{m,n} = 0. \quad (\text{A.10})$$

Or collecting terms for the notation used in implementation

$$u_{m,n} \left(-\frac{2}{\Delta} + \frac{3i\omega}{2c_{m,n}} \right) + (u_{m+1,n} + u_{m,n+1}) \frac{1}{\Delta} = 0. \quad (\text{A.11})$$

We then again express in terms of real and imaginary parts for this particular boundary. Note that boundary conditions for the other boundaries/corners are then deduced by symmetry.

$$\begin{aligned} \text{Real} &\rightarrow u_{m,n} \left(-\frac{2}{\Delta} - \frac{3}{2}\omega \text{Im}\{1/c\} \right) + (u_{m+1,n} + u_{m,n+1}) \frac{1}{\Delta} = 0, \\ \text{Imaginary} &\rightarrow u_{m,n} \left(\frac{3}{2}\omega \text{Re}\{1/c\} \right) = 0. \end{aligned} \quad (\text{A.12})$$

A.5 Derivative of S Matrix: Interior Points

We will use $\partial/\partial m \equiv \partial/\partial c_R$ or $\partial/\partial c_I$ depending on if we are interested in a real or imaginary update. The only interesting terms in the stencil in equation A.2 are terms that involve the sound speed c . The others terms are lumped together in a constant \mathcal{C}

$$\begin{aligned} u_{m,n} \left(\mathcal{C} + \frac{\alpha_2 \omega^2}{c_{m,n}^2} \right) + (u_{m+1,n} + u_{m-1,n} + u_{m,n+1} + u_{m,n-1}) \left(\mathcal{C} + \frac{\alpha_3 \omega^2}{c_{m,n}^2} \right) \\ + (u_{m+1,n+1} + u_{m+1,n-1} + u_{m-1,n+1} + u_{m-1,n-1}) \left(\mathcal{C} + \frac{(1 - \alpha_2 - 4\alpha_3) \omega^2}{4 c_{m,n}^2} \right) = \mathcal{C}. \end{aligned} \quad (\text{A.13})$$

Then taking derivatives and expressing in terms of the real and imaginary parts we obtain

$$\begin{aligned}
\text{Real} &\rightarrow u_{m,n} \alpha_2 \omega^2 \operatorname{Re} \left\{ \frac{\partial}{\partial m} \frac{1}{c_{m,n}^2} \right\} + (u_{m+1,n} + u_{m-1,n} + u_{m,n+1} + u_{m,n-1}) \alpha_3 \omega^2 \operatorname{Re} \left\{ \frac{\partial}{\partial m} \frac{1}{c_{m,n}^2} \right\} \\
&+ (u_{m+1,n+1} + u_{m+1,n-1} + u_{m-1,n+1} + u_{m-1,n-1}) \frac{(1 - \alpha_2 - 4\alpha_3)}{4} \omega^2 \operatorname{Re} \left\{ \frac{\partial}{\partial m} \frac{1}{c_{m,n}^2} \right\}, \\
\text{Imaginary} &\rightarrow u_{m,n} \alpha_2 \omega^2 \operatorname{Im} \left\{ \frac{\partial}{\partial m} \frac{1}{c_{m,n}^2} \right\} \\
&+ (u_{m+1,n} + u_{m-1,n} + u_{m,n+1} + u_{m,n-1}) \alpha_3 \omega^2 \operatorname{Im} \left\{ \frac{\partial}{\partial m} \frac{1}{c_{m,n}^2} \right\} \\
&+ (u_{m+1,n+1} + u_{m+1,n-1} + u_{m-1,n+1} + u_{m-1,n-1}) \frac{(1 - \alpha_2 - 4\alpha_3)}{4} \omega^2 \operatorname{Im} \left\{ \frac{\partial}{\partial m} \frac{1}{c_{m,n}^2} \right\}.
\end{aligned} \tag{A.14}$$

A.6 Derivative of S Matrix: Boundary Points

Lumping together constant terms in equation A.6 as we did for the interior case

$$u_{m,n} \left(\frac{\omega^2}{c_{m,n}^2} - \mathcal{C} - \frac{i\omega}{c_{m,n}} \frac{1}{\Delta} \right) + u_{m+1,n} \frac{i\omega}{c_{m,n}} \frac{1}{\Delta} + (u_{m,n+1} + u_{m,n-1}) \mathcal{C} = 0. \tag{A.15}$$

We then express in terms of real and imaginary parts. We again emphasize that depending on the model update of interest $m = c_R$ or $m = c_I$, we take the appropriate $\partial/\partial m$

$$\begin{aligned}
\text{Real} &\rightarrow u_{m,n} \left(\omega^2 \operatorname{Re} \left\{ \frac{\partial}{\partial m} \frac{1}{c_{m,n}^2} \right\} + \frac{\omega}{\Delta} \operatorname{Im} \left\{ \frac{\partial}{\partial m} \frac{1}{c_{m,n}} \right\} \right) + u_{m+1,n} \left(-\frac{\omega}{\Delta} \operatorname{Im} \left\{ \frac{\partial}{\partial m} \frac{1}{c_{m,n}} \right\} \right) = 0, \\
\text{Imaginary} &\rightarrow u_{m,n} \left(\omega^2 \operatorname{Im} \left\{ \frac{\partial}{\partial m} \frac{1}{c_{m,n}^2} \right\} - \frac{\omega}{\Delta} \operatorname{Re} \left\{ \frac{\partial}{\partial m} \frac{1}{c_{m,n}} \right\} \right) \\
&+ u_{m+1,n} \left(\frac{\omega}{\Delta} \operatorname{Re} \left\{ \frac{\partial}{\partial m} \frac{1}{c_{m,n}} \right\} \right) = 0.
\end{aligned} \tag{A.16}$$

A.7 Derivative of S Matrix: Corner Points

We have from the corners stencil in equation A.11

$$u_{m,n} \left(\mathcal{C} + \frac{3}{2} \frac{i\omega}{c_{m,n}} \right) + (u_{m+1,n} + u_{m,n+1}) \mathcal{C} = 0. \tag{A.17}$$

And in terms of real and imaginary parts

$$\begin{aligned} \text{Real} &\rightarrow u_{m,n} \left(-\frac{3}{2}\omega \operatorname{Im} \left\{ \frac{\partial}{\partial m} \frac{1}{c_{m,n}} \right\} \right) = 0, \\ \text{Imaginary} &\rightarrow u_{m,n} \left(\frac{3}{2}\omega \operatorname{Re} \left\{ \frac{\partial}{\partial m} \frac{1}{c_{m,n}} \right\} \right) = 0. \end{aligned} \quad (\text{A.18})$$

A.8 Example of Matrix Representing Finite Difference Stencil

We give an explicit example of the structure of the matrix \mathbf{S} which represents the finite difference stencil representation of the Helmholtz operator in equation 3.1. The matrix equation is given by

$$\mathbf{S}\mathbf{u} = \mathbf{s}, \quad (\text{A.19})$$

where the vector of field values is \mathbf{u} and the source vector is \mathbf{s} . We will use the standard 5-point formula for the Laplacian operator. Then, equation 3.1 becomes

$$\begin{aligned} \left(\nabla^2 + \frac{\omega^2}{c(\mathbf{r}_{m,n})^2} \right) u(\mathbf{r}_{m,n}, \omega) \approx \\ \frac{u_{m+1,n} + u_{m-1,n} - 4u_{m,n} + u_{m,n+1} + u_{m,n-1}}{\Delta^2} + \frac{\omega^2}{c_{m,n}^2} u_{m,n} = -\delta_{m,n}(\omega), \quad \mathbf{r}_{m,n} \in \Omega. \end{aligned} \quad (\text{A.20})$$

In this example we will discretize the problem domain Ω into a 9×9 grid. We also ignore boundary conditions. Setting $\Delta = 1$, and letting $\xi_{m,n} = -4 + \omega^2/c_{m,n}^2$, we combine equations A.19 and A.20 to generate the system of equations shown in equation A.21

$$\begin{pmatrix} \xi_{1,1} & 1 & 0 & 1 & 0 & 0 & 0 & 0 & 0 \\ 1 & \xi_{2,2} & 1 & 0 & 1 & 0 & 0 & 0 & 0 \\ 0 & 1 & \xi_{3,3} & 0 & 0 & 1 & 0 & 0 & 0 \\ 1 & 0 & 0 & \xi_{4,4} & 1 & 0 & 1 & 0 & 0 \\ 0 & 1 & 0 & 1 & \xi_{5,5} & 1 & 0 & 1 & 0 \\ 0 & 0 & 1 & 0 & 1 & \xi_{6,6} & 0 & 0 & 1 \\ 0 & 0 & 0 & 1 & 0 & 0 & \xi_{7,7} & 1 & 0 \\ 0 & 0 & 0 & 0 & 1 & 0 & 1 & \xi_{8,8} & 1 \\ 0 & 0 & 0 & 0 & 0 & 1 & 0 & 1 & \xi_{9,9} \end{pmatrix} \begin{pmatrix} u_{1,1} \\ u_{1,2} \\ u_{1,3} \\ u_{2,1} \\ u_{2,2} \\ u_{2,3} \\ u_{3,1} \\ u_{3,2} \\ u_{3,3} \end{pmatrix} = \begin{pmatrix} 0 \\ 0 \\ 0 \\ s \\ 0 \\ 0 \\ 0 \\ 0 \\ 0 \end{pmatrix}. \quad (\text{A.21})$$

\mathbf{s}
 \mathbf{u}
 \mathbf{s}

APPENDIX B: Inverse Problem

B.1 Line Search Estimation

In order to find the optimal value of the step length α , we need to minimize the cost function E with respect to the step length. Letting the cost function E be

$$E(\mathbf{c}) = \frac{1}{2} (\mathbf{u}(\mathbf{c}) - \mathbf{d})^H (\mathbf{u}(\mathbf{c}) - \mathbf{d}), \quad (\text{B.1})$$

where the experimental data is denoted \mathbf{d} , and the synthetic data term \mathbf{u} is non-linearly dependent on some model \mathbf{c} . Taking the derivative of the cost function E with respect to the step length α gives

$$\frac{\partial E}{\partial \alpha} = \frac{1}{2} \left\{ \left(\frac{\partial \mathbf{u}(\mathbf{c})}{\partial \alpha} \right)^H (\mathbf{u}(\mathbf{c}) - \mathbf{d}) + (\mathbf{u}(\mathbf{c}) - \mathbf{d})^H \frac{\partial \mathbf{u}(\mathbf{c})}{\partial \alpha} \right\}. \quad (\text{B.2})$$

We need to obtain an expression for $\partial \mathbf{u}(\mathbf{c}) / \partial \alpha$. Assuming linearity of $\mathbf{u}(\mathbf{c}^{k+1})$ with respect to perturbations to the current model k , we expand the wave field \mathbf{u} using the update equation 4.3 and a Taylor expansion

$$\begin{aligned} \mathbf{u}(\mathbf{c}^{k+1}) &= \mathbf{u}(\mathbf{c}^k - \alpha^k \nabla E(\mathbf{c}^k)) \\ &\approx \mathbf{u}(\mathbf{c}^{k+1}) - \alpha^k \nabla \mathbf{u}(\mathbf{c}^k)^H \nabla E(\mathbf{c}^k) + \mathcal{O}\left(\frac{\partial^2}{\partial \mathbf{c}^2}\right). \end{aligned} \quad (\text{B.3})$$

We then take the partial derivative of the wavefield with respect to α^k

$$\frac{\partial \mathbf{u}(\mathbf{c}^{k+1})}{\partial \alpha^k} = \frac{\partial \mathbf{u}(\mathbf{c}^k)}{\partial \alpha^k} - \nabla \mathbf{u}(\mathbf{c}^k)^H \nabla E(\mathbf{c}^k) - \alpha^k \frac{\partial^2 \mathbf{u}(\mathbf{c}^k)^H}{\partial \alpha^k \partial \mathbf{c}^k} \nabla E(\mathbf{c}^k). \quad (\text{B.4})$$

To simplify notation, we will now omit the iteration superscript k and the explicit dependence on \mathbf{c} . Ignoring terms that involve second derivatives, using the chain rule, and substituting equation B.4 into B.2. We have

$$\begin{aligned}
2\frac{\partial E}{\partial \alpha} &= \left(\nabla \mathbf{u} \frac{\partial \mathbf{u}}{\partial \alpha} - \nabla \mathbf{u} \nabla E \right)^H (\mathbf{u} - \alpha \nabla \mathbf{u} \nabla E - \mathbf{d}) \\
&+ (\mathbf{u} - \alpha \nabla \mathbf{u} \nabla E - \mathbf{d})^H \left(\nabla \mathbf{u} \frac{\partial \mathbf{u}}{\partial \alpha} - \nabla \mathbf{u} \nabla E \right) \\
&= -2 \left\{ \nabla E^H \nabla \mathbf{u}^H (\mathbf{u} - \alpha \nabla \mathbf{u} \nabla E - \mathbf{d}) + (\mathbf{u} - \alpha \nabla \mathbf{u} \nabla E - \mathbf{d})^H \nabla E \nabla \mathbf{u} \right\} \\
&= -2 \left\{ \nabla E^H \nabla \mathbf{u}^H (\mathbf{u} - \mathbf{d}) + (\mathbf{u} - \mathbf{d})^H \nabla E \nabla \mathbf{u} - 2\alpha \nabla E^H \nabla \mathbf{u}^H \nabla \mathbf{u} \nabla E \right\} \\
&= -4 \left\{ \nabla E^H \nabla E - \alpha \nabla E^H \nabla \mathbf{u}^H \nabla \mathbf{u} \nabla E \right\} .
\end{aligned} \tag{B.5}$$

Setting the left hand side of equation B.5 to zero then gives us an expression for the step length

$$\alpha = \frac{\nabla E^H \nabla E}{\nabla E^H \nabla \mathbf{u}^H \nabla \mathbf{u} \nabla E} . \tag{B.6}$$

B.2 Cost Function Gradient

The following discussion will establish a relationship between the cost function

$$E = 1/2 (u(c) - d)^* (u(c) - d) , \tag{B.7}$$

the Fréchet derivatives $J = \nabla u$, and the data residual $\delta d = u(c) - d$. Namely, we will show

$$\nabla E = \text{Re}\{J^* \delta d\} , \tag{B.8}$$

where the gradient ∇ can be taken with respect to the real or imaginary component of the velocity $\nabla = \partial/\partial c_R$ or $\partial/\partial c_I$. We will use $\nabla = \partial/\partial c$ for notational simplicity. Note that the fields values $u(c)$ are non-linear functions of the sound speed c . Taking the derivative of the cost function in equation B.7 and recognizing that both $u(c)$ and d have real and imaginary parts yields

$$2\frac{\partial E}{\partial c} = \frac{\partial u^*}{\partial c} (u - d) + (u - d)^* \frac{\partial u}{\partial c} \quad (\text{B.9a})$$

$$= \left(\frac{\partial u_R}{\partial c} - i \frac{\partial u_I}{\partial c} \right) (u_R + i u_I - d_R - i d_I) \\ + (u_R - i u_I - d_R + i d_I) \left(\frac{\partial u_R}{\partial c} + i \frac{\partial u_I}{\partial c} \right) \quad (\text{B.9b})$$

$$= \frac{\partial u_R}{\partial c} u_R + \frac{\partial u_I}{\partial c} u_I - \frac{\partial u_R}{\partial c} d_R - \frac{\partial u_I}{\partial c} d_I. \quad (\text{B.9c})$$

The term $J^* \delta d$ is expanded to give

$$J^* \delta d = \frac{\partial u^*}{\partial c} (u - d) \quad (\text{B.10a})$$

$$= \left(\frac{\partial u^*}{\partial c} - i \frac{\partial u_I}{\partial c} \right) (u_R + i u_I - d_R - i d_I) \quad (\text{B.10b})$$

$$= \left(\frac{\partial u_R}{\partial c} u_R + \frac{\partial u_I}{\partial c} u_I - \frac{\partial u_R}{\partial c} d_R - \frac{\partial u_I}{\partial c} d_I \right) \\ + i \left(-\frac{\partial u_I}{\partial c} u_R + \frac{\partial u_R}{\partial c} u_I + \frac{\partial u_I}{\partial c} d_R - \frac{\partial u_R}{\partial c} d_I \right). \quad (\text{B.10c})$$

Thus, we can see that equation B.8 is true.

B.3 Gradient Example

In section 4.3 we discuss the use of the gradient descent method to iteratively find the sound speed model \mathbf{c} that minimizes the cost function E . The reader is referred to [97] for an excellent resource for understanding the gradient descent method. In this section, we give a simple example of using the gradient descent method to find the solution of a concave system of linear equations. Consider the system

$$\mathbf{Ax} = \mathbf{b}, \quad \mathbf{A} = \begin{pmatrix} 3 & 2 \\ 2 & -6 \end{pmatrix}, \quad \mathbf{b} = \begin{pmatrix} 2 \\ -8 \end{pmatrix}.$$

The system is also represented by the linear equations

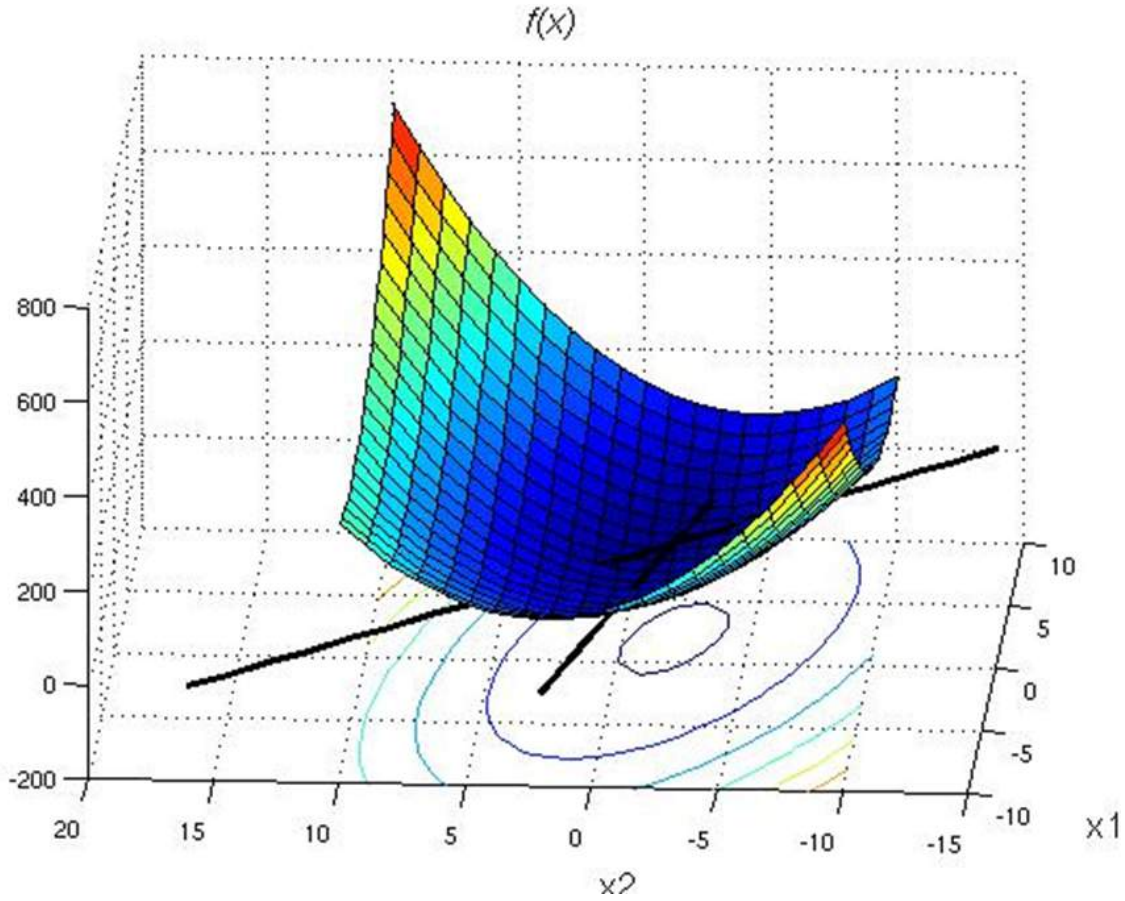


Figure B.1: Surface and Contour Lines Representing the Cost Function $f(\mathbf{x})$. Lines representing the system of equations intersect at the minimum point of $f(\mathbf{x})$.

$$x_2 = \frac{1}{6}(-8 - 2x_1)$$

$$x_2 = \frac{1}{2}(2 - 3x_1),$$

which is also seen in Figure B.1 as the two black lines. Define the cost function $f(\mathbf{x})$ for this problem to be

$$f(\mathbf{x}) = \|\mathbf{Ax} - \mathbf{b}\|^2.$$

which is also seen in Figure B.1 as the concave manifold. The gradient update procedure is given by

$$\mathbf{x}^{(i+1)} = \mathbf{x}^{(i)} - \alpha \nabla_x f(\mathbf{x}^{(i)}).$$

where i is the iteration number, α is a step size, and ∇_x is the gradient with respect to \mathbf{x} .

Guess an initial point \mathbf{x}_0 as the solution to the system (or \mathbf{c}_0 from section 4.3). Letting $\alpha = 1$, the first update is then given by

$$\mathbf{x}_1 = \mathbf{x}_0 - 2\mathbf{A}^T (\mathbf{A}\mathbf{x}_0 - \mathbf{b}) .$$

where T is the transpose operator. You can continue in this manner until you reach the optimal solution $x_{opt} = (2, -2)^T$. In this simple example the choice for the starting model \mathbf{x}_0 is not as important, but for multi-dimensional ill-posed problems, many local minimums exist in the cost function $f(\mathbf{x})$ (or E from section 4.3). For these ill-posed problems, selecting an initial point close to the global minimum is crucial for convergence to the global minimum. For example, for the application of the frequency domain ultrasound waveform tomography gradient descent method to experimental data, choosing the sound speed model \mathbf{c}_{ray} created using ray tomography methods leads to convergence to a global minimum, while using a constant sound speed of model of $c_0 \approx c_{H_2O}$ leads to rapid divergence. This contrasts with the numerical case where a constant sound speed model approximately average of the true model is sufficient at driving convergence to the global minimum.

APPENDIX C: Common Shot Gathers and Frequency Spectrums

A common shot gather of a water shot, a scattered density breast, and a dense breast are seen in Figures C.1, C.2, and C.3, respectively. After preprocessing the waveforms using the methods detailed in section 5.2, we have show common shot gathers of the scattered breast and very dense breast in Figures C.4, and C.5. The corresponding magnitude spectrums of the Fourier transforms of the preprocessed data are seen in Figures C.6, C.7, and C.8.

Denser breasts scatter and attenuate ultrasound waves more readily than fattier breasts. The scattering results in more multiply reflected signals and the attenuation results in signals with decreasing magnitude. Thus, there is a greater chance that a time-of-flight picker will get more confused in a dense breast. The presence of a denser breast also alters the filtering of the received frequencies with respect to the water shot frequency spectrum.

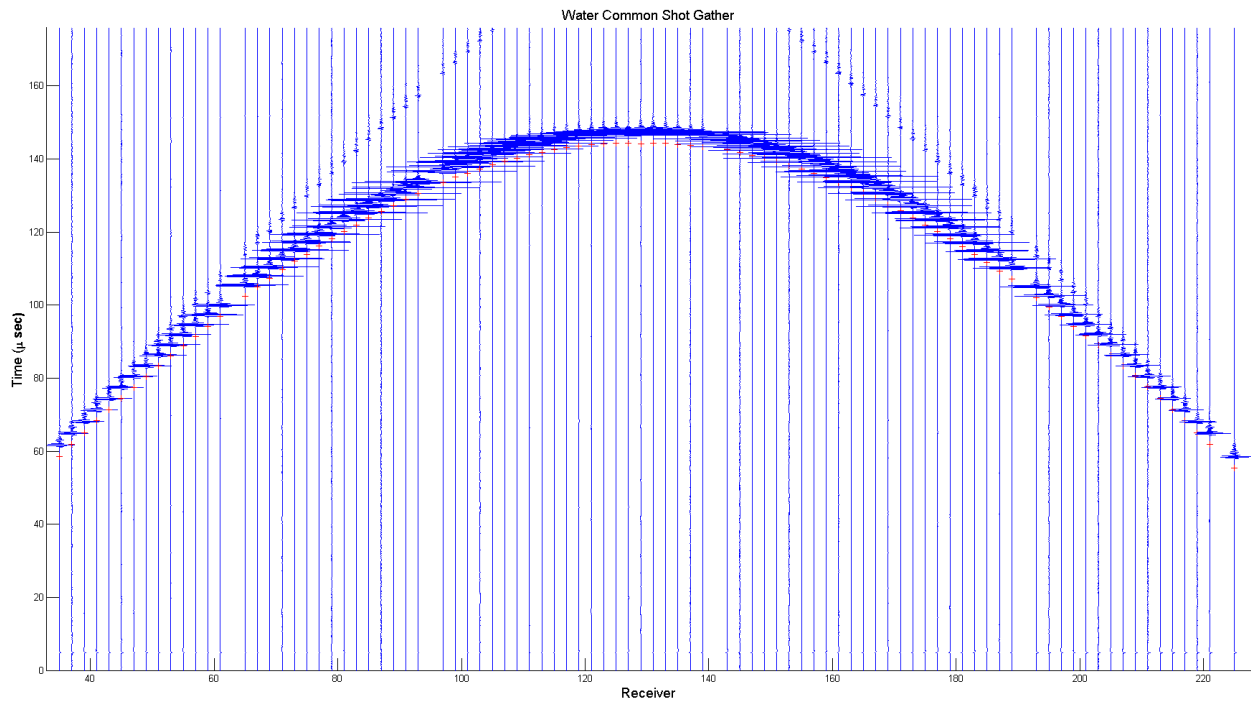


Figure C.1: Common Shot Gather of Water Shot. Overlaid are red crosses that are the first arrival times determined by the automatic TOF picking algorithm.

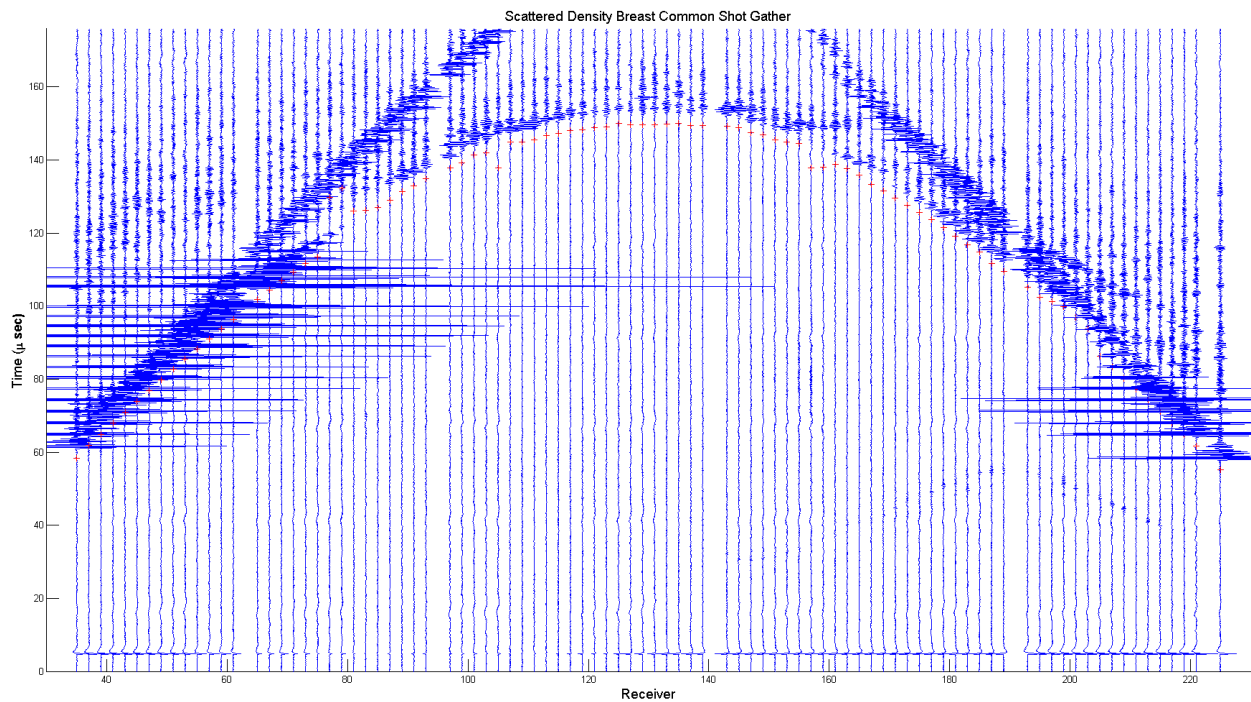


Figure C.2: Common Shot Gather of Scattered Density Breast. Overlaid are red crosses that are the first arrival times determined by the automatic TOF picking algorithm.

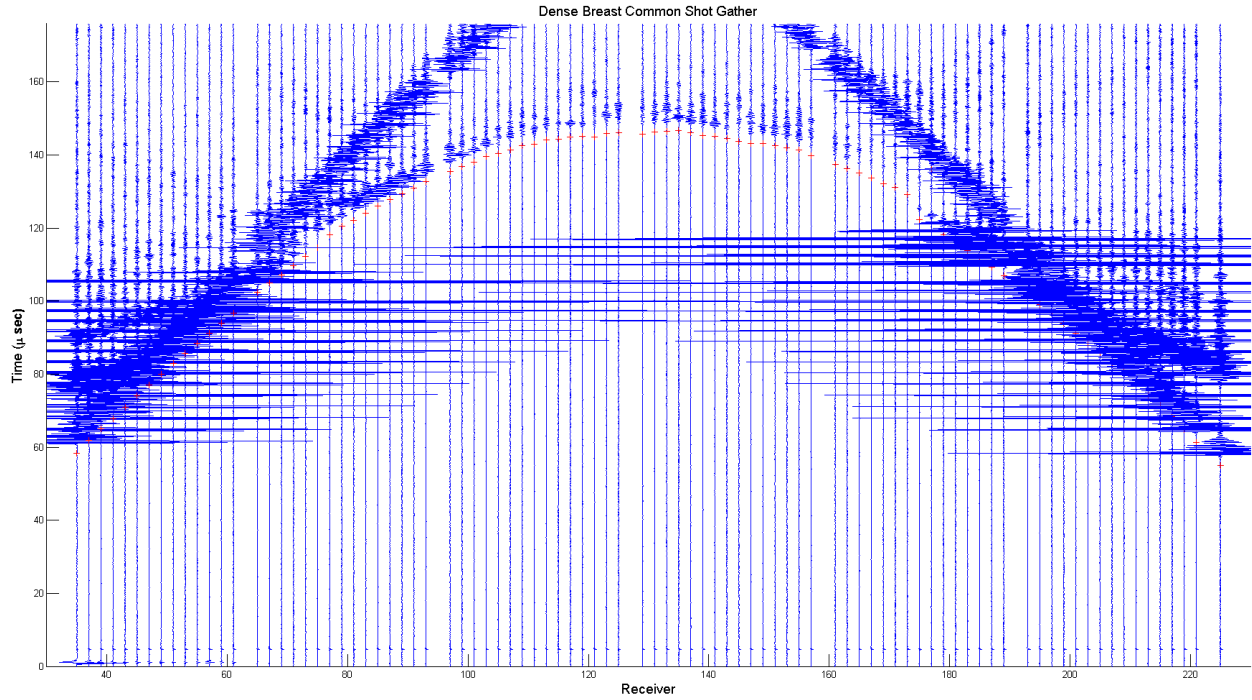


Figure C.3: Common Shot Gather of Dense Breast. Overlaid are red crosses that are the first arrival times determined by the automatic TOF picking algorithm.

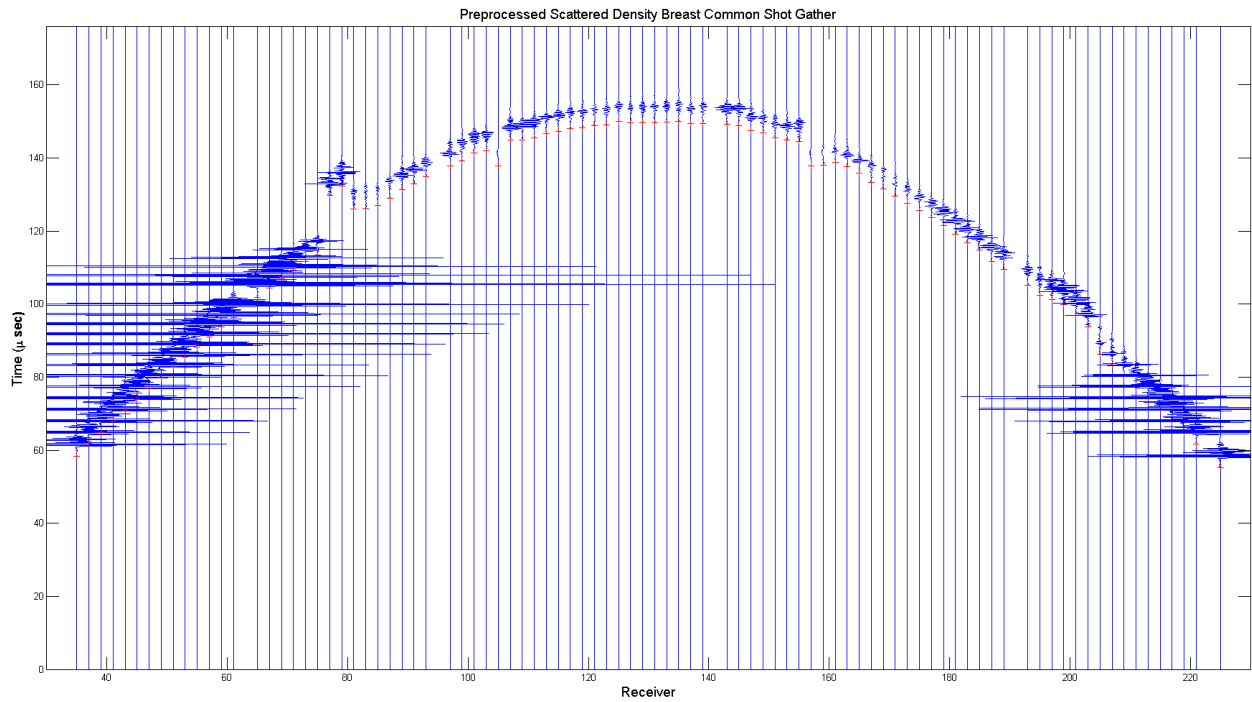


Figure C.4: Preprocessed Common Shot Gather of Scattered Density Breast. Overlaid are red crosses that are the first arrival times determined by the automatic TOF picking algorithm.

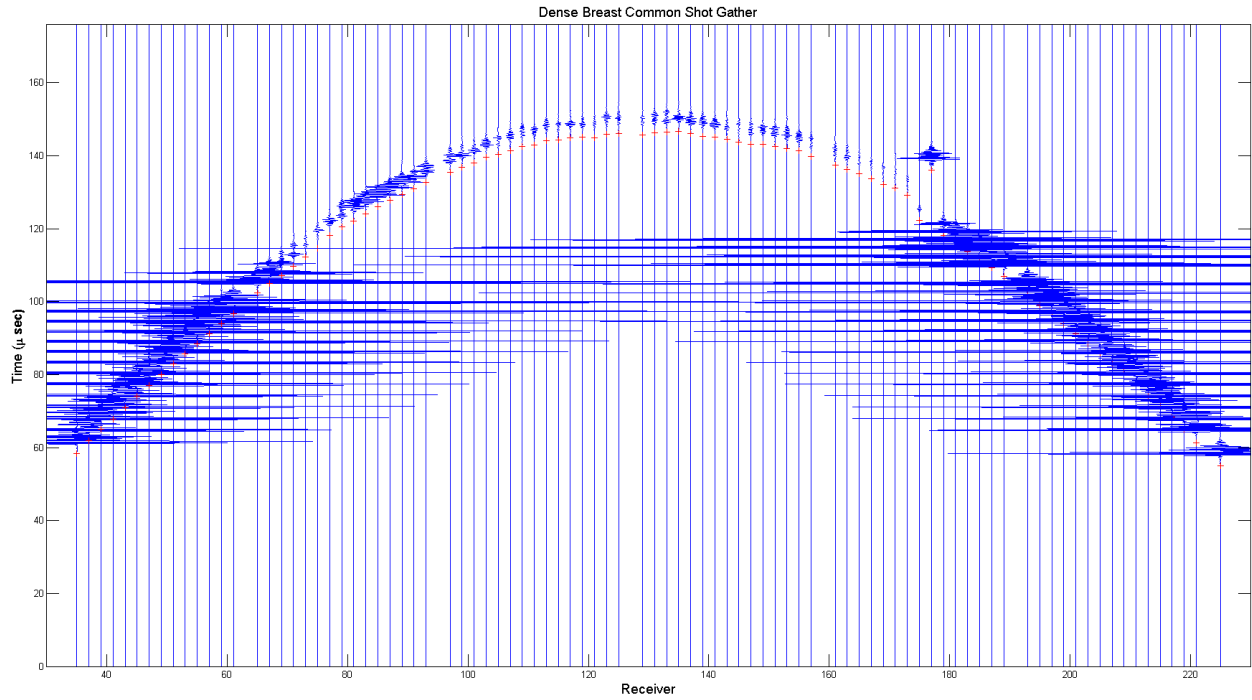


Figure C.5: Preprocessed Common Shot Gather of Dense Breast. Overlaid are red crosses that are the first arrival times determined by the automatic TOF picking algorithm.

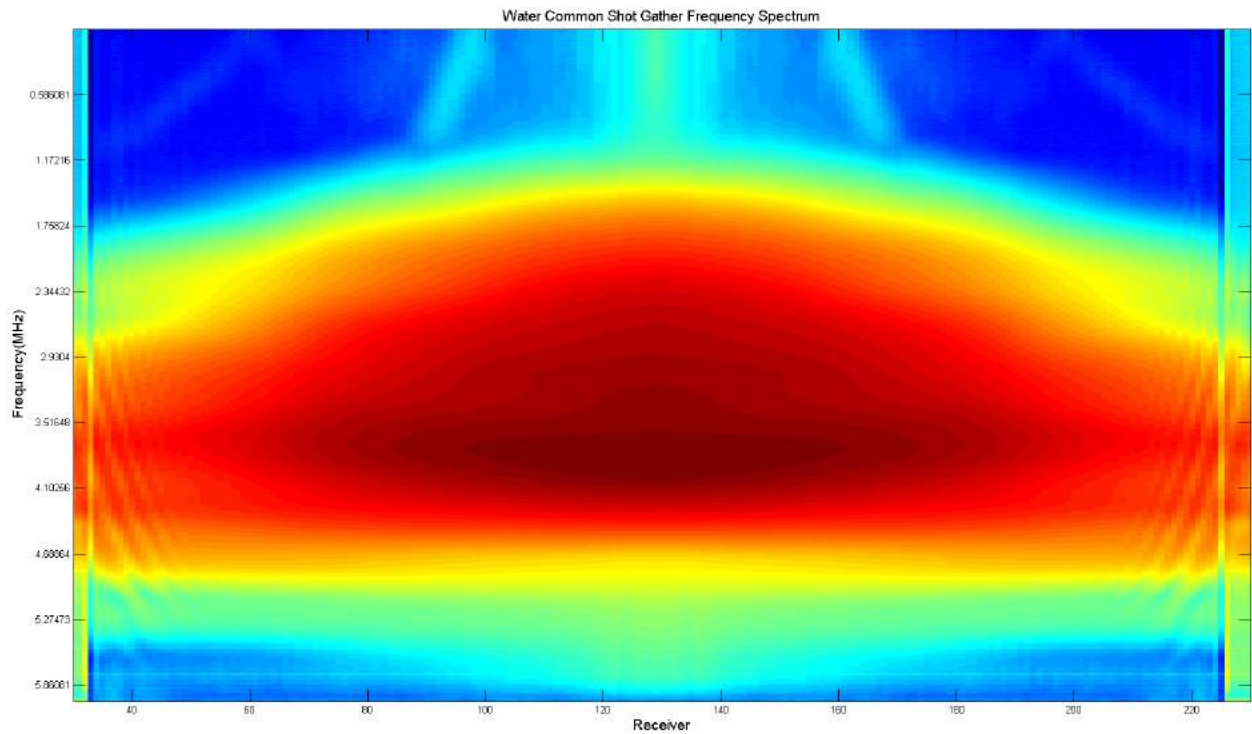


Figure C.6: Magnitude Spectrum of Preprocessed Common Shot Gather of Water Shot.

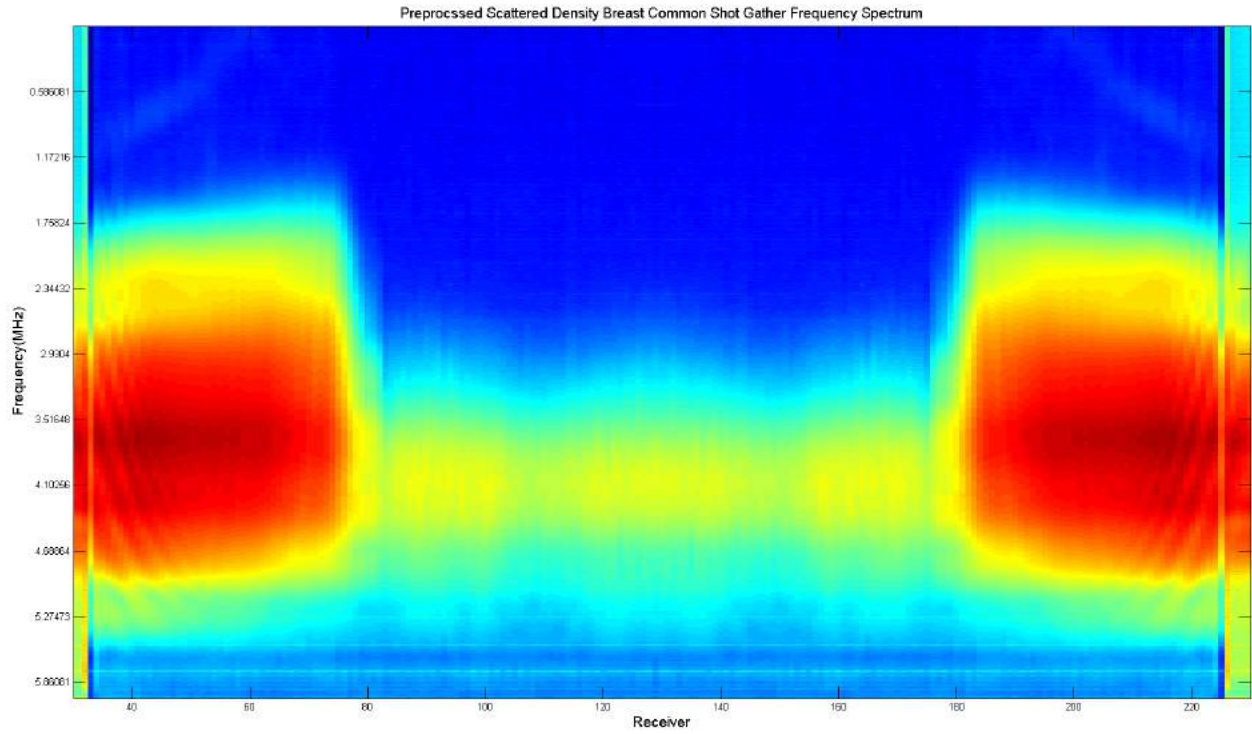


Figure C.7: Magnitude Spectrum of Preprocessed Common Shot Gather of Scattered Density Breast.

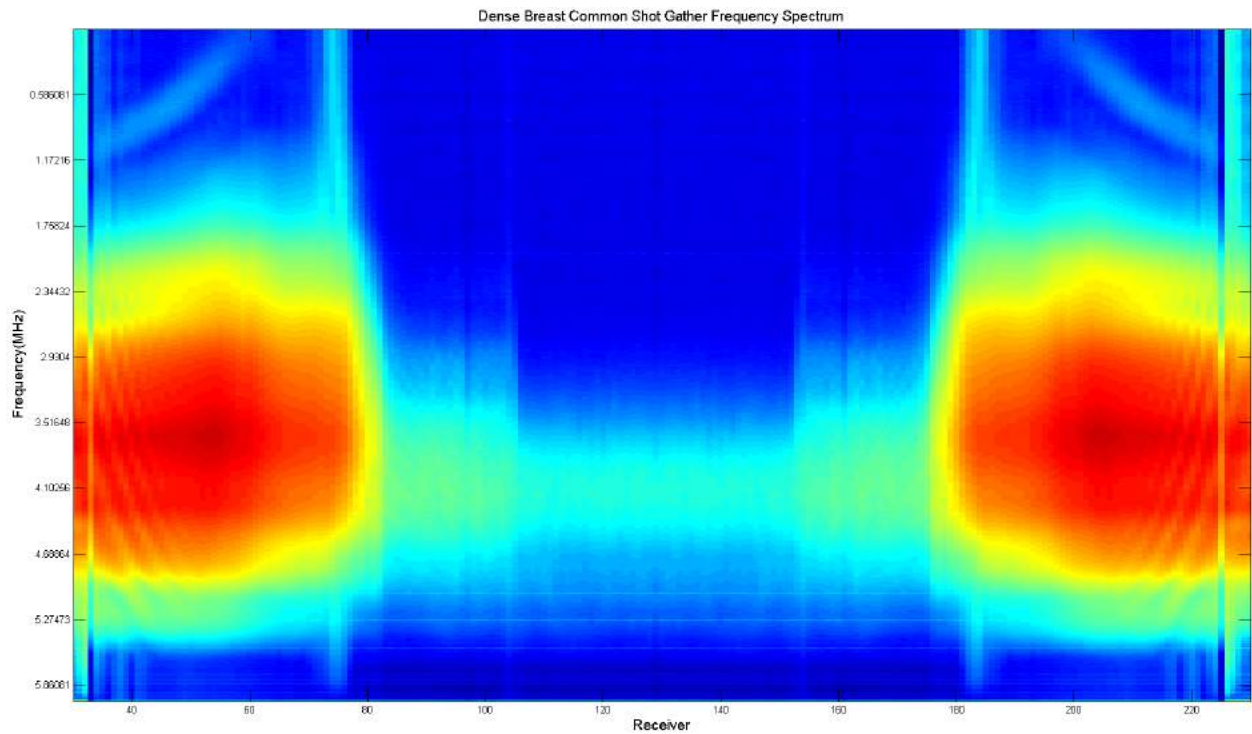


Figure C.8: Magnitude Spectrum of Preprocessed Common Shot Gather of Dense Breast.

REFERENCES

- [1] Carol DeSantis, Rebecca Siegel, Priti Bandi, and Ahmedin Jemal. Breast cancer statistics, 2011. *CA: a cancer journal for clinicians*, 61(6):408–418, 2011.
- [2] Jean Virieux and Stéphane Operto. An overview of full-waveform inversion in exploration geophysics. *Geophysics*, 74(6):WCC1–WCC26, 2009.
- [3] Cuiping Li, Neb Duric, and Lianjie Huang. Clinical breast imaging using sound-speed reconstructions of ultrasound tomography data. In *Medical Imaging*, pages 692009–692009. International Society for Optics and Photonics, 2008.
- [4] David O’Halloran, Kathryn Guyers, and Jill Henderson. *Notes on Anatomy and Oncology*. Elsevier Health Sciences, 2004.
- [5] Michael C Joiner and Albert van der Kogel. *Basic Clinical Radiobiology Fourth Edition*. CRC Press, 2009.
- [6] Stephen B Edge and Carolyn C Compton. The american joint committee on cancer: the 7th edition of the ajcc cancer staging manual and the future of tnm. *Annals of surgical oncology*, 17(6):1471–1474, 2010.
- [7] American College of Radiology. BI-RADS Committee and American College of Radiology. *Breast imaging reporting and data system*. American College of Radiology, 1998.
- [8] Patrick J. Lynch. Breast anatomy normal scheme, 2006.
- [9] A Marilyn Leitch, Gerald D Dodd, Mary Costanza, Michael Linver, Peter Pressman, LaMar McGinnis, and Robert A Smith. American cancer society guidelines for the early detection of breast cancer: update 1997. *CA: A cancer Journal for Clinicians*, 47(3):150–153, 1997.
- [10] Susan G. Komen for the Cure. Size of tumors found by mammography and breast self-exam, 2007.
- [11] Donald A Berry, Kathleen A Cronin, Sylvia K Plevritis, Dennis G Fryback, Lauren Clarke, Marvin Zelen, Jeanne S Mandelblatt, Andrei Y Yakovlev, J Dik F Habbema,

- and Eric J Feuer. Effect of screening and adjuvant therapy on mortality from breast cancer. *New England Journal of Medicine*, 353(17):1784–1792, 2005.
- [12] Blausen.com staff. Illustration of a mammogram, 2014.
- [13] Frank Herbert Attix. *Introduction to radiological physics and radiation dosimetry*. John Wiley & Sons, 2008.
- [14] Donald W Kufe, Raphael E Pollock, Ralph R Weichselbaum, Robert C Bast, Ted S Gansler, James F Holland, Emil Frei, Lawrence W Bassett, Karen Conner, et al. The abnormal mammogram. 2003.
- [15] National Cancer Institute. Mammograms fact sheet, year = .
- [16] Kristine Bihrmann, Allan Jensen, Anne Helene Olsen, Sisse Njor, Walter Schwartz, Ilse Vejborg, and Elsebeth Lynge. Performance of systematic and non-systematic (opportunistic) screening mammography: a comparative study from denmark. *Journal of Medical Screening*, 15(1):23–26, 2008.
- [17] Liezel Taylor, Sarinah Basro, Justus P Apffelstaedt, and Karin Baatjes. Time for a re-evaluation of mammography in the young? Results of an audit of mammography in women younger than 40 in a resource restricted environment. *Breast cancer research and treatment*, 129(1):99–106, 2011.
- [18] Anthony B Miller, Claus Wall, Cornelia J Baines, Ping Sun, Teresa To, Steven A Narod, et al. Twenty five year follow-up for breast cancer incidence and mortality of the canadian national breast screening study: randomised screening trial. *Bmj*, 348, 2014.
- [19] Peter C Gøtzsche and Ole Olsen. Is screening for breast cancer with mammography justifiable? *The Lancet*, 355(9198):129–134, 2000.
- [20] John D Keen. Promoting screening mammography: insight or uptake? *The Journal of the American Board of Family Medicine*, 23(6):775–782, 2010.
- [21] Yoshio Kasahara, Masaaki Kawai, Ichiro Tsuji, Eriko Tohno, Takao Yokoe, Minoru Irahara, Akira Tangoku, and Noriaki Ohuchi. Harms of screening mammography for breast cancer in japanese women. *Breast Cancer*, 20(4):310–315, 2013.

- [22] H Gilbert Welch and William C Black. Overdiagnosis in cancer. *Journal of the National Cancer Institute*, 102(9):605–613, 2010.
- [23] Iris Rosenfeld, Paul Ian Tartter, Csaba Gajdos, George Hermann, and Ira Bleiweiss. The significance of malignancies incidental to microcalcifications in breast spot localization biopsy specimens. *The American journal of surgery*, 182(1):1–5, 2001.
- [24] Nimmi Arora, Tari A King, Lindsay M Jacks, Michelle M Stempel, Sujata Patil, Elizabeth Morris, and Monica Morrow. Impact of breast density on the presenting features of malignancy. *Annals of surgical oncology*, 17(3):211–218, 2010.
- [25] Thomas M Kolb, Jacob Lichy, and Jeffrey H Newhouse. Comparison of the performance of screening mammography, physical examination, and breast us and evaluation of factors that influence them: An analysis of 27,825 patient evaluations 1. *Radiology*, 225(1):165–175, 2002.
- [26] Thomas A Stavros, David Thickman, Cynthia L Rapp, Mark A Dennis, Steve H Parker, and Gale A Sisney. Solid breast nodules: use of sonography to distinguish between benign and malignant lesions. *Radiology*, 196(1):123–134, 1995.
- [27] Wendie A Berg, Jeffrey D Blume, Jean B Cormack, Ellen B Mendelson, Daniel Lehrer, Marcela Böhm-Vélez, Etta D Pisano, Roberta A Jong, W Phil Evans, Marilyn J Morton, et al. Combined screening with ultrasound and mammography vs mammography alone in women at elevated risk of breast cancer. *Jama*, 299(18):2151–2163, 2008.
- [28] William R Hendee and E Russell Ritenour. *Medical imaging physics*. John Wiley & Sons, 2003.
- [29] Barys Ihnatsenka and André Pierre Boezaart. Ultrasound: Basic understanding and learning the language. *International journal of shoulder surgery*, 4(3):55, 2010.
- [30] James F Greenleaf, SA Johnson, and Robert C Bahn. Quantitative cross-sectional imaging of ultrasound parameters. In *Ultrasonics Symposium, 1977*, pages 989–995. IEEE, 1977.
- [31] Stephen J Norton and Melvin Linzer. Ultrasonic reflectivity tomography: reconstruction with circular transducer arrays. *Ultrasonic Imaging*, 1(2):154–184, 1979.

- [32] SA Goss, RL Johnston, and F Dunn. Comprehensive compilation of empirical ultrasonic properties of mammalian tissues. *The Journal of the Acoustical Society of America*, 64(2):423–457, 1978.
- [33] PD Edmonds, CL Mortensen, JR Hill, SK Holland, JF Jensen, P Schattner, AD Valdes, RH Lee, and FA Marzoni. Ultrasound tissue characterization of breast biopsy specimens. *Ultrasonic imaging*, 13(2):162–185, 1991.
- [34] Chen-Han Chang, Sheng-Wen Huang, Hsin-Chia Yang, Yi-Hong Chou, and Pai-Chi Li. Reconstruction of ultrasonic sound velocity and attenuation coefficient using linear arrays: Clinical assessment. *Ultrasound in medicine & biology*, 33(11):1681–1687, 2007.
- [35] Francis A. Duck. *Physical properties of tissues: a comprehensive reference book*. Academic press, 2013.
- [36] Paul L Carson, Charles R Meyer, Ann L Scherzinger, and Thomas V Oughton. Breast imaging in coronal planes with simultaneous pulse echo and transmission ultrasound. *Science*, 214(4525):1141–1143, 1981.
- [37] Michael P André, Helmar S Janeé, Peter J Martin, Gregory P Otto, Brett A Spivey, and Douglas A Palmer. High-speed data acquisition in a diffraction tomography system employing large-scale toroidal arrays. *International Journal of Imaging Systems and Technology*, 8(1):137–147, 1997.
- [38] Dong-Lai Liu and Robert C Waag. Propagation and backpropagation for ultrasonic wavefront design. *Ultrasonics, Ferroelectrics, and Frequency Control, IEEE Transactions on*, 44(1):1–13, 1997.
- [39] David T Borup, Steven A Johnson, Frank Natterer, Scott Charles Olsen, James W Wiskin, F Wubeling, and Yongzhi Zhang. Apparatus and method for imaging with wavefields using inverse scattering techniques, December 21 1999. US Patent 6,005,916.
- [40] Vasilis Z Marmarelis, Tae-Seong Kim, and Ramez EN Shehada. High-resolution ultrasound transmission tomography. In *Medical Imaging 2003*, pages 33–40. International Society for Optics and Photonics, 2003.
- [41] Nebojsa Duric, Peter Littrup, Alex Babkin, David Chambers, Stephen Azevedo,

- Arkady Kalinin, Roman Pevzner, Mikhail Tokarev, Earle Holsapple, Olsi Rama, et al. Development of ultrasound tomography for breast imaging: Technical assessment. *Medical Physics*, 32(5):1375–1386, 2005.
- [42] Nebojsa Duric, Peter Littrup, Lou Poulo, Alex Babkin, Roman Pevzner, Earle Holsapple, Olsi Rama, and Carri Glide. Detection of breast cancer with ultrasound tomography: First results with the computed ultrasound risk evaluation (CURE) prototype. *Medical physics*, 34(2):773–785, 2007.
- [43] Neb Duric, Peter Littrup, Steven Schmidt, Cuiping Li, Olivier Roy, Lisa Bey-Knight, Roman Janer, Dave Kunz, Xiaoyang Chen, Jeffrey Goll, et al. Breast imaging with the softvue imaging system: First results. In *SPIE Medical Imaging*, pages 86750K–86750K. International Society for Optics and Photonics, 2013.
- [44] Steven Schmidt, Nebojsa Duric, Cuiping Li, Olivier Roy, and Zhi-Feng Huang. Modification of kirchhoff migration with variable sound speed and attenuation for acoustic imaging of media and application to tomographic imaging of the breast. *Medical physics*, 38(2):998–1007, 2011.
- [45] Cuiping Li, Neb Duric, and Lianjie Huang. Comparison of ultrasound attenuation tomography methods for breast imaging. In *Medical Imaging*, pages 692015–692015. International Society for Optics and Photonics, 2008.
- [46] Cuiping Li, Nebojsa Duric, Peter Littrup, and Lianjie Huang. In vivo breast sound-speed imaging with ultrasound tomography. *Ultrasound in medicine & biology*, 35(10):1615–1628, 2009.
- [47] Carri Glide, Nebojsa Duric, and Peter Littrup. Novel approach to evaluating breast density utilizing ultrasound tomography. *Medical physics*, 34(2):744–753, 2007.
- [48] Carri K Glide-Hurst, Neb Duric, and Peter Littrup. Volumetric breast density evaluation from ultrasound tomography images. *Medical physics*, 35(9):3988–3997, 2008.
- [49] Norman F Boyd, Lisa J Martin, Michael Bronskill, Martin J Yaffe, Neb Duric, and Salomon Minkin. Breast tissue composition and susceptibility to breast cancer. *Journal of the National Cancer Institute*, 2010.

- [50] Mark Sak, Neb Duric, Norman Boyd, Peter Littrup, Erik West, and Cuiping Li. Breast tissue composition and breast density measurements from ultrasound tomography. In *SPIE Medical Imaging*, pages 83200Q–83200Q. International Society for Optics and Photonics, 2012.
- [51] Jon F Claerbout. Toward a unified theory of reflector mapping. *Geophysics*, 36(3):467–481, 1971.
- [52] Patrick Lailly. The seismic inverse problem as a sequence of before stack migrations. In *Conference on inverse scattering: theory and application*, pages 206–220. Society for Industrial and Applied Mathematics, Philadelphia, PA, 1983.
- [53] Albert Tarantola. Inversion of seismic reflection data in the acoustic approximation. *Geophysics*, 49(8):1259–1266, 1984.
- [54] Peter Mora. Nonlinear two-dimensional elastic inversion of multioffset seismic data. *Geophysics*, 52(9):1211–1228, 1987.
- [55] R Gerhard Pratt and MH Worthington. Inverse theory applied to multi-source cross-hole tomography. part 1: acoustic wave-equation method. *Geophysical prospecting*, 38(3):287–310, 1990.
- [56] R Gerhard Pratt. Seismic waveform inversion in the frequency domain, part 1: Theory and verification in a physical scale model. *Geophysics*, 64(3):888–901, 1999.
- [57] Laurent Sirgue and R Gerhard Pratt. Efficient waveform inversion and imaging: A strategy for selecting temporal frequencies. *Geophysics*, 69(1):231–248, 2004.
- [58] Zhong-Min Song, Paul R Williamson, and R Gerhard Pratt. Frequency-domain acoustic-wave modeling and inversion of crosshole data: Part ii-inversion method, synthetic experiments and real-data results. *Geophysics*, 60(3):796–809, 1995.
- [59] R Gerhard Pratt and Richard M Shipp. Seismic waveform inversion in the frequency domain, part 2: Fault delineation in sediments using crosshole data. *Geophysics*, 64(3):902–914, 1999.
- [60] J-X Dessa and G Pascal. Combined travelttime and frequency-domain seismic waveform

- inversion: a case study on multi-offset ultrasonic data. *Geophysical Journal International*, 154(1):117–133, 2003.
- [61] Yanghua Wang and Ying Rao. Crosshole seismic waveform tomography–i. strategy for real data application. *Geophysical Journal International*, 166(3):1224–1236, 2006.
- [62] AJ Breeders and RG Pratt. Efficient waveform tomography for lithospheric imaging: implications for realistic, two-dimensional acquisition geometries and low-frequency data. *Geophysical Journal International*, 168(1):152–170, 2007.
- [63] Priyank Jaiswal, Colin A Zelt, Albert W Bally, and Rahul Dasgupta. 2-d travelttime and waveform inversion for improved seismic imaging: Naga thrust and fold belt, india. *Geophysical Journal International*, 173(2):642–658, 2008.
- [64] Frank Natterer. Acoustic mammography in the time domain. *University of Münster, Germany, Tech. Rep*, 2008.
- [65] Olivier Roy, I Jovanović, Ali Hormati, Reza Parhizkar, and Martin Vetterli. Sound speed estimation using wave-based ultrasound tomography: theory and gpu implementation. In *SPIE Medical Imaging*, pages 76290J–76290J. International Society for Optics and Photonics, 2010.
- [66] Lianjie Huang, Youzuo Lin, Zhigang Zhang, Yassin Labyed, Sirui Tan, Nghia Nguyen, Kenneth Hanson, Daniel Sandoval, and Michael Williamson. Breast ultrasound waveform tomography: using both transmission and reflection data, and numerical virtual point sources. In *SPIE Medical Imaging*, pages 90400T–90400T. International Society for Optics and Photonics, 2014.
- [67] Cuiping Li, Gursharan S Sandhu, Olivier Roy, Neb Duric, Veerendra Allada, and Steven Schmidt. Toward a practical ultrasound waveform tomography algorithm for improving breast imaging. In *SPIE Medical Imaging*, pages 90401P–90401P. International Society for Optics and Photonics, 2014.
- [68] J Wiskin, DT Borup, SA Johnson, M Berggren, T Abbott, and R Hanover. Full-wave, non-linear, inverse scattering. In *Acoustical Imaging*, pages 183–193. Springer, 2007.
- [69] R Gerhard Pratt, Lianjie Huang, Neb Duric, and Peter Littrup. Sound-speed and

- attenuation imaging of breast tissue using waveform tomography of transmission ultrasound data. In *Medical Imaging*, pages 65104S–65104S. International Society for Optics and Photonics, 2007.
- [70] Keiiti Aki and Paul G Richards. *Quantitative seismology*, volume 1. 2002.
- [71] Philip McCord Morse. *Theoretical acoustics*. Princeton university press, 1968.
- [72] LD Landau and EM Lifshitz. Fluid mechanics, vol. 6. *Course of Theoretical Physics*, pages 227–229, 1987.
- [73] Bruce Roy Munson, Donald F Young, and Theodore Hisao Okiishi. *Fundamentals of fluid mechanics*. New York, 1990.
- [74] Sjoerd W Rienstra and Avraham Hirschberg. An introduction to acoustics. *Eindhoven University of Technology*, 18:19, 2003.
- [75] Tsutomu Kambe. *Elementary fluid mechanics*, volume 258. World Scientific, 2007.
- [76] Richard P Feynman, Robert B Leighton, and Matthew Sands. *The Feynman Lectures on Physics, Desktop Edition Volume I*, volume 1. Basic Books, 2013.
- [77] Geoffrey J Pert. *Introductory fluid mechanics for physicists and mathematicians*. John Wiley & Sons, 2013.
- [78] Paul M Chaikin and Tom C Lubensky. *Principles of condensed matter physics*, volume 1. Cambridge Univ Press, 2000.
- [79] Steven H Schot. Eighty years of sommerfeld’s radiation condition. *Historia Mathematica*, 19(4):385–401, 1992.
- [80] Philip McCord Morse and Hermann Feshbach. *Methods of theoretical physics*. 1953.
- [81] Alex H. Barnett. *Greens functions for the wave equation*, 2006.
- [82] George B Arfken. *Mathematical methods for physicists*. Academic press, 2013.
- [83] Olof Runborg. Lecture notes 5: Helmholtz equation and high frequency approximations, 2012.
- [84] John David Jackson and John D Jackson. *Classical electrodynamics*, volume 3. Wiley New York etc., 1962.
- [85] Pascal Podvin and Isabelle Lecomte. Finite difference computation of traveltimes in

- very contrasted velocity models: a massively parallel approach and its associated tools. *Geophysical Journal International*, 105(1):271–284, 1991.
- [86] Churl-Hyun Jo, Changsoo Shin, and Jung Hee Suh. An optimal 9-point, finite-difference, frequency-space, 2-d scalar wave extrapolator. *Geophysics*, 61(2):529–537, 1996.
- [87] Björn Engquist and Andrew Majda. Absorbing boundary conditions for numerical simulation of waves. *Proceedings of the National Academy of Sciences*, 74(5):1765–1766, 1977.
- [88] Bjorn Engquist and Andrew Majda. Radiation boundary conditions for acoustic and elastic wave calculations. *Communications on pure and applied mathematics*, 32(3):313–357, 1979.
- [89] Alain Bamberger, Patrick Joly, and Jean E Roberts. Second-order absorbing boundary conditions for the wave equation: a solution for the corner problem. *SIAM journal on numerical analysis*, 27(2):323–352, 1990.
- [90] Kurt J Marfurt. Accuracy of finite-difference and finite-element modeling of the scalar and elastic wave equations. *Geophysics*, 49(5):533–549, 1984.
- [91] Xiaoye S. Li. An overview of SuperLU: Algorithms, implementation, and user interface. *ACM Transactions on Mathematical Software*, 31(3):302–325, September 2005.
- [92] Milton Abramowitz and Irene A Stegun. *Handbook of mathematical functions: with formulas, graphs, and mathematical tables*. Number 55. Courier Corporation, 1964.
- [93] John A Scales and Martin L Smith. *Introductory geophysical inverse theory*. 1994.
- [94] Albert Tarantola. *Inverse problem theory and methods for model parameter estimation*. siam, 2005.
- [95] Gene H Golub, Per Christian Hansen, and Dianne P O’Leary. Tikhonov regularization and total least squares. *SIAM Journal on Matrix Analysis and Applications*, 21(1):185–194, 1999.
- [96] Jorge Nocedal and Stephen J Wright. *Numerical optimization*. *Springerverlang, USA*, 1999.

- [97] Jonathan Richard Shewchuk. An introduction to the conjugate gradient method without the agonizing pain, 1994.
- [98] R Brossier, Jean Virieux, and Stéphane Operto. Parsimonious finite-volume frequency-domain method for 2-dp-sv-wave modelling. *Geophysical Journal International*, 175(2):541–559, 2008.
- [99] Haijiang Zhang, Clifford Thurber, and Charlotte Rowe. Automatic p-wave arrival detection and picking with multiscale wavelet analysis for single-component recordings. *Bulletin of the Seismological Society of America*, 93(5):1904–1912, 2003.
- [100] Cuiping Li, Lianjie Huang, Nebojsa Duric, Haijiang Zhang, and Charlotte Rowe. An improved automatic time-of-flight picker for medical ultrasound tomography. *Ultrasonics*, 49(1):61–72, 2009.
- [101] O. Roy, I. Jovanovic, N. Duric, L. Poulo, and M. Vetterli. Robust array calibration using time delays with application to ultrasound tomography. In *SPIE Medical Imaging*, volume 7968, March 2011.
- [102] Nicole V Ruiter, Georg Göbel, Lutz Berger, Michael Zapf, and Hartmut Gemmeke. Realization of an optimized 3D USCT. In *SPIE Medical Imaging*, pages 796805–796805. International Society for Optics and Photonics, 2011.
- [103] Jason Sanders and Edward Kandrot. *CUDA by example: an introduction to general-purpose GPU programming*. Addison-Wesley Professional, 2010.
- [104] Lawrence E Spence, Arnold J Insel, and Stephen H Friedberg. *Elementary linear algebra*. Pearson/Prentice Hall, 2008.
- [105] U.S. FDA. Saline-filled breast implants, 2014. [Online; accessed 26-March-2015].
- [106] Wayne D Wilson. Equation for the speed of sound in sea water. *The Journal of the Acoustical Society of America*, 32(10):1357–1357, 1960.
- [107] National Cancer Institute. Body planes, 2007.
- [108] Blausen.com staff. Directional references, 2014.
- [109] Kuerer HM. Breast radial anti-radial.

ABSTRACT**FREQUENCY DOMAIN ULTRASOUND WAVEFORM TOMOGRAPHY
BREAST IMAGING**

by

GURSHARAN YASH SINGH SANDHU**August 2015****Advisor:** Dr. Zhi-Feng Huang**Co-Advisor:** Dr. Neb Duric**Major:** Physics**Degree:** Doctor of Philosophy

Ultrasound tomography is an emerging modality for imaging breast tissue for the detection of disease. Using the principles of full waveform inversion, high-resolution quantitative sound speed and attenuation maps of the breast can be created. In this thesis, we introduce some basic principles of imaging breast disease and the formalism of sound wave propagation. We present numerical methods to model acoustic wave propagation and methods to solve the corresponding inverse problem. Numerical simulations of sound speed reconstructions are used to assess the efficacy of the algorithm. A careful review of the preprocessing techniques needed for the successful inversion of acoustic data is presented. *Ex vivo* and *in vivo* sound speed reconstructions highlight the significant improvements that are made upon commonly used travel time sound speed reconstruction methods. The higher resolution and contrast of our waveform method will allow radiologists to make a more informed diagnosis of breast disease. A comparison of full waveform sound speed imaging to MRI shows a great deal of concordant findings. Lastly, we give examples of the use of full waveform inversion sound speed imaging in a clinical setting.

AUTOBIOGRAPHICAL STATEMENT

Name: Gursharan Yash Singh Sandhu

Education:

B.S. Physics, University of Michigan, Ann Arbor, MI 2010

B.S. Mathematics, University of Michigan, Ann Arbor, MI 2010

Professional experience:

Graduate Teaching Assistant, Wayne State University, Detroit, MI: 2010–2012

Graduate Research Assistant, Wayne State University, Detroit, MI: 2012–2014

Imaging Scientist, Delphinus Medical Technologies, Inc., Plymouth, MI, 2014–present

Publication:

1. Li, C., Sandhu, G. S., Roy, O., Duric, N., Allada, V., & Schmidt, S. (2014, March). Toward a practical ultrasound waveform tomography algorithm for improving breast imaging. In SPIE Medical Imaging (pp. 90401P-90401P). International Society for Optics and Photonics.
2. Sandhu, G. Y., Li, C., Roy, O., Schmidt, S., & Duric, N. (2015, March). High-resolution quantitative whole-breast ultrasound: in vivo application using frequency-domain waveform tomography. In SPIE Medical Imaging (pp. 94190D-94190D). International Society for Optics and Photonics.
3. Sandhu, G. Y., Li, C., Roy, O., Schmidt, S., & Duric, N. (2015). Frequency Domain Ultrasound Waveform Tomography: Breast Imaging Using a Ring Transducer. *Physics in Medicine and Biology* (Draft awaiting acceptance after revision from reviewer's suggestions).
4. Sandhu, G. Y., Li, C., Roy, O., Littrup, P., & Duric, N. (2015). Clinical Applications of Frequency Domain Ultrasound Waveform Tomography: a Preliminary Study. *Medical Physics* (First draft submitted).